ON THE UNDERLYING OPTICAL MECHANISMS OF THE ELECTRONIC SPECKLE PATTERN INTERFEROMETER (ESPI)

by

FERNANDO MENDOZA SANTOYO

A Doctoral Thesis
submitted in partial fulfilment of
the requirements for the award of
Doctor of Philosophy
of the
Loughborough University of Technology

February 1988

Supervisor: B D Bergquist
Department of Mechanical Engineering

To Ana Gema and Fernando

To my parents, brother and sisters

To my grandparents

CONTENTS

PAGE No.

PAGE No.

ABSTRACT

The underlying optical mechanism of the Electronic Speckle Pattern Interferometer (ESPI) was studied. It was theoretically found that the previous design concept of conjugacy was not needed, and that an alternative design gives better quality results. This was shown experimentally using different geometries and point of origin for the reference beam. The intrinsic problem of aliasing in the electronic apparatus of ESPI was investigated with the aid of an interferometric technique. Relevant parameters to the system were brought together to study a simplified model for the distribution of spatial frequencies at the plane of the object image. Experimentation on photographic speckle pattern interferometry revealed the need for the introduction of a variable spatial filter into the ESPI electronic system that will give way to fringes of holographic quality. Implications for future designs of ESPI are discussed.

INTRODUCTION

The optical design of the Electronic Speckle Pattern Interferometer (ESPI) has seen little change since first developed by Butters and Leendertz [1]. The main reason being the unsuccessful attempts by researchers to study its true working mechanism.

The objective of this Thesis is to investigate the underlying optical mechanism of ESPI, and thus achieve an optimal design for it.

Description of the Thesis.

The Thesis is divided into eight chapters and six appendices, as follows:

Chapter I starts describing ESPI, with a particular emphasis in the work done on the design of the optical head of the interferometer, which forms the basis of this Thesis. A literature survey of the relevant and related papers to the work to be carried out here is presented. Since literature reviews of ESPI are out of the scope of this Thesis they can be found in, for instance [2,3].

Chapter II deals with a theoretical model describing the interference between the scattering waves coming from a rough surface (object) and the scattered (from a ground glass) or smooth (from a microscope/spatial filter combination) waves acting as the reference beam in ESPI. It is found that different reference beam geometries are feasible, thus predicting the possibility of using the beam splitter (or beam combiner) in between the object and imaging lens, a new design for ESPI. The role of conjugacy as proposed in [4] and indeed in recent ESPI designs is consequently eradicated. A computer algorithm of the proposed model gives as a result well defined interference fringes.

Chapter III is the experimental version to the previous chapter. Here four different reference beam geometries are used, namely: divergent, convergent, parallel and speckled. The beams are interfered with the object waves in two ways: using the beam splitter a) in between the TV camera and the imaging lens (normal ESPI configuration), and b) in between the object and imaging lens. The results obtained for the latter case show considerable advantages over those in the former case.

Chapter IV examines the response of the electronic apparatus in ESPI to an incoming straight line fringe pattern whose spatial frequency can be varied, making possible an analogy with the more complicated and random case of speckles. The aliasing phenomena, independent of ESPI, appears as a result of the high and random spatial frequency detected by the TV-electronic system.

Chapter V studies the resolution problem of the imaging and electronic system (treated as a self contained entity). A simple model of interference between object and reference waves is presented that facilitates the understanding of the resolving capabilities of the electronics in ESPI.

Chapter VI exhibits the photographic analog to ESPI. A double-exposure photograph of the disturbed object directly shows on the film the same correlation (addition) fringe pattern as obtained in ESPI (on subtraction). (To the author's knowledge the double-exposure photographic speckle pattern interferometry presented here has for the first time been successfully used with non holographic film). An optical Fourier spatial filtering system is employed to filter out the optical noise in the image, finally obtaining a holographic quality fringe image. A non rigorous theoretical approach is given to describe this process. The results suggest the introduction of a variable filter in the electronic device of ESPI.

Chapter VII recommends improvements for future designs of ESPI based on the material of this Thesis.

Chapter VIII is a summary of the closure sections to be found at the end of each chapter.

Appendix A describes the theoretical formulation for the scattered field appearing in Chapter II.

Appendix B explains some of the results found in Chapter V.

Appendix C contains a list of symbols appearing in Chapters II and VI.

Appendix D is a list of tables in the thesis.

Appendix E is a list of figures in the thesis.

Appendix F contains a list of the author publications done during his work at Loughborough.

CHAPTER I
ELECTRONIC SPECKLE PATTERN INTERFEROMETRY (ESPI).

1.1 Description of ESPI.

Since the invention of ESPI by Butters and Leendertz [1], the research and development performed on this system has been directed towards the achievement of holographic quality fringe displays, since ESPI intrinsically gives noisy fringe patterns. This together with the fact that the system is difficult to set up and maintain, represent the only real drawback restricting commercial use.

The ESPI system has two main components: a) Optical components, and b) Electronic related components. Figure 1.1 schematically shows them.

Light from a cw laser is divided in two beams: one illuminating the object, and the other being spatially filtered and diverged to serve as the reference beam. This reference beam has to appear to come from about the pole of the viewing system, i.e. the conjugacy requirement.

The laser illuminated object is imaged on the TV camera plate. Its speckled appearance is due to the self interference of scattered light rays from the object's rough surface. The size of the speckles at the image plane of the viewing lens is determined by the aperture size in this imaging system. The beam splitter behind the imaging lens directs the reference beam towards the TV camera plate, thus combining it with the object rays at this plane. The path length difference (between object and reference paths) has to be equal to an even multiple of the laser resonator cavity length to achieve good coherence for the two beams.

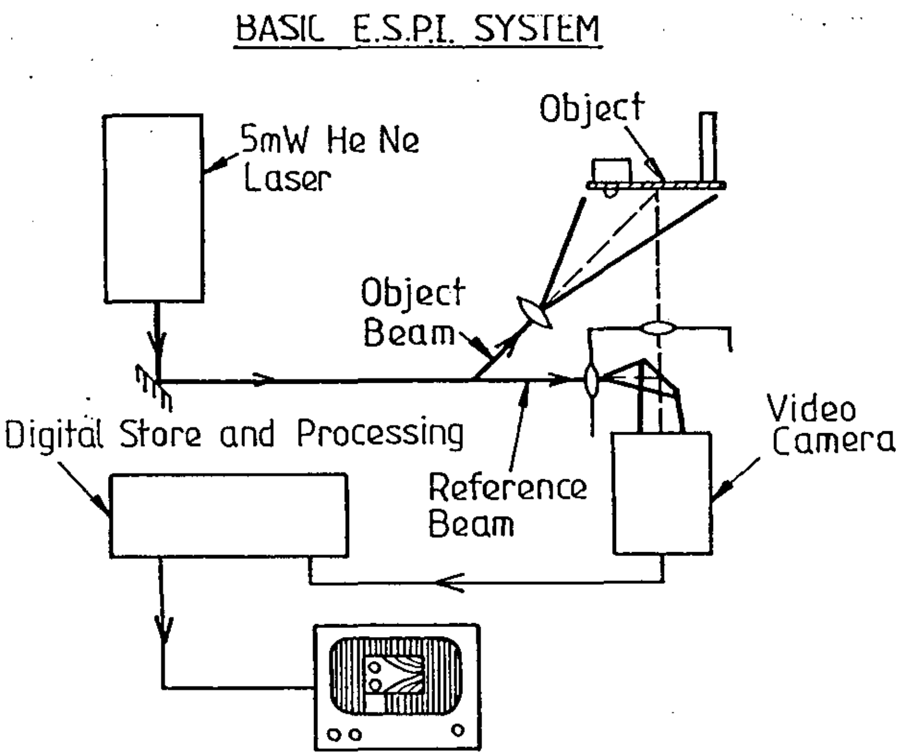

Figure 1.1
A conventional ESPI set-up.

The picture of the stationary object is stored in the system digital memory, and later subtracted from the instantaneous image of the disturbed object. The digital store pixel size is determined by the size of array the store can accommodate, which is larger (horizontally) than the limits set by the TV camera.

The result of this digital subtraction gives way to correlation fringe patterns displayed on the system monitor. This fringe pattern carries the information on the object deformation, hence the importance of getting a noise free image.

The noise in ESPI has two roots: optical and electronic. The optical noise comes from, mainly, the speckled appearance of the object and the optical components within the interferometer (such as dust in mirrors, etc.). The electronic noise is inherent to the TV camera plate and digital store.

During the years of the ESPI existence, several research workers have tackled these problems in different ways with an emphasis on the electronic signal processing (see for instance Slettemoen [5,6]) and on the speckle decorrelation properties of the system (Wykes [7]). Some successful techniques have been applied in the time average mode of ESPI that give holographic quality fringe displays (Montgomery [2]). More recently, techniques on computer fringe processing have relatively cleared the images from their speckled aspect [8].

All the research done so far on the noise subject, has been based on the early design of ESPI [1], as in fig. 1.1, and more importantly on the exact conjugacy of the diverging reference beam.

Pedersen et al. [9] highlights the importance of the reference wave to be precisely diverging from a virtual point inside the imaging lens aperture. Slettemoen [5,6] also relies on the reference beam conjugacy for his optimal ESPI design.

Some time later, Slettemoen published a paper [10] where he used a speckled reference beam made up from an object located at the plane of the object under investigation. His results include systems using f/# of f/1-f/2 as compared to those obtained in [6] of f/70. He does not make further comments about the possibility of extending this result to the use of different reference beam geometries coming from the object space.

Based on the concept of conjugacy Jones and Wykes [4] proposed a straightforward method leading to the optimization in the design of ESPI. In their paper they assume, for mathematical simplicity, that the smooth reference wavefront diverges from the center of the lens-aperture viewing system. Their mathematical approach has some algebraic inaccuracies, which are later appropriately dealt with in their book [3]. However, the need for accurate conjugacy is still seen as a major concept for the design of ESPI.

A later paper by Creath and Slettemoen [11] proposing a new form of ESPI uses the concept of conjugacy for its design. Here, due to the possibility of the image field being undersampled by the digital memory in ESPI, the authors introduce a diode-array camera to avoid this undersampling. They called this system DSPI.

In her latest paper, Wykes [12] discusses a theoretical method for the optimization of ESPI with limited laser power. Here the study is supported on the conjugacy requirement. This paper suggests that the optimal setting for the interferometer (and thus the clarity of the fringe patterns) depends on the laser power available (among other features). It will be shown in this Thesis that this argument is wrong, since an ESPI system based on the beam splitter lying in between the object and imaging lens (i.e. disregarding the conjugacy requirement) uses a full aperture lens, corroborating the results for a speckled reference beam obtained in [10].

More recently, Stetson and Brohinsky [36] introduce random access memory units (RAM) to replace the customary memory used in ESPI. Their optical set-up relied on the conjugacy concept. The quality of the fringes obtained is very poor if compared to those achievable in an ordinary ESPI. This is mainly due to their inaccurate assumption on the speckle field statistics and the difficulties in measuring the beam ratio correctly.

It is the intention of this Thesis to investigate the underlying optical mechanisms of ESPI not being considered previously, in order to achieve the knowledge needed to improve the performance of the system.

Next a review of the papers and books used in the development of each chapter is given.

1.2 Literature Survey.

The results in **Chapter II** are based on the theory of scattering as proposed by Beckmann and Spizzichino [13]. The derivation of the scattering coefficient, eq. (7), can be found there. The Kirchhoff principle is thoroughly explained in Born and Wolf [14] and its further propagation from the object space down to the image space follows that of Goodman [15]. The more complicated integrals (e.g. those containing Bessel functions) were solved using the tables of integrals by Gradshteyn [16].

Chapter III displays the experimental results for Chapter II. It shows figures obtained in an earlier paper by Bergquist and Mendoza Santoyo [17]. Their results are further confirmed by section 3.4 of this chapter and results by Montgomery ([2], pp. 187). It should be pointed out here the similarity between section 3.4 of this chapter and a paper published by Stetson [18] and that of Slettemoen [10].

At first glance it would appear that the set up proposed by Stetson has a similar lay out to that using the beam splitter in between the object and imaging lens using a divergent reference beam employed in this Thesis, but a closer inspection of his model reveals a different system, e.g. uses an eyepiece to image the beam splitter onto the retina of the eye (this beam splitter lies in between the lens imaging the object and the eyepiece).

The Slettemoen model uses a stationary object at the plane of the object under inspection to create the speckled reference beam. This might bring up the question as to which object is being under inspection. With the speckled beam of section 3.4 this ambiguity is solved by placing the speckled reference source on a different plane, thus imaging only the object under study.

The image processing routine used in this chapter is in agreement with a previous study done by Tanner [19] on the fringe clarity of laser produced fringes. Tanner stresses the need for, in the presence of speckle, an integration over a distance much larger than the speckle size must be carried out to find the fringe visibility of a pattern.

Chapter IV looks for the characterization of the ESPI response to a spatial frequency variable fringe pattern produced with a Mach-Zehnder type of interferometer (this apparatus is primarly used to measure refractive index variations [14], but due to its versatility it can be used to produce a pattern of frequency variable straight line fringes). The results presented here are the first of their kind in ESPI: a paper is being currently prepared on this subject [20].

The ray-tracing technique used in **Chapter V** can be found in Jenkins and White [21]. The model proposed in this chapter finds that the use of slit like apertures (to go in front of the imaging lens) might be an advantage towards the need (if any) to resolve the interference between the object and reference beams. Slettemoen [10,22] uses a multislit aperture for his speckled reference beam model with the aim of separating the cross-interference terms from the self-interference terms of object and reference beams.

The use of photographic speckle techniques to measure in-plane and out-of-plane displacements has been widely investigated by several authors [23-30]. In **Chapter VI** a photographic technique for double-exposure speckle interferograms is reported that obtains out-of-plane fringe patterns on a single piece of non-holographic film. The fringes are clearly visible on the film and Fourier plane spatial filtering was used to remove the optical noise surrounding the fringe patterns.

Burch and Tokarski proposed [23] that by recording m speckle patterns with m-1 in-plane displacements on a single photographic plate and then using a Fourier filtration system to transform this multiple exposed plate, the fringes observed in the Fourier plane represented the object in-plane movement.

Leendertz [24] used two speckled patterns photographed on different plates that, after being superimposed and Fourier filtered, give fringe patterns corresponding to the object deformation; the use of a reference beam combined with the object waves to obtain phase information from object points is suggested (the idea was later used in the realization of the ESPI by Butters and Leendertz [1]).

Archbold et al. [25] found fringe patterns on double-exposed photographs of speckle patterns due to in-plane displacements. The object's surface was illuminated by two oblique beams to measure small surface strain, or with a single beam for in-plane displacements. To observe the fringes thus formed Fourier plane filtering was used (an unexpanded laser beam used to create Young's fringes has roughly a similar effect).

Tiziani applied speckle photography to in-plane vibration analysis, and measurement of tilts [26,27].

Stetson [28] gave a theoretical account of speckle techniques to include measurements of strains in the absence of large displacements, and measurements of large displacements alone.

Verhoeven and Farrell [29] used speckle interferometry with a collimated reference beam to obtain measurements of density variation for a cylindrical flame. They used spatial filtering to recover fringe patterns.

The theoretical description given in Chapter VI follows that of Klimenco et al [30]. They work on the in-plane and rotation interferometric case using holographic plates to record the events.

1.3 Closure.

The research done so far on ESPI images has been concentrated on the study of the statistical propeties of the speckle, on the electronic signal processing of the images, on different techniques of noise reduction and more recently, with the presence of more powerful computers, on the digital image processing of the fringes. Besides new systems have been introduced with the use of diode-array TV cameras that display nearly noise free pictures.

The different techniques on photographic speckle interferometry fail to give any useful information to be applied in ESPI.

Despite the thorough studies on these subjects the ESPI system has never been successfully studied on its basic working principles. It is the belief of the author that the work presented in this Thesis gives a final new design concept of ESPI based on its underlying optical mechanisms.

CHAPTER II
THEORY FOR THE INTERFERENCE EQUATION ON THE IMAGE PLANE

2.1 Introduction.

The subject to be treated in this chapter is that of the interference pattern created when scattered object wavefronts overlap smooth reference beams of different geometries at the plane of the object image (the solution can be extended to that considering a speckled reference beam).

The most common and straightforward solution to this problem is when the complex amplitude distribution of the scattered light due to object surface profile variations , is described in terms of a real (and constant) amplitude times a random phase variation. The reference beam is represented by a (usually) unitary amplitude term times a constant phase. The result when these two complex amplitudes are added up and squared at the object's image plane is an intensity distribution along this plane, of the form:

$$I_{i,1} = I_o + I_r + 2\ (I_o I_r)^{1/2}\ \cos(\phi_o + \phi_r + \psi_o) \qquad (1)$$

where I_o and I_r are the intensities of the object and reference beams respectively and ϕ_o and ϕ_r the object and reference beam phases: ψ_o is a random phase related to the speckles. All these parameters are functions of the (X_v,Y_v) image plane coordinates.

Eq.(1) being modulated by a cosine function describes the intensity distribution on the image plane as an interference pattern whose spatial frequency distribution and form depend on ϕ_o and ϕ_r. This interference pattern is not resolved by the ESPI system electronics (Chapter V).

For ESPI a second interference pattern similar to that in eq.(1) is obtained by deforming the object in such a way that the phase value changes from ϕ_o to $\phi_o + \Delta\phi$. The intensity distribution on the image plane is now given by:

$$I_{1,2} = I_o + I_r + 2\ (I_oI_r)^{1/2}\ \cos(\phi_o + \psi_o + \Delta\phi + \phi_r) \qquad (2)$$

where I_o and I_r are assumed to remain unchanged. (This is true for the case of the reference beam if it stays unchanged during the deformation. For the object beam this approximation largely depends on the object's surface roughness, direction in which it is illuminated and viewed by the imaging-photosurface system).

After subtracting electronically (in this Thesis it is proved that the same fringe patterns can be reproduced on addition using photographic methods) eqs. (1) and (2), the intensity distribution appears now as a well defined fringe pattern modulated by a sine term of the form:

$$Mo = 2\ \sin(\phi_o + \psi_o + \phi_r + \Delta\phi/2)\ \sin(\Delta\phi/2) \qquad (3)$$

At this stage a more formal analytical model for the object random phase distribution is required to assess with more certainty the exact surface deformation suffered by the object when it was disturbed. Although it is well known that the exact form of the phase distribution on or near the image plane is extremely complicated ([14], pp. 447), and is indeed an active research area (see for instance [31]), in this chapter a more realistic model for the phase will be found that, to a good extent, theoretically reproduces the ESPI system.

The work is presented in sections as follows:

Section 2.2 starts with the form of the field scattered by an arbitrary object surface. By applying the Kirchhoff diffraction formula ([15], pp. 60) to the field next to the object, the object field before the lens surface is obtained.

Section 2.3 applies the lens transformation (e.g. [15], Chapter 5) to the field before the lens to obtain the field distribution immediately after it. Then propagation of this field to the image plane is carried out in the usual way.

Section 2.4 works out the reference beam propagation using the same methodology of the previous sections. Here two cases are distinguished:

a) when the reference beam comes from a point in between the object and the imaging lens, i.e. the beam splitter is located between the object and the imaging lens, and

b) when the reference beam comes from a point in between the imaging lens and the image plane (photosurface), i.e. normal ESPI configuration.

Three reference beam geometries (together with the speckled case) are considered, i.e. parallel, convergent and divergent beams.

Section 2.5 treats the interference between the object and reference field distributions obtained in the sections above.

In section 2.6 the final interference equation is used to create a computer program that simulates the ESPI system for the particular case of object rotations.

2.2 Object Field Distribution in The Object Space.

2.2.1 Object Scattered Field.

Let an approximately plane object (assumed to be rough in two-dimensions) with amplitude reflectivity $r_{ao}(x',y')$ be placed at a distance u in front of a converging lens system of focal length f. The object is being illuminated by a diverging monochromatic wave, having a useful parabolic approximation to the spherical wave, of amplitude,

$$U_{in}(r') = (1/i\lambda r_i)\ \exp(ikr_i)\ \exp(ik|r'|^2/(2r_i)) \qquad (4)$$

where: $k = 2\pi n/\lambda$, λ being the wavelength of the illuminating light and n the index of refraction of air (usually taken as 1); r_i is the distance from the point where the illuminating beam originates and the object surface; and r' is a position vector defined with respect to the x',y' axes defined on the object surface (see fig. 2.1).

If $r_i \gg 1$ eq.(4) represents a nearly parallel illuminating wave. In most of the practical arrangements this condition applies, and therefore it can be assumed that the object is being illuminated uniformly.

The Object surface roughness will be represented by the function:

$$\xi = \xi(x',y') \qquad (5)$$

whose mean is represented by the local tangential plane (it is being considered a single resolution cell on the object):

$$z = 0 \qquad (6)$$

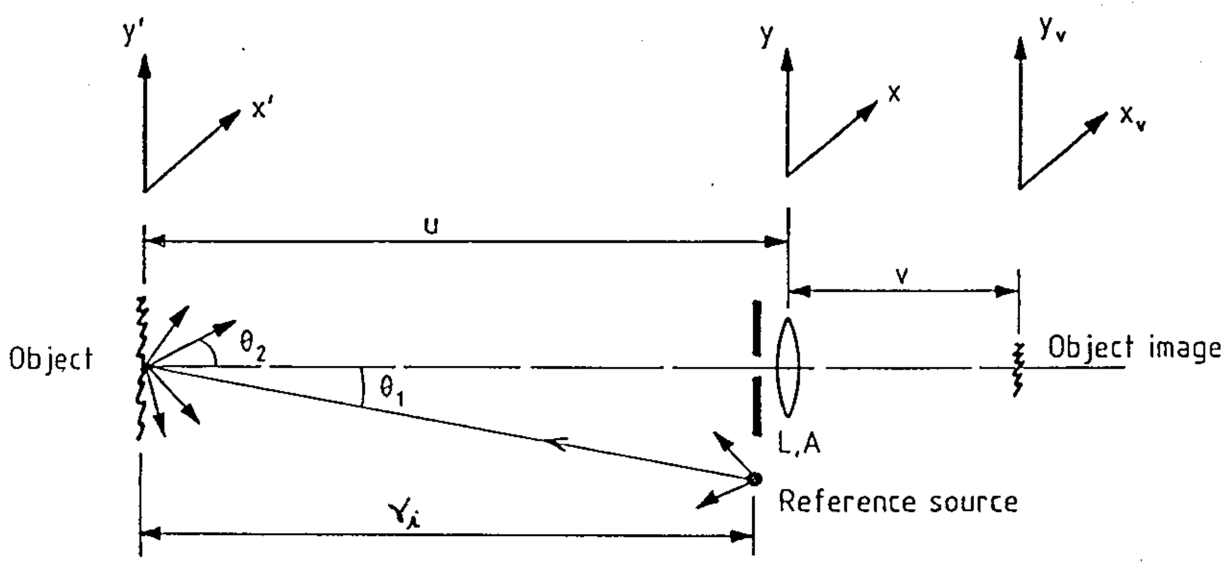

Figure 2.1
Geometrical array showing illuminating beam incident at an angle θ_1 to the z optical axis.

The scattered field from the object is represented by a scattering normalized coefficient equal to (e.g. [13], pp.22):

$$\rho = E_2/E_{2o} \tag{7}$$

where E_2 is the actual scattered field and E_{2o} is the object field for the direction of specular reflection ($\theta_1 = \theta_2$) by a smooth (ξ = 0) , perfectly conducting plane for the same object dimensions. Then,

$$E_{2o} = i\ k\ S\ \cos\theta_1\ \exp(i\ k\ r_o)/(\pi\ r_o) \tag{8}$$

Here r_0 is the distance, measured from the object surface, where the field is being observed; $S = 4xy$ is the area of the object on the X'Y' plane; θ_1 is the angle of incidence of the illuminating beam included between the direction of propagation and the z axis.

Before displaying the exact analytical form of ρ in eq.(7) the following features are assumed:

a) A perfectly conducting surface, i.e. when the local reflection coefficient of the surface is independent of the local angle of incidence, $r_{eo}(x',y') = 1$.

b) No polarization effects will be included.

c) $S \gg \lambda^2$ (9)

d) Mutual interaction of surface irregularities such as shadowing and multiple scattering are neglected.

e) The incident wave is plane and linearly polarized.

f) The point of observation is far from the surface in such a way as to consider the scattered waves as plane.

All these assumptions will not weaken the validity for the ρ equation, as long as the surfaces under study are composed of irregularities with small curvatures, i.e. the radius of curvature of the irregularities $\gg \lambda$. Therefore the relation for ρ (eq.(10)) holds when the surface does not contain sharp edges, sharp points or other irregularities with small radii of curvature.

Hence ρ in eq.(7) is given by ([13], pp. 27):

$$\rho(\theta_1;\theta_2,\theta_3) = F_3/S \iint \exp(i\ \mathbf{v}.\mathbf{r})\ dx'dy' \tag{10}$$

where:

a) The integral is taken over the object area,

b) $F_3 = (1+\cos\theta_1\cos\theta_2-\sin\theta_1\sin\theta_2\cos\theta_3)/(\cos\theta_1(\cos\theta_1+\cos\theta_2))$, (11)

c) $\mathbf{v}.\mathbf{r} = k\ ((\sin\theta_1-\sin\theta_2\cos\theta_3)x-\sin\theta_2\sin\theta_3 y-(\cos\theta_1+\cos\theta_2)\xi)$, (12) .
where $\mathbf{r}' = x'\mathbf{i} + y'\mathbf{j} + \xi\mathbf{k}$, is a position vector in the object plane.

d) θ_2 is the angle of scattering included between the z axis and the direction of scattering, both measured with respect to the positive z axis (θ_2 measured in opposite sense as θ_1); θ_3 is an angle for lateral scattering out of the plane of incidence given by θ_1.

2.2.2 Propagation of the Scattered Field.

On applying the Kirchhoff formulation to eq.(10) the following condition is assumed:

$$\lambda \ll (x'^2 + y'^2)^{1/2} \ll z \qquad (13)$$

The left hand side of this inequality is already implied for eq.(10), and the remaining part of the inequality holds for most of the practical cases where the square root of the object surface area under study is much smaller than the distance from the (x',y') coordinates to the point of observation.

In the plane (z = u) of the lens eq.(7) for E_2 then takes the form:

$$U(x,y,z=u) = \exp(iku)/(i\lambda u)\iint_{-\infty}^{+\infty} E_{2o}\ \rho(x',y')$$
$$\exp(ik[(x-x')^2 + (y-y')^2]/2u)\ dx'\ dy' \qquad (14)$$

Eq.(14) gives the object field incident on the lens at coordinates (x,y). The finite extent of the lens aperture can be described by a pupil function P(x,y) defined by:

$$P(x,y) = \begin{cases} 1 & \text{for } (x,y) \text{ points inside the lens aperture,} \\ 0 & \text{otherwise.} \end{cases} \tag{15}$$

If an aperture is used in front of the lens, then this acts as the real lens aperture being employed, but if this aperture is located behind the lens (in between the lens and the photosurface), then the rim of the lens acts as the limiting aperture.

2.3 Object Field Distribution in the Image Space.

2.3.1 The Lens Transformation.

The amplitude distribution immediately after the lens is ([15], Chapter 5):

$$U'(x,y) = U(x,y,u)\ P(x,y)\ \exp(ikn'\Delta_o)\ \exp(-ik|r^2|/2f) \tag{16}$$

where U(x,y,u) and P(x,y) are given by eqs.(14) and (15) respectively; r is the magnitude of the position vector (**r**) to the point (x,y) as measured from the coordinates origin in the lens XY plane; n' is the index of refraction of the lens material and Δ_o is the lens central thickness.

The term $\exp(ikn\Delta_o)$ is a constant phase delay that will be omitted in the calculations hereafter.

2.3.2 Field Distribution at the Image plane.

To find the field distribution $U_v(x_v,y_v)$ across the image plane, eq.(16) is propagated to the plane z = v (the lens to image plane distance) as follows:

$$U_v(x_v,y_v,v) = (1/i\lambda v)\ \exp\{ikv\} \iint_{-\infty}^{+\infty} dx\ dy\ U'(x,y)$$
$$\exp\{(ik/2v)[(x - x_v)^2 + (y - y_v)^2]\} \qquad (17)$$

Substituting eq.(16) into eq.(17) and expanding the quadratic factors gives:

$$U_v(x_v,y_v,v) = (1/i\lambda v)\ \exp\{ikv\} \iint_{-\infty}^{+\infty} dx\ dy\ U(x,y,u)\ P(x,y)$$
$$\exp\{-ik|r|^2/2(1/f - 1/v)\}\exp\{ik/2v(x_v^2 + y_v^2)\}\exp\{-ik/v(x_v x + y_v y)\} \qquad (18)$$

If the finite extent of the lens aperture is neglected, i.e. P = 1, and the lens formula

$$1/u + 1/v = 1/f \qquad (19)$$

is used ($\lambda \ll 1$, geometrical optics case), eq.(18) takes the form (substitution of eq.(14) is done too):

$$U_v(x_v,y_v) = -\exp\{ik(v + u)\}/(vu\lambda^2)\quad \exp\{ik(x_v^2 + y_v^2)/2v\}$$
$$\iint_{-\infty}^{+\infty} (E_{2o}\ \rho(x',y')\ \exp\{ik(x'^2 + y'^2)/2u\}$$
$$\iint_{-\infty}^{+\infty} \exp\{-ik[(x_v + Mx')x + (y_v + My')y]/v\}\ dx\ dy)\ dx'dy' \qquad (20)$$

where M (= v/u) is the lens system magnification.

Making the change in variables:

$$x \to x/\lambda v \qquad \text{and} \qquad y \to y/\lambda v \tag{21}$$

and integrating over dx dy, eq.(20) becomes:

$$U_v(x_v,y_v) = -\exp\{ik(v+u)\}\exp\{ik(x_v^2 + y_v^2)/2vf\}\, M \int\!\!\int_{-\infty}^{+\infty} E_{20}\,\rho(x',y')\,\delta(x_v + Mx', y_v + My')\,dx'\,dy' \tag{22}$$

where δ is the Dirac function.

Finally performing the last integration over dx' dy', it is obtained:

$$U_v(x_v,y_v) = -(1/M)\exp\{ik(v+u)\}\exp\{iku(x_v^2 + y_v^2)/(2vf)\}\, E_{20}\,\rho(-x_v/M, -y_v/M) \tag{23}$$

Eq.(23), besides the constant factor dropped in the last section, expresses the complex amplitude distribution of the object waves on the image plane of a lens of focal length f. It gives an analytical form for the phase terms (through $E_{20}\ \rho$) due to object surface profile.

Consider now the case when the pupil function is represented by a circular aperture of the form:

$$P(r) = \mathrm{circ}(r/\alpha) = \begin{cases} 1 & \text{for } r/\alpha \leqslant 1, \\ 0 & \text{otherwise.} \end{cases} \tag{24}$$

where α is the radius of the aperture and r is the magnitude of any position vector inside the aperture. After the change in variables:

$$\left.\begin{array}{lll} \bar{x} = x/(\lambda v) & \text{and} & \bar{y} = y/(\lambda v) \\ \bar{x}' = -Mx' & \text{and} & \bar{y}' = -My' \end{array}\right\} \qquad (25)$$

eq. (20) becomes:

$$U_v(x_v, y_v) = -(1/M)\exp\{ik(v+u)\}\exp\{ik(x_v^2 + y_v^2)/2v\}$$

$$\int\!\!\int_{-\infty}^{+\infty} d\bar{x}'d\bar{y}'\; E_{2o}\; \rho(-\bar{x}'/M, -\bar{y}'/M)\exp\{ik(\bar{x}'^2 + \bar{y}'^2)/(2vM)\}\; h(x_v-\bar{x}', y_v-\bar{y}') \qquad (26)$$

where

$$h(x_v-\bar{x}', y_v-\bar{y}') = \int\!\!\int_{-\infty}^{+\infty} P(\lambda v\bar{x}, \lambda v\bar{y})\exp\{-i2\pi[(x_v - \bar{x}')\bar{x} + (y_v - \bar{y}')\bar{y}]\}\; d\bar{x}\; d\bar{y} \qquad (27)$$

is the invariant impulse response function.

Eq. (26) is the convolution integral of the impulse function h with the geometrical image; it contains the geometrical optics amplitude distribution of the object, namely:

$$U_{go}(x_v, y_v) = -(1/M)\exp\{ik(v+u)\}\exp\{ik[(x_v^2+y_v^2)+(\bar{x}'^2+\bar{y}'^2)/M]/2v\}$$
$$E_{2o}\quad \rho(-\bar{x}'/M, -\bar{y}'/M) \qquad (28)$$

Therefore eq. (26) illustrates the effect of introducing a diffracting aperture into the problem. As a consequence of the non zero width of the impulse function h, the image is not a perfect replica of the object. Solving for the circular aperture (with $r_1 = r/\alpha$), eq. (27) takes the form:

$$h(x_v - x', y_v - y') = \int_0^{2\pi}\int_0^{\alpha} \exp\{-i(2\pi/\lambda v)[(x_v - x')r_1\cos\theta_1 + (y_v - y')r_1\sin\theta_1\} \, r_1 \, dr_1 \, d\theta_1 \qquad (29)$$

Performing the integration over θ_1 and subsequently that for r_1 it is obtained for the impulse response function:

$$h(x_v - x', y_v - y') = (\lambda v/\Omega\alpha) \, J_1(2\pi\Omega/\lambda v\alpha) \qquad (30)$$

where, $\Omega = ((x_v - x')^2 + (y_v - y')^2)^{1/2}$.

Finally substituting in eq.(26), the complex amplitude distribution at the image plane is obtained for a circular aperture of radius α:

$$U_v(x_v, y_v) = -(\lambda v/M\alpha) \exp\{ik(v + u)\} \exp\{(ik/2v)(x_v^2 + y_v^2)\}$$
$$\int\int_{-\infty}^{+\infty} dx'dy' \; E_{20} \, \rho(-x'/M, -y'/M) \exp\{(ik/2vM)(x'^2 + y'^2)\} \, [(1/\Omega)J_1(2\pi\Omega/\lambda v\alpha)] \qquad (31)$$

Eq.(31) gives the solution for the complex amplitude at the image plane of a lens of focal length f due to a uniformly illuminated object element whose surface scattering coefficient is ρ (given by eq.(7)). It shows the form of the contribution from different portions of the object surface to the image point in consideration, when diffraction effects due to the circular aperture are taken into account.

2.4 Reference Beam Propagation.

2.4.1 Beam Splitter Behind the Lens.

With regard to fig.2.2 the complex amplitude distribution on the image plane due to the disturbance $U(x_r, y_r)$ at the plane of the reference source is (after applying the Kirchhoff formulation, as in eq.(14)):

$$Ur_v(x_v, y_v, u_v) = (1/i\lambda u_v)\exp(iku_v) \iint_{-\infty}^{+\infty} dx_r\, dy_r\, U(x_r, y_r)\exp((ik/2u_v)[(x_v - x_r)^2 + (y_v - y_r)^2) \quad (32)$$

where it was assumed that the origin of the X_rY_r plane is colinear to the optical axis.

Consider four different cases of reference beams: i) Speckled, and smooth: ii) Divergent, iii) Convergent and iv) parallel.

i) Eq.(32) represents the scattered light propagated through a distance u_v, if $U(x_r, y_r)$ is replaced by the scattering coefficient $E_{2o}\ \rho$ given by eq.(7) and corresponding to the object producing the speckled reference beam.

ii) From eq.(32) and assuming $U(x_r, y_r)$ to be a point source colinear with the optical axis, it is obtained:

$$Ur_v(x_v, y_v) = (1/i\lambda u_v)\exp(iku_v)\exp((ik/2u_v)(x_v^2 + y_v^2)) \quad (33)$$

This equation represents a diverging spherical wavefront coming from a point $z = u_v$. The factor $\exp(-i\pi/2)$ (= $1/i$) gives way to waves oscillating a quarter of a period out of phase at (x_v, y_v).

iii) The solution for the convergent wavefront is analogous to that of eq. (33). The difference being that the solution for the convergent beam contains a negative sign in front of the exponentials, and u_v is now the point of convergence.

iv) From eq. (32) and a parallel beam of amplitude A acting as reference (assuming it is normally incident on the X_vY_v plane), then:

$$Ur_v(x_v, y_v) = A \exp\{iku_v\} \tag{34}$$

The relation above represents a parallel wavefront of amplitude A, and phase ku_v relative to the initial wavefront at the X_rY_r plane.

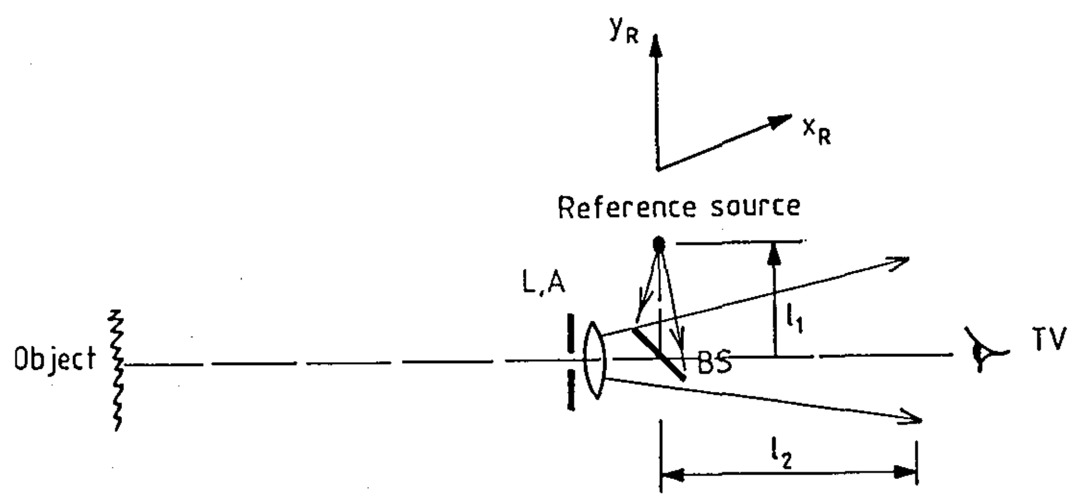

$$l_1 + l_2 = u_v$$

Figure 2.2
Layout shows beam splitter in between the lens and the image plane. The reference beam originates from an imaginary point on the optical axis.

2.4.2 Beam Splitter in Front of the Lens.

Suppose again that the reference source is coming from an imaginary set of axes perpendicular to the optical axis (see figure 2.3). Following the procedure in sections 2.2 and 2.3 for the propagation of waves from the object space to the image one, the reference field distribution on the image plane will be given by:

$$Ur_v(x_v,y_v) = -(1/\lambda^2 vu_r)\exp(ik(v+u_r))\exp((ik/2v)(x_v^2+y_v^2))$$
$$\int\int_{-\infty}^{+\infty} dx_r dy_r\, U(x_r,y_r)\exp((ik/2u_r)R_r^2)\int\int_{-\infty}^{+\infty} dx\, dy\, P(x,y)$$
$$\exp((ik/2)r^2(1/u_r+1/v-1/f))\exp\{-ik[(x_v/v+x_r/u_r)x+(y_v/v+y_r/u_r)y]\} \qquad (35)$$

where: $R_r^2 = x_r^2 + y_r^2$, (x_r,y_r) coordinates at the reference beam plane of origin; $r^2 = x^2 + y^2$, (x,y) coordinates at lens plane; $P(x,y)$ the aperture or pupil function, and u_r is the distance (in the object space) from the lens to the origin of the X_rY_r plane.

Again four different geometries for the reference beam can be distinguished.

1) For a speckled reference beam, substituting $E_{2o}\,\rho$, the scattering coefficient similar to that in eq.(7) (this time the object producing the speckled beam is a ground glass, so the factor $E_{2o}\,\rho$ differs from that of the object under study) for $U(x_r,y_r)$, eq.(35) gives the complex amplitude at the plane of the object image. Before writing down the resulting expression, it is noticed that eq.(35) includes the effect produced by the pupil function P(x.y). Two different forms of this function are considered next:

1) $P(x,y) = 1$, as in relation (15), i.e. $\lambda \ll 1$ or geometrical optics case. Substituting back in eq.(35):

$$U_{rv}(x_v, y_v) = (1/a\lambda^2 v u_r)\, \exp(-i\pi/2)\, \exp(ik(v+u_r))\, \exp((ik/2v)(x_v^2+y_v^2))$$

$$\int\int_{-\infty}^{+\infty} dx_r\, dy_r\, E_{2o}\, \rho(x_r, y_r)\, \exp((ik/2u_r)R_r^2)\, \exp(-(i/4a)(b^2 + b'^2)) \qquad (36)$$

where the parameters a, b and b' are given by:

$$\left.\begin{aligned} a &= (k/2)\ (1/u_r + 1/v - 1/f), \\ b &= k\ (x_v/v + x_r/u_r) \\ b' &= k\ (y_v/v + y_r/u_r). \end{aligned}\right\} \qquad (37)$$

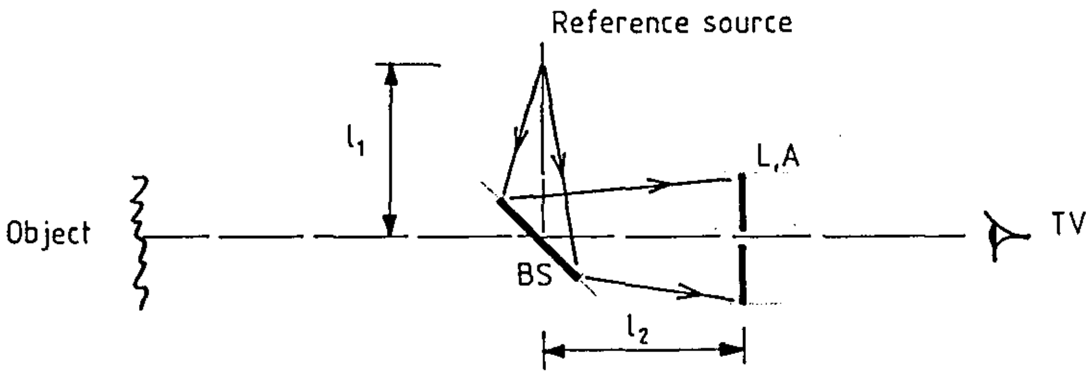

$$l_1 + l_2 = u_r$$

Figure 2.3
Set-up showing the reference beam coming from a point or plane in between the object and imaging lens.

2) P(r) is given by eq.(24) as representing a circular aperture. Substituting in eq.(35) gives:

$$Ur_v(x_v,y_v) = (\alpha^2/2a\lambda^2 vu_r)\exp\{-i\pi/2\}\exp\{(ik/2v)(x_v^2 + y_v^2)\}$$
$$\iint_{-\infty}^{+\infty} dx_r\, dy_r\, E_{20}\,\rho(x_r,y_r)\exp\{(ik/2u_r)R_r^2\}\exp\{-(ik^2/4a)r_{vr}^2\} \quad (38)$$

where: $r_{vr}^2 = (x_v/v + x_r/u_r)^2 + (y_v/v + y_r/u_r)^2$, and α is the radius of the aperture.

Eqs.(36) and (38) express the analytical form of the complex amplitude distribution for the speckled reference beam and for two different pupil functions.

ii) If the reference beam diverges from a point in the optical axis, i.e. $U(x_r,y_r) = \delta(0,0)$, eq.(35) (for the two pupil functions mentioned in the previous case) takes the form:

1) P(x,y) = 1,

$$Ur_v(x_v,y_v) = (\pi/a\lambda^2 vu_r)\exp\{-i\pi/2\}\exp\{ik(v + u_r)\}$$
$$\exp\{-(ik/2v)(x_v^2 + y_v^2)[(1/f - 1/u_r)/(1/u_r + 1/v - 1/f)]\} \quad (39)$$

2) P(r) = circ (r), as in eq.(24).

$$Ur_v(x_v,y_v) = (\alpha^2/2a\lambda^2 vu_r)\exp\{-i\pi/2\}\exp\{ik(v + u_r)\}$$
$$\exp\{-(ik/2v)(x_v^2 + y_v^2)[(1/f - 1/u_r)/(1/u_r + 1/v - 1/f)]\} \quad (40)$$

Eq.(40) is the representation of the complex amplitude distribution at the object image plane when diffraction effects are accounted for. The similarity between eqs.(39) and (40) is noted: they have the same phase but the amplitude is different (eq.(40) is equal to eq.(39) but for a factor $\alpha^2/2\pi$), i.e. the presence of the aperture affects the intensity of the field at the image plane and the size of the Airy diffraction ring (and thus the speckle size).

Both, eq.(39) and eq.(40) give converging spherical wavefronts at the image plane if and only if:

$$u_r > f \quad , \quad f > u_r v/(v + u_r) \quad , \text{ and } u_r < u \tag{41}$$

iii) If a converging beam is directed towards the imaging lens, to converge at a point in between the lens and this lens focal point, then the net effect is that the beam will now diverge from an imaginary point v_r given by eq.(19). Therefore, eqs.(39) and (40) give a divergent reference source if:

$$u_r < f \quad \text{and} \quad f > u_r v/(v + u_r) \tag{42}$$

Then, the quadratic exponentials become positive giving way to diverging reference waves appearing to come from a point v_r.

iv) Let the plane wave on the $X_r Y_r$ plane be of amplitude A.

1) Pupil = 1 and eq.(35),

$$Ur_v(x_v, y_v) = -(Au/v)\exp(ik(v + u_r)) \exp((ik/2(v - f))(x_v^2 + y_v^2)) \tag{43}$$

Eq.(43) is a diverging wave from the lens focal point.

2) Circular pupil and eq.(35),

$$Ur_v(x_v, y_v) = -(A\alpha^2 u/2\pi v)\exp(ik(v + u_r)) \exp((ik/2(v - f))(x_v^2 + y_v^2)) \tag{44}$$

The above equation represents a spherical wavefront diverging from the lens focal point. Comparing it with eq.(43), it is noticed that in eq.(44) the amplitude is now being multiplied by $\alpha^2/2\pi$, this is due to the effect of the diffracting aperture.

As a summary of this section, it must be pointed out that: a) eqs.(33), (39) and (40) (with the correct sign in the exponentials), (43) and (44) all describe diverging reference wavefronts at the object's image plane, and b) eqs.(33) (with the right change in sign), (39) and (40) describe converging reference wavefronts impinging the image plane of the object.

The theoretical characteristics described above, show that the actual reference beam can be originated from anywhere in the ESPI system and not necessarily from the so called conjugacy point. In fact it will be shown in the next section that a reference beam originating from a plane close to the object surface simplifies by much the calculations.

2.5 Object and Reference Waves Interference.

2.5.1 The Interference Equation: a Particular Case.

Since the wavelength of the light used throughout this Thesis is such that:

$$\lambda = 0.6328\ \mu m \ll 1, \tag{45}$$

the first approximation taken is to choose the Pupil function equal to 1, i.e. the geometrical optics approach will be used everywhere in this section. Then eq.(23) will be used to represent the object field at its image plane, viz:

$$U_v(x_v, y_v) = -(1/M)\exp(ik(v + u))\exp((iku/2vf)(x_v^2 + y_v^2))$$
$$E_{20}\ \rho(-x_v/M, -y_v/M) \tag{23}$$

As the complex amplitude distribution for the reference beam, eq.(43) for a parallel beam is chosen, namely:

$$Ur_v(x_v,y_v) = -(Au/v) \exp\{ik(v + u_r)\} \exp\{(ik/2(v - f))(x_v^2 + y_v^2)\} \tag{43}$$

Assuming that $u = u_r$, i.e. the reference beam originates from the object plane, the intensity of the interference pattern created between eqs. (23) and (43) is, to within a constant factor:

$$I= (U + Ur_v)(U^* + Ur_v^*) = UU^* + Ur_vUr_v^* + UUr_v^* + U^*Ur_v \tag{46}$$

where the dependence on the (x_v,y_v) coordinates has been dropped since all the variables involved depend on them.

Substituting from eqs. (23) and (43) into eq. (46), it is obtained:

$$I = (1/M^2)\ E_{2o}^2\ \rho\rho^* + (Au/v)^2 + (Au/Mv)\ E_{2o}\ \{\rho + \rho^*) \tag{47}$$

This is the intensity as seen on the image plane of the object (where the TV photosurface is placed).

The active area of the photosurface is divided into resolution cells, called pixels. The intensity given by eq. (47) is integrated (averaged) over each pixel (see Chapter V). Recalling eq. (8):

$$E_{2o} = i\ k\ S\ \cos\theta_1\ \exp\{i\ k\ r_o\}/(\pi\ r_o) \tag{8}$$

Then substituting eq. (8) into eq. (47) and averaging over a pixel area, it is found that:

$$\langle I\rangle_{pixel} = K'^2\ \langle\rho^2\rangle + (A/M)^2 - 2K'(A/M)\ \sin(kr_o)\ \langle\rho\rangle \tag{48}$$

where:

$$K' = k\ S\ \cos\theta_1/(\pi\ r_o\ M) \tag{49}$$

2.5.2 The Solution for the Scattering Coefficient with Respect to an Individual Pixel.

Recalling eq.(10):

$$\rho = (F_3/S) \iint \exp(i\mathbf{v}.\mathbf{r})\, dx'\, dy' \tag{10}$$

where the scalar dot product **v.r** is given by relation (12):

$$\mathbf{v}.\mathbf{r} = k\{(\sin\theta_1 - \sin\theta_2 \cos\theta_3)\, x - \sin\theta_2 \sin\theta_3\, y - (\cos\theta_1 + \cos\theta_2)\, \xi\} \tag{12}$$

The integral in eq.(10) is over the object surface and is such that the area under integration has to comply with condition (9), i.e. $S \gg \lambda^2$. To perform the average in eq.(48), eq.(10) has to be transformed to image plane coordinates. Then the following transformation is needed:

$$x = x_v/M \qquad \text{and} \qquad y = y_v/M \tag{50}$$

The linear dimensions of x_v, y_v are those of the pixel size.

On the object surface there exists a definite area , conjugate to a particular pixel area, that contributes with scattered light to the pixel in question. This object area is given by the imaging lens magnification. Whether or not this area in the object space is resolved depends on the lens-aperture arrangement. For this case (vide [14], pp.415) the resolution at the image plane of a lens is the Airy disk:

$$v \sin(0.61\ \lambda/\alpha) \simeq v\ (0.61\ \lambda/\alpha) \tag{51}$$

where v is the distance from the lens to the object image plane, and α is the lens semiaperture. For instance:

$f = 200$ mm, $v = 300$ mm, $\alpha = 10.05$ mm and $\lambda = 0.6328$ μm, eq.(51) gives for the diameter of the Airy disk,

$D = 11.52$ μm or a circular area of $ca = 104.27$ $\mu m^2 \gg \lambda^2$.

Therefore the diameter of the resolution cell at the object surface will be $ca/M = 2ca \gg \lambda^2$. If the object area under inspection is such that $S \gg 2ca$, then condition (9) is satisfied.

2.5.3 Surface Roughness.

Following the analysis on the subject in [13], the change of variables given by relation (50) is substituted into eq.(10), and consequently it is found that:

$$\rho = (F_3/SM^2) \int\int \exp\{-(i/M)(V_x x_v + V_y y_v)\} \exp\{iV_z \zeta(-x_v/M, -y_v/M)\} dx_v dy_v \tag{52}$$

where the integrals are taken over the pixel longitudinal dimensions.

When the average of eq.(52) is taken, only that part containing the surface information is averaged ([13], pp. 73), i.e.

$$\langle\rho\rangle \simeq \langle\exp\{iV_z\zeta\}\rangle \equiv \int_{-\infty}^{+\infty} w(z) \exp\{iV_z z\} \, dz = \chi(V_z) \tag{53}$$

The function $\chi(V_z)$ is the surface characteristic function (a standard roughness parameter) associated with the Gaussian distribution $w(z)$. During the present section the object surface will be treated as if it were a normally distributed surface, in which case ([13], pp. 80):

$$w(z) = (1/\sigma \; (2\pi)^{1/2} \;) \exp\{-z^2/2\sigma^2\} \tag{54}$$

is the one-dimensional normal distribution. σ, the root-mean-square value of ξ, describes the surface roughness. σ^2 is the variance of ξ, so large σ means a very rough surface. Therefore:

$$\chi(V_z) = \exp\{-2(\pi\sigma/\lambda)^2(\cos\theta_1 + \cos\theta_2)^2\} \tag{55}$$

To completely describe the roughness of a surface, the next function is introduced for the autocorrelation coefficient:

$$C(\tau) = \exp\{-\tau^2/T^2\} \tag{56}$$

Eq. (56) describes the density of the surface irregularities, e.g. the distance τ from hills to valleys of the surface. T is the correlation distance for which $C(\tau)$ will drop to e^{-1}.

Substituting eq. (55) in eq. (52) and integrating, it is obtained:

$$\langle\rho\rangle = F_3\ \rho_o \exp\{-2(\pi\sigma/\lambda)^2(\cos\theta_1 + \cos\theta_2)^2\} \tag{57}$$

with

$$\rho_o = \mathrm{sinc}(V_x L_x/M)\ \mathrm{sinc}(V_y L_y/M) \tag{58}$$

L_x and L_y are the pixel half dimensions.

The value of $\langle\rho^2\rangle$ appearing in eq. (48) will be found next (vide [13], pp. 78).

Taking the average of the square of eq. (10) and making the change of variables given in relation (50), it is found that:

$$\langle\rho^2\rangle = (F_3/SM^2)^2 \int\!\!\int_{-x}^{+x} \int\!\!\int_{-y}^{+y} \exp\{(i/M)[V_x(x_{v1} - x_{v2}) + V_y(y_{v1} - y_{v2})]\} \langle\exp\{iV_z(\xi_1 - \xi_2)\}\rangle\, dx_{v1}\, dx_{v2}\, dy_{v1}\, dy_{v2} \tag{59}$$

the integrals extending over the pixel area. Introducing polar coordinates to ease the calculations, e.g.

$$x_{v1} - x_{v2} = r_v\cos\phi \qquad \text{and} \qquad y_{v1} - y_{v2} = r_v\sin\phi \tag{60}$$

eq.(59) transforms to:

$$\langle\rho^2\rangle = (F_3^2/SM^2) \int_0^{\infty}\int_0^{2\pi} \exp((i/M)r_v(V_x\cos\phi + V_y\sin\phi))$$
$$\langle\exp(iV_z(\xi_1 - \xi_2))\rangle r_v\, dr_v\, d\phi \tag{61}$$

Using the identity ([13], pp. 183):

$$J_0(\ (x^2 + y^2)\ ) = 1/2\pi \int_{\theta}^{\theta+2\pi} \exp(\pm\, i\ x\ \cos\phi \pm i\ y\ \sin\phi)\ d\phi \tag{62}$$

and integrating eq.(61) over ϕ gives:

$$\langle\rho^2\rangle = (2\pi F_3^2/SM^2)\int_0^{\infty} J_0(V_{x,y}\ r_v/M)\ \langle\exp(iV_z(\xi_1 - \xi_2))\rangle\ r_v\ dr_v \tag{63}$$

with

$$V_{x,y}^2 = V_x^2 + V_y^2 \tag{64}$$

The two dimensional form of the surface's normal distribution is ([13], pp. 81):

$$w(z_1,z_2) = (1/2\pi\sigma^2)\ (1-C^2)\ \exp(-(z_1^2 - 2Cz_1z_2 + z_2)/(2\sigma^2(1 - C^2))) \tag{65}$$

giving,

$$\langle \exp\{iV_z(\zeta_1 - \zeta_2)\}\rangle = \chi(V_z,-V_z) = \exp\{-V_z^2\sigma^2(1 - C)\} \tag{66}$$

as a result for the characteristic function.

The attention is drawn to the quantity:

$$V_z^2\ \sigma^2 = (2\pi)^2\ (\sigma/\lambda)^2\ (\cos\theta_1 + \cos\theta_2)^2 \equiv g \tag{67}$$

It is noticed that g is proportional to (σ/λ), and thus g can be seen as a parameter measuring the roughness of the surface. There are two extreme cases to consider: a) $g \ll 1$, a slightly rough surface and b) $g \gg 1$, a very rough surface.

C is the general autocorrelation coefficient given by eq.(56). Substituting in eq.(63),

$$\langle \rho^2\rangle = (2\pi F_3^2/SM^2)\int_0^\infty J_0(V_{x,y}r_v/M)\exp\{-V_z^2\sigma^2[1 - \exp(-r_v^2/(MT)^2)]\}\ r_v dr_v \tag{68}$$

where τ has been substituted for r_v/M.

The steps leading to the solution of eq.(68) are lengthy and thus out of the scope of this chapter. The reader interested on how to work out the solution is asked to refer to appendix A.

Then for a surface rough in both dimensions, eq.(68) becomes after considerable manipulation:

$$\langle \rho^2\rangle = e^{-g}F_3^2\{\rho_0^2 + (\pi T^2/S)\sum_{m=1}^{\infty}(g^m/m!\,m)\ \exp\{-(T^2/4m)(V_x^2 + V_y^2)\}\} \tag{69}$$

with the two limiting cases, a)

$$\langle\rho^2\rangle = e^{-g}F_s^2\{\rho_o^2 + (\pi T^2 g/S)\exp\{-(T^2/4)(V_x^2 + V_y^2)\}\} \quad \text{for} \quad g \ll 1 \tag{70}$$

and, b)

$$\langle\rho^2\rangle = (\pi/gS)(F_sT)^2 \exp\{-(T^2/4g)(V_x^2 + V_y^2)\} \quad \text{for} \quad g \gg 1 \tag{71}$$

Eqs. (70) and (71) are the desired relations to be substituted in the interference relation (eq. (48)).

2.5.4 The Solution.

Replacing eqs. (70) and (71) into eq. (48) for the average pixel intensity,

$$\langle I\rangle_{pixel} = K'^2\, e^{-g}F_s^2\{\rho_o^2 + (\pi T^2 g/S)\exp\{-(T^2/4)(V_x^2 + V_y^2)\}\} + (A/M)^2 - 2K'(A/M)\sin(kr_o)\, e^{-g/2}\rho_oF_s \quad \text{for} \quad g \ll 1 \tag{72}$$

and

$$\langle I\rangle_{pixel} = K'^2\, (\pi/gS)(F_sT)^2\exp\{-(T^2/4g)(V_x^2 + V_y^2)\} + (A/M)^2 - 2K'(A/M)\sin(kr_o)\, e^{-g/2}\rho_oF_s \quad \text{for} \quad g \gg 1 \tag{73}$$

with the last term of eq. (73) rapidly going to zero as g increases and less rapidly as ρ_o decreases.

Eqs. (72) and (73) are the final results, describing the interference between the object scattered light and a divergent reference beam (originally the beam was parallel and coming from the object plane) at the image plane of the object. Both eqs. are the result of averaging the intensity given by eq. (47) over the pixel area.

2.6 Results and Discussion.

Computer programs of eqs.(72) and (73) were developed in order to find the pixel intensity along a line on the photosurface. The results for the intensity were scaled as 0 to 255 grey levels and plotted against the corresponding pixel number. To assess the magnitude of the parameter g defined in eq.(67), and thus decide which equation to use for the intensity, the surface roughness throughout was measured using a stylus profilometer (the surface profile obtained can be seen in figure 2.4a):

Object	σ (μm)	σ/λ	g_{max}	Comments
Metal Cantilever	0.023	0.0363	0.21	slightly rough
Ground Glass #1	0.636	1.01	159.51	rough
Ground Glass #2	0.820	1.30	265.16	very rough
Ground Glass #3	4.71	7.44	8748	extremely rough

Data for the ground glasses used to create the speckled reference beams is given for comparison: the metal cantilever used as the test object in this thesis is seen to be a comparatively smooth object. Hence, the results that follow consider plots of eq.(72) only, i.e. for $g \ll 1$. (The ground glasses were prepared using a silicon carbide paste, Carborundum, with different coarseness numbers).

Moreover,an intensity ratio of 2 between the object and reference beams was assumed, i.e.

$$I_r/I_o = 2 \tag{74}$$

i.e., the intensity of the reference beam averaged over the pixel area was twice that of the object. I_o, the object intensity, is given by the first term in eq.(72) and I_r by the second. Then eq.(72) takes the form:

$$\langle I\rangle_{pixel} = K'^2\{ 3\langle\rho^2\rangle - 2 \sin(kr_o) \langle\rho\rangle (2\langle\rho^2\rangle)^{1/2} \} \tag{75}$$

where the $\langle\rho^2\rangle$ and $\langle\rho\rangle$ values corresponding to $g \ll 1$ or $g \gg 1$ are substituted according to the circumstances.

2.6.1 Computer Modelling.

The special case of a small object tilt was modelled in the computer. The process was as follows:

1) Consider that not all the scattered light from a particular object point reaches the conjugate image point, i.e. the scattering angle θ_2 is limited to a range defined by the acceptance cone.

2) Compare an element size on the object surface (corresponding to the conjugate pixel in the image plane) to that of the resolution cell defined by the viewing system to find the number of object points contributing to the pixel at the image plane, e.g. if the horizontal dimension of the resolution cell is one third of the size of an element, there will be three points from the object contributing to the pixel.

3) Calculate eq. (75) for all the allowed scattered rays and contributing object points, within an element, to a single pixel.

4) Repeat the operation for every pixel/conjugate object element.

5) Tilt the object by α degrees.

6) Find the intensity per pixel as in 1 to 4 above.

7) Subtract intensities/pixel before and after rotation.

8) Convert the subtraction values to a 0 to 255 grey scale level, in such a way as to give the minimum value (0) to that pixel whose subtraction value is minimum (negative values were accounted for) and the maximum value (255) to that showing the maximum value on subtraction.

The previous procedure was done for 256 pixels. The tilt was about an axis in the first pixel. The above computation assumed a circular aperture.

Figures 2.5 to 2.11, showed the results for the above computation. The intensity grey level values are plotted in the vertical axis and the pixel number in the horizontal one. The angle of incidence θ_1 was 0° and the tilt angle was increased to have approximately: 3, 5, 6, 35, 70, 100 and 128 fringes respectively. Absolute comparisons, with respect to intensity values, among the plots was not possible due to the way in which the scaling was done. However, it is seen that when the tilt is increased the fringes show a higher noise level (or smaller visibility) than the plots for small tilts.

Figure 2.12 shows two photographs of a computer read-out from fringe patterns (subtraction) obtained when tilting the object. Both, computer simulations and read-outs were done along a horizontal line of the photosurface. It can be noticed that:

1) The computer model of ESPI (eq.(75)) gave fringes that were equally spaced, as expected.

2) The model showed a decreasing envelope on the fringes; this was due to the sinc(x) function appearing in $\langle\rho\rangle$, through ρ_o (eq.(58)). The roots of this function are not equally spaced for small values of its argument, but they asymptotically approach the values:

$$x = (2m + 1)\pi/2 \qquad (76)$$

for large m, m being an integer.

3) Fig. 2.12 showed, as might be expected, an oscillating distribution of intensities along a horizontal axis. The peaks of this intensity distribution did not show an equally spacing behaviour, though the fringes were equally spaced.

The visibility shown in the plots of eq.(75) decreases when the fringe density increases. In this limit the values taken by ρ (per pixel) before and after the object is tilted, combined with a rapidly varying sine function drop the visibility of the fringe patterns.

Thus, to a good approximation, the fringe patterns obtained with eq.(75) model the smoothed fringe distribution for ESPI.

2.7 Closure.

The complex amplitude distribution functions that describe the object and reference wavefronts at the plane of the object image in an ESPI system were found. The more rigorous solution for the analytical form of the object wavefront phase was approached to, by invoking the roughness properties of the object surface. Thus, the intensity found at the image plane was given by eqs.(72) and (73). A computer algorithm was developed for eq.(72) that successfully describes the ESPI system for the case where the intensity was measured pixel by pixel and along a line at the plane of the image.

Finally, it was found that the stringent condition for the reference beam conjugacy can and must be dropped-out from the ESPI experimental design and theory, since it is just an unnecessary mathematical condition and difficult to operate experimental requirement.

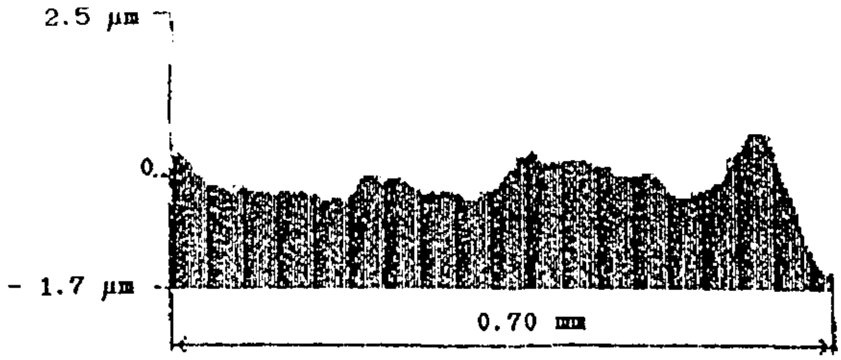

(a)

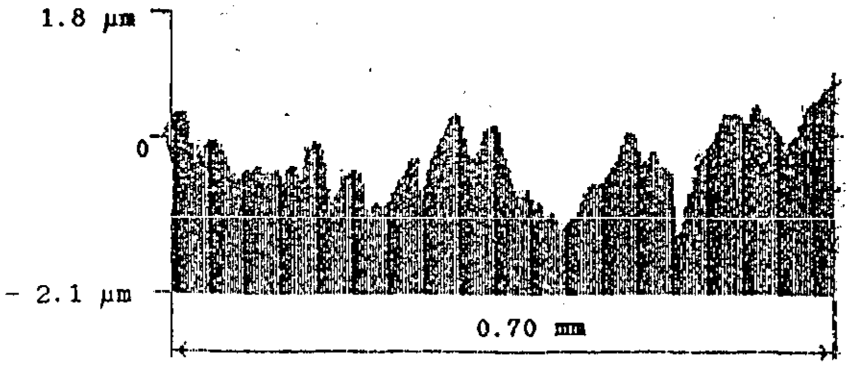

(b)

Figure caption in next page.

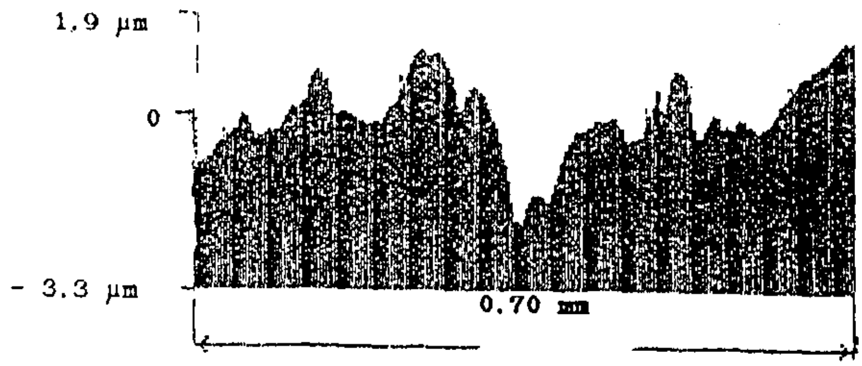

(c)

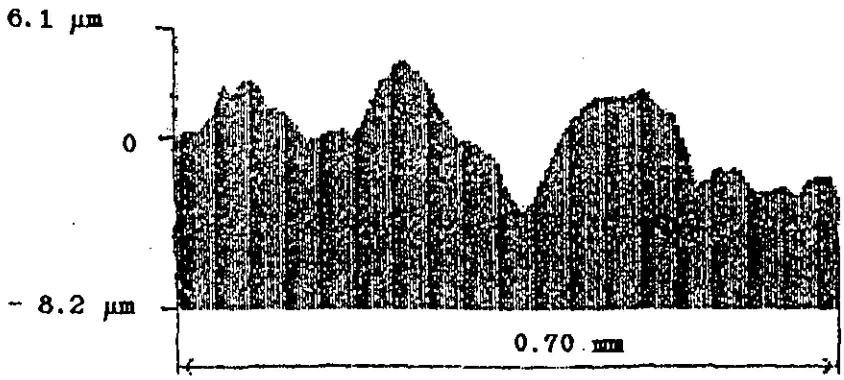

(d)

Figure 2.4
Stylus profiles for: a) Object (cantilever), b) GG #1, c) GG #2, d) GG #3.

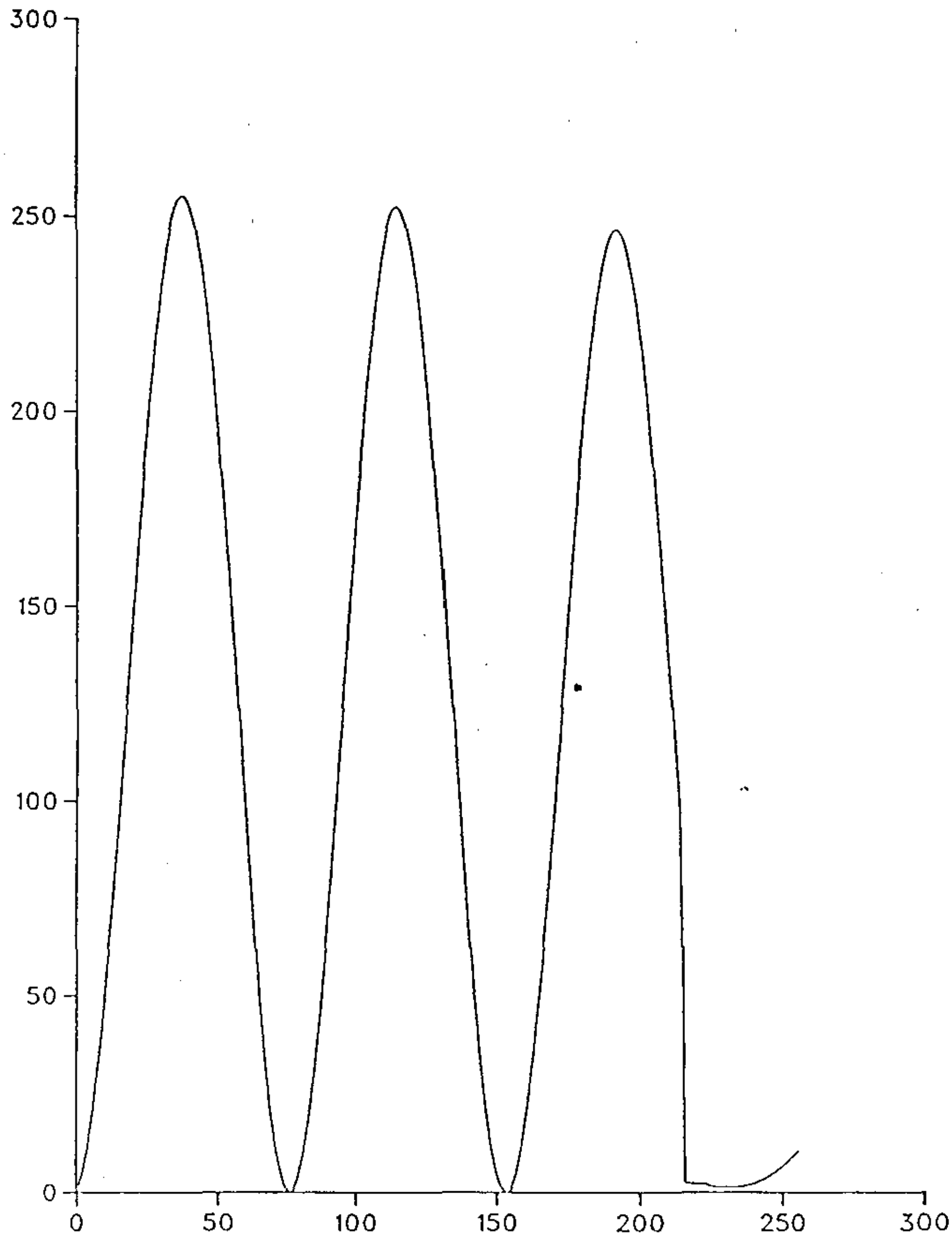

Figure 2.5
Plot of eq.(75) for a circular aperture, $\theta_1 = 0^\circ$ and tilt angle of 0.010°. The vertical axis is for the grey level scale and the horizontal for the pixel number. Three fringes are clearly seen.

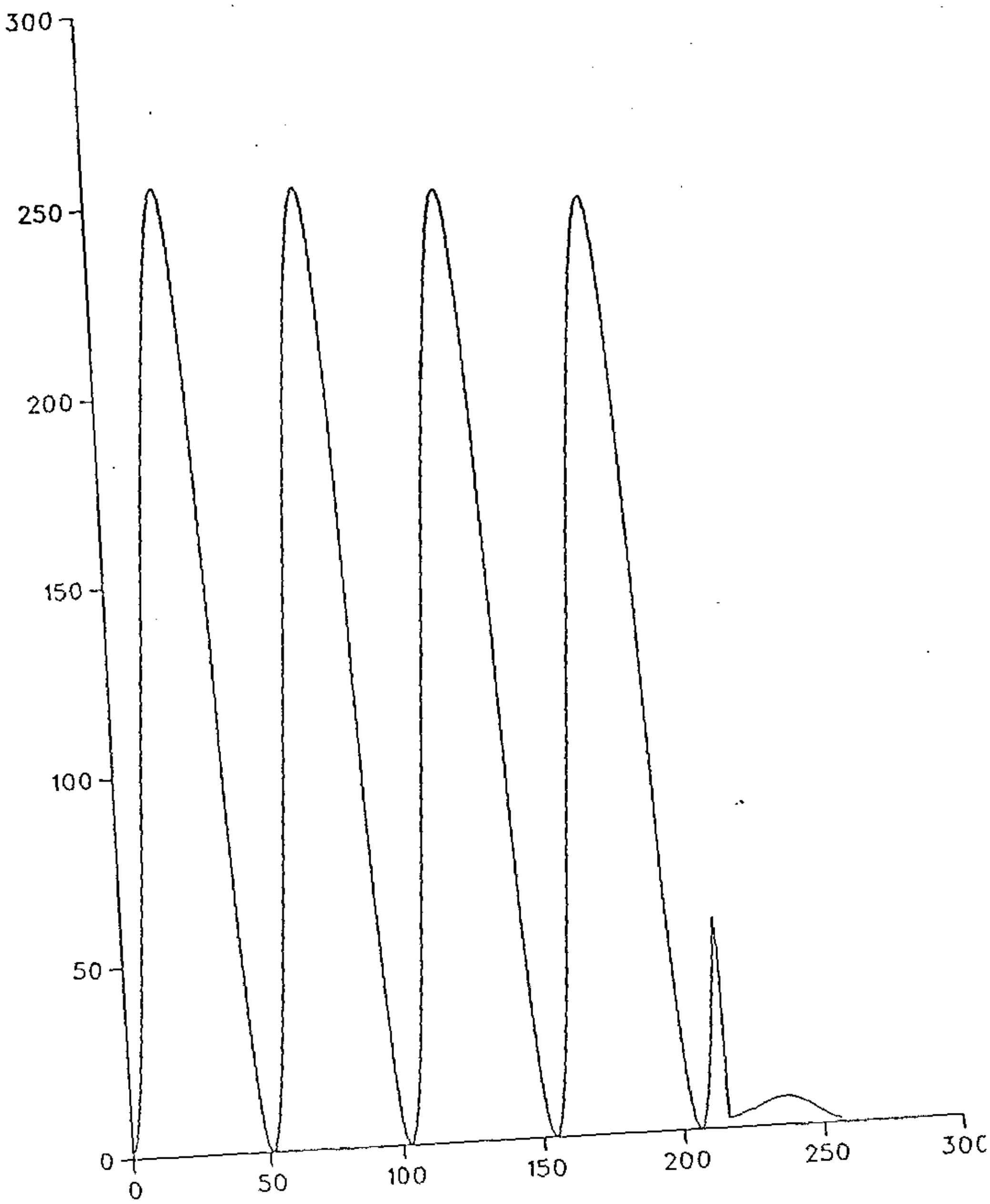

Figure 2.6
As fig. 2.5, but increased tilt to 0.015°.

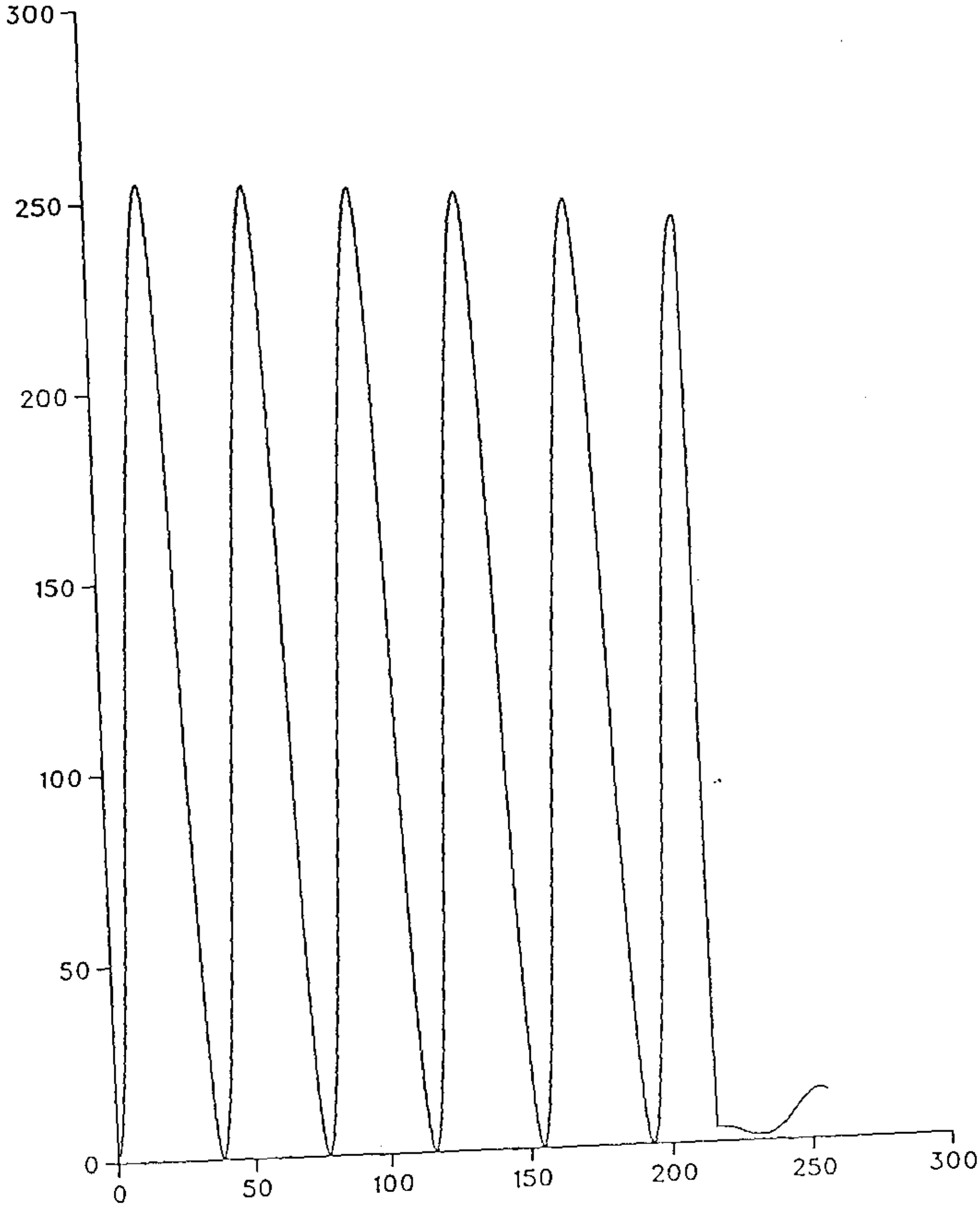

Figure 2.7
As in fig. 2.5. The tilt was 0.020°.

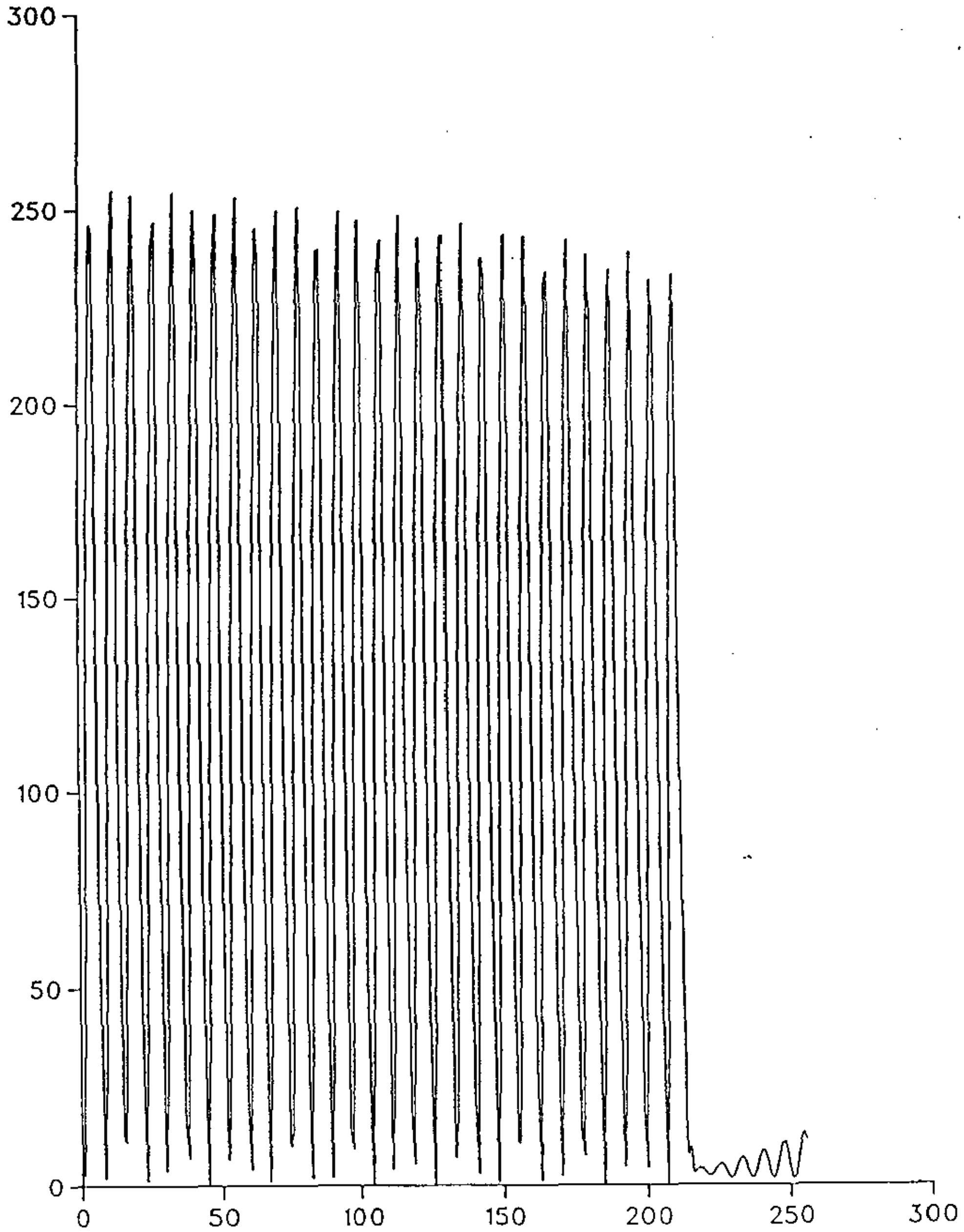

Figure 2.8
As in fig. 2.5. Tilt = 0.105° with about 35 fringes.

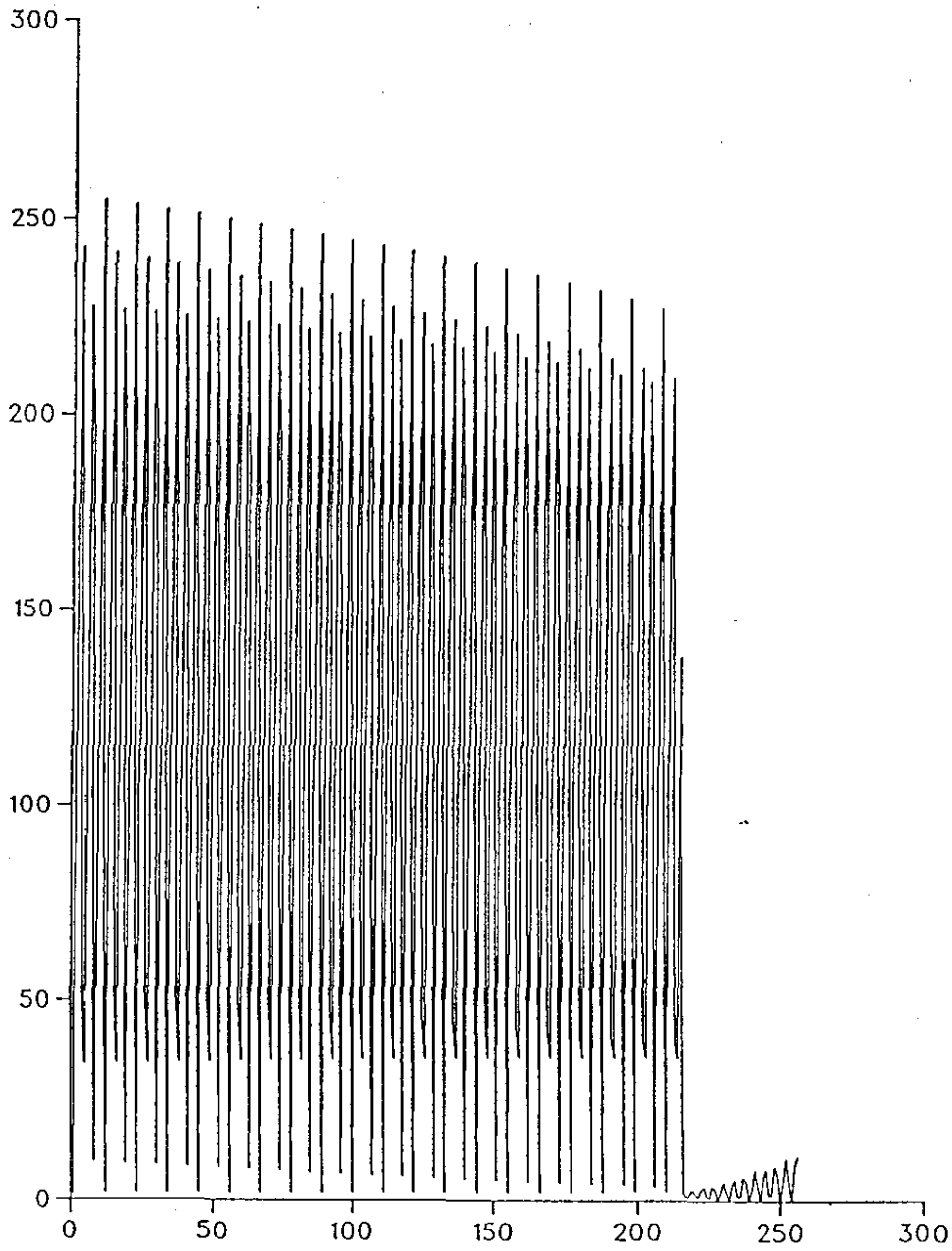

Figure 2.9
As in fig. 2.5. Tilt = 0.211° with about 70 fringes.

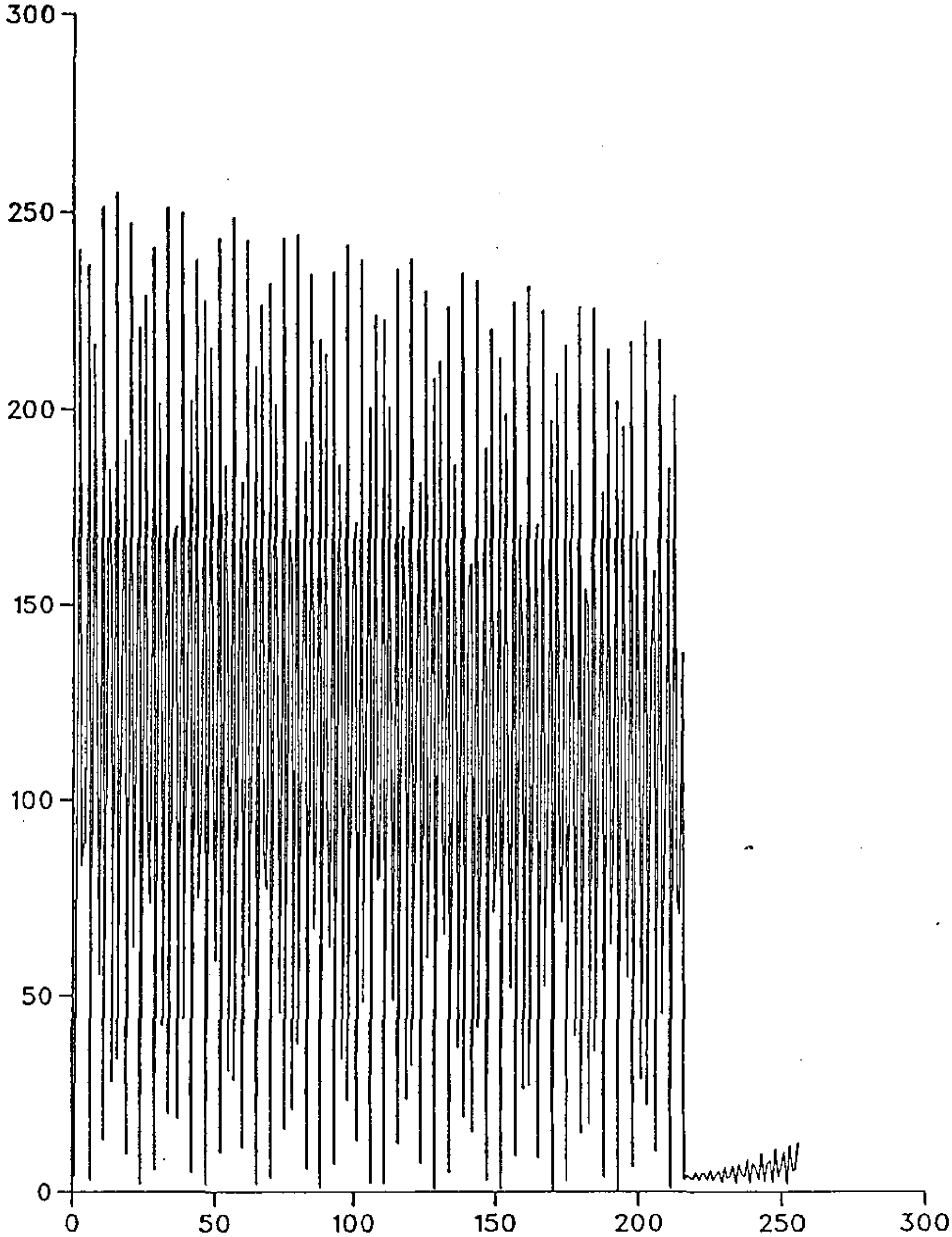

Figure 2.10
As in fig. 2.5. Tilt = 0.302° with about 100 fringes.

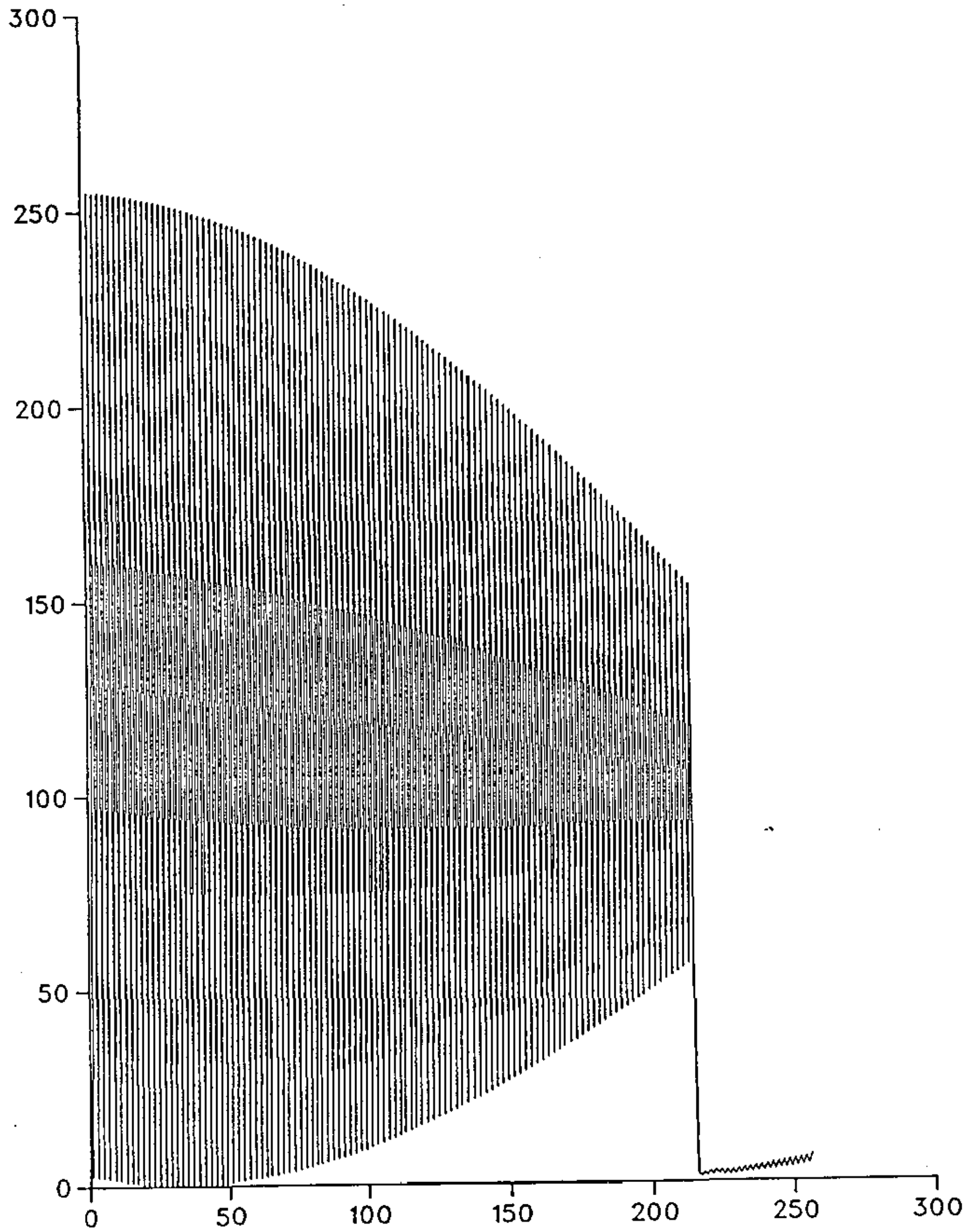

Figure 2.11
As in fig. 2.5. Tilt = 0.386° with about 128 fringes.

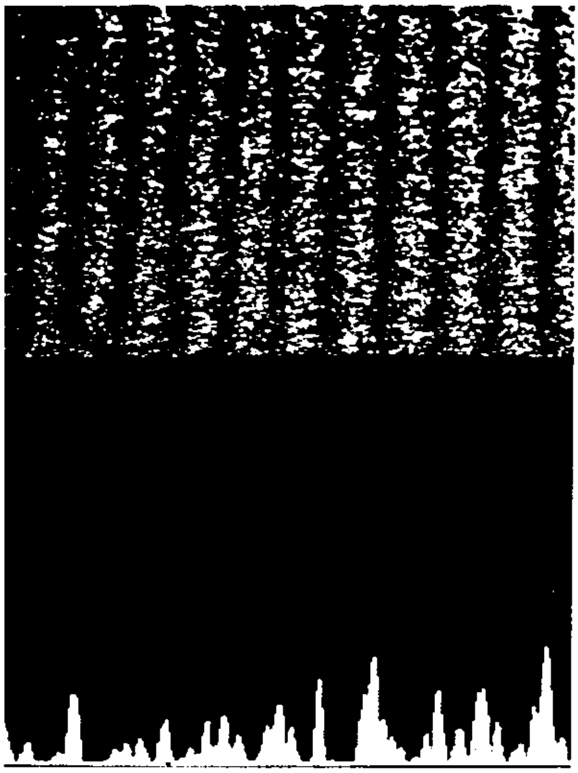

(a)

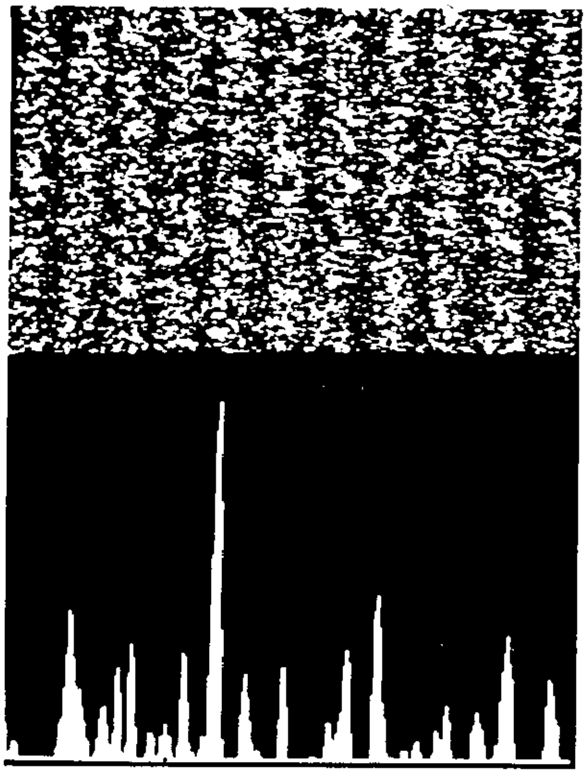

(b)

Figure 2.12
Photographs taken from the TV monitor. They show the intensity readings along a horizontal line on the fringe pattern. The computed visibility is higher in (b).

CHAPTER III
REFERENCE BEAM CONSIDERATIONS.

3.1 Introduction.

To date most of the ESPI systems used substantially rely on the characteristics of the reference beam, namely: divergent form and point of origin, the latter known as the conjugacy requirement (see fig. 3.1). These two features have been seen as requirements for a good overall performance by ESPI, i.e for a good visibility of the displayed fringe patterns. Hence the importance they have played in the design of ESPI.

Good visibility of the fringe patterns as seen from the monitor screen by the eye may not (and in most cases it does not) agree with visibility values given by a computer due to the fact that the eye performs an integration over the fringe pattern displayed.

In Chapter II it was shown that the divergent beam form and point of origin conditions are not necessary and that other forms and points of origin can be used for the reference beam. In particular it is found that the beam splitter can be located in between the object and the imaging lens, simplifying greatly the optical design of ESPI.

The present Chapter shows the experimental response of ESPI to the different geometries for the reference beam, viz: divergent, convergent, parallel, and speckled reference beams.

Several points of origin for the smooth beams will be obtained for two cases: a) where the beam splitter is located in between the imaging lens and the TV photosurface (normal ESPI configuration), and b) the beam splitter is placed in between the object and imaging lens.

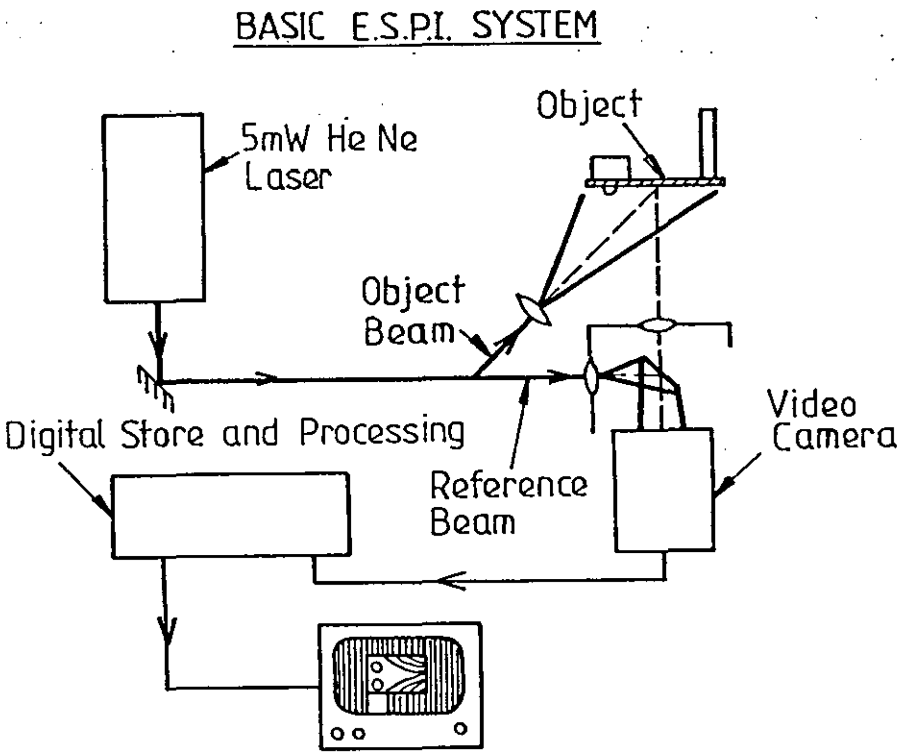

Figure 3.1
Ordinary ESPI lay-out showing optical head using a diverging reference beam appearing to come from the pole of the imaging lens.

As usual with ESPI (as used in subtraction mode), two images are compared within the electronic memory. In this Chapter, the first image is that of the static object and the second is the tilted object (the tilt axis is perpendicular to the optical axis, and passes through the center of the object, see fig. 3.1). Thus, correlation fringes are obtained from the subtraction of the two images. Since the averaging effect of the pixel affects the result, the same number of fringes across the screen (19 vertical) was used throughout.

Thus, the resulting ESPI subtraction fringes are analysed by computer, which carries out readings of intensity along several lines perpendicular to the fringes. The visibility, being an absolute measure of the peak to valley intensity ratio for the fringes, is the most important parameter to be calculated from these patterns, i.e. the visibility values will allow a comparison among the fringe patterns.

For all the results in this Chapter, the visibility is calculated from:

$$V = (I_{max} - I_{min})/(I_{max} + I_{min}) \tag{1}$$

where I_{max} and I_{min} are the overall maximum and minimum average intensities for the bright and dark fringes respectively.

The electronic signal processing in ESPI plays an important role in the visibility of the speckled fringes. The analog to digital (A/D) device introduces noise in the otherwise dark portions of the speckled fringe patterns (subtraction case only). When this is removed the dark fringes should look black.

3.2 Image Processing Routine.

At this point, and since all the fringe patterns will be analysed by computer, it is convenient to describe the steps leading to the evaluation of the subtracted patterns. All the subtraction fringe patterns were obtained from object tilts, a fixed number of vertical fringes being examined every time. Unless otherwise stated, the image processing procedure for all the images is:

a) Store in a floppy disc the subtracted pattern.

b) Read the pixel intensity along 17 different lines across (perpendicular to) the fringes.

c) Find the maxima and minima of intensity for each line and calculate an average for these values.

d) Obtain a final average value for the intensity maxima (I_{max}) and minima (I_{min}) for the whole fringe pattern.

e) Calculate eq.(1), Standard Deviation (σ) for the Mean of the pixel data over the whole field, and Uncertainty (calculated from eq.(1) in the usual way) for the visibility of every pattern.

A DEC PDP 11-23 mini computer was used for the analysis throughout the Chapter.

3.3 Beam Splitter Behind the Lens.

3.3.1 Divergent Reference Beam.

The optical head of the interferometer is shown in figure 3.2. Here the reference point source, formed with the usual microscope/spatial filter combination, is mounted on a translation stage that can be moved back or forth in a direction perpendicular to that of the system optical axis (e.g. along the reference beam axis), thus having the availability of a diverging beam with different radii of curvature at the plane of the object image.

For the divergent, convergent and parallel beam experiments in this section (BS behind imaging lens) the following parameters were kept constant: imaging lens-aperture combination set to f/25, the focal length of the imaging lens (200 mm), the object to imaging lens distance (600 mm), distance from lens to beam splitter (80 mm), and the number of vertical correlation fringes obtained on subtraction. A He-Ne 10 mW laser at λ = 0.6328 μm is used throughout the Chapter.

Table I, shows the results for the divergent beam for two different intensity ratios (r = ratio of the reference to object beam intensities); the distance given is that measured from the origin of the point source to the beam splitter (BS).

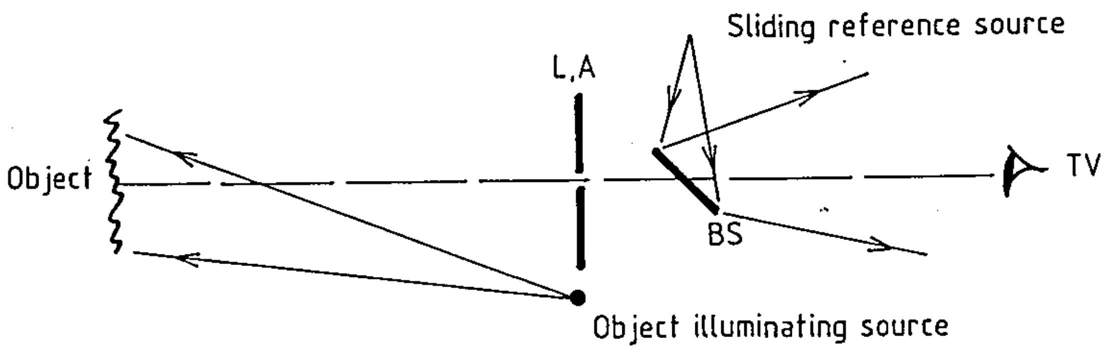

Figure 3.2
Optical setting for the sliding reference beam.
The discrete motion is along the beam axis.

Table III

ratio (r)	Visibility	Uncertainty x 10^{-2}
2	0.3447	7.95
3	0.3417	6.09
4	0.3250	2.25
6	0.2857	7.08
7	0.3034	7.78
8	0.3135	5.98
9	0.2978	7.83

3.3.4 Oscillating Speckled Reference Beam.

With reference to figure 3.7, a piezoelectric mirror, driven by a sine square frequency oscillator, is employed to sweep (with a definite frequency) a convergent laser beam over the surface of a ground glass, such that the light scattered from it serves as the source for the speckled reference beam. Three different ground glasses were used for every scanning frequency. Some useful parameters, also cited in Chapter II, for these ground glasses are:

Ground Glass No.	σ (μm)	σ/λ
1	0.636	1.01
2	0.820	1.30
3	4.71	7.44

The last column representing a measure of the glass surface ptical roughness.

Table I

Distance (mm)	r	Visibility	Uncertainty x 10^{-2}
74)	8	0.3710	8.06
	2	0.4409	9.51
76)	8	-	-
	2	0.4305	8.61
78)	8	0.3982	6.89
	2	0.4246	10.64
79)	8	0.4079	6.58
	2	0.4341	9.84
80)	8	0.4075	6.79
	2	0.4432	11.23
81)	8	0.4331	6.49
	2	0.4027	6.04
85)	8	0.4400	7.43
	2	0.4712	7.98
90)	8	0.4198	10.49
	2	0.3985	9.18
95)	8	0.3983	7.31
	2	0.4557	10.98

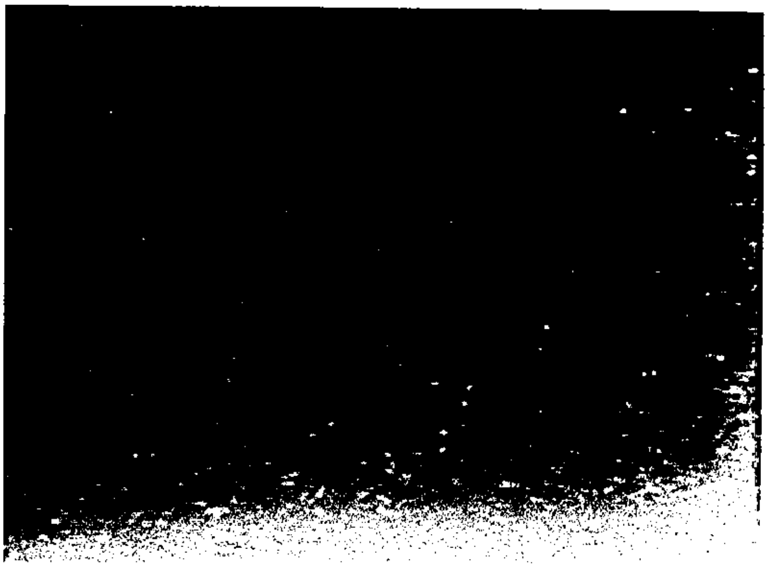

(a)

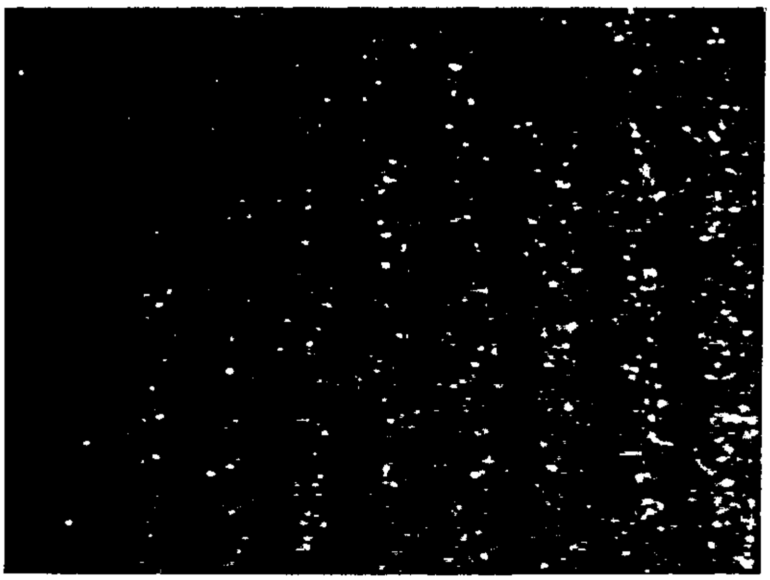

(b)

Figure 3.3
Photographs showing 9 fringes for: (a) r = 2, V = 0.4712 and (b) r = 8, V = 0.4400.

From the above data it can be seen that although the eye perceives a better picture when r = 8 (fig. 3.3b), the computer readings show that the visibility values are higher for r = 2 (fig. 3.3a).

3.3.2 Convergent Reference Beam.

Figure 3.4 shows the optical set-up for the convergent/parallel reference beams. The convergent beam has its point of convergence behind the TV camera plate, i.e. converging wavefronts arrive at the object image plane. The distance to be measured in this case is that from this point of convergence to the beam splitter. By moving the microscope/spatial filter combination with respect to lens l_2 different radii of curvature are obtained for the wavefronts at the plane of the object image. The results of this experiment are contained in table II for two intensity ratios. Figure 3.5 displays 9 fringes obtained on subtraction for r = 2 and r = 8.

For these data the visibility values are higher for r = 2. The visibility increases for larger radius of curvature of the converging wavefront, i.e. flatter curvatures give better visibilities.

3.3.3 Parallel Reference Beam.

Locating the point source (see fig. 3.4) at the focal point of lens L_2 creates a parallel beam used as reference beam at the plane of the object image. In this case the visibility of the correlation patterns is investigated as a function of the beam ratio r. Table III depicts the results for this case.

Figure 3.6 show two images from Table III. The best value for the visibility is found when r = 2. From this and the results in previous subsections it can be said that the optimum curvature for the reference beam will be that of a converging beam having a slight curvature.

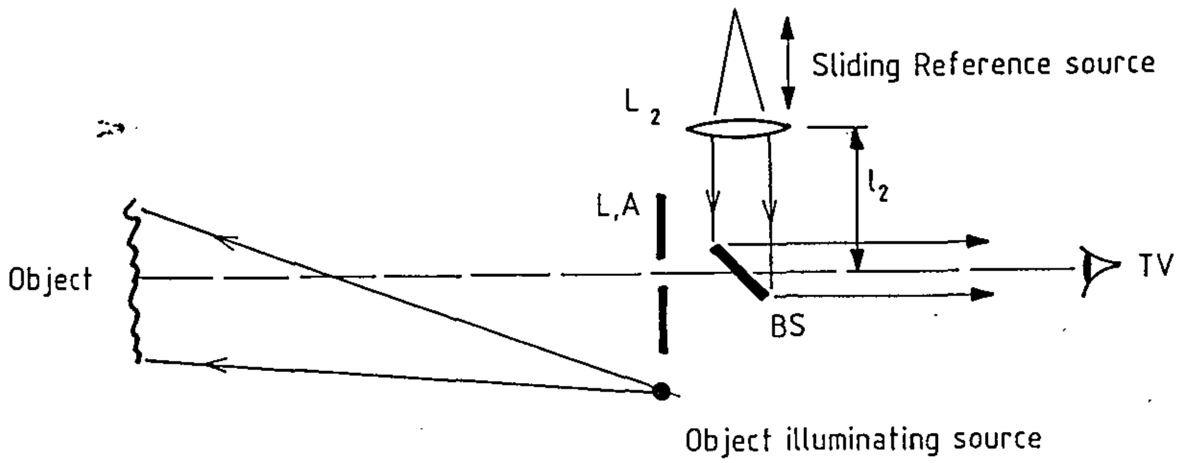

Figure 3.4
Set-up for the Convergent/Parallel reference beam. Distance l_2 to BS = 95 mm, Focal length L_2 = 200mm.

Table II

Distance (m)	r	Visibility	Uncertainty x 10^{-2}
8.105	8	0.3033	7.72
	2	0.3428	7.23
6.772	8	0.3396	8.04
	2	0.3633	8.87
5.43	8	0.3481	7.11
	2	0.3995	9.06
4.81	8	0.3435	7.36
	2	0.3874	7.89
4.105	8	0.2989	8.66
	2	0.3912	8.37
3.74	8	0.3183	7.40
	2	0.3919	7.62
3.18	8	0.3259	5.77
	2	0.4170	8.14
2.77	8	0.3372	6.24
	2	0.3922	9.71
2.21	8	0.3361	8.94
	2	0.3868	6.67
1.92	8	0.3455	6.53
	2	0.3691	6.68
1.64	8	0.3221	8.24
	2	0.3865	6.53
1.15	8	0.3235	8.08
	2	0.3823	8.62

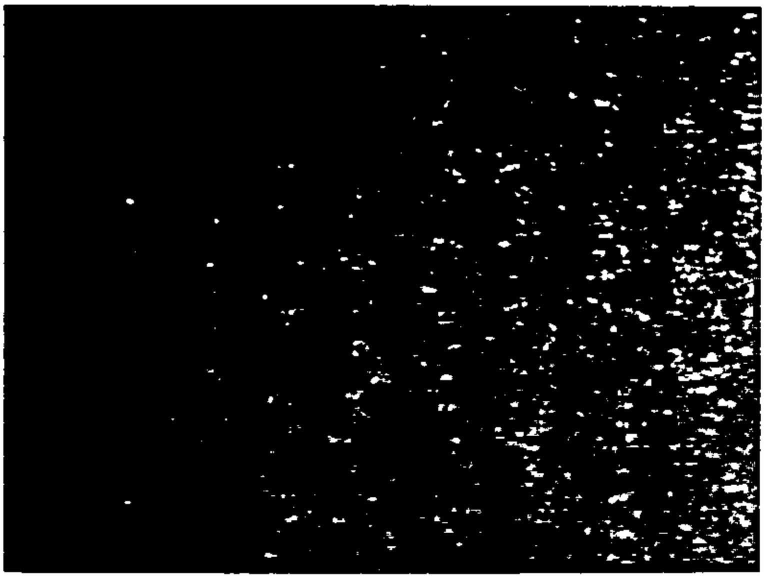

(a)

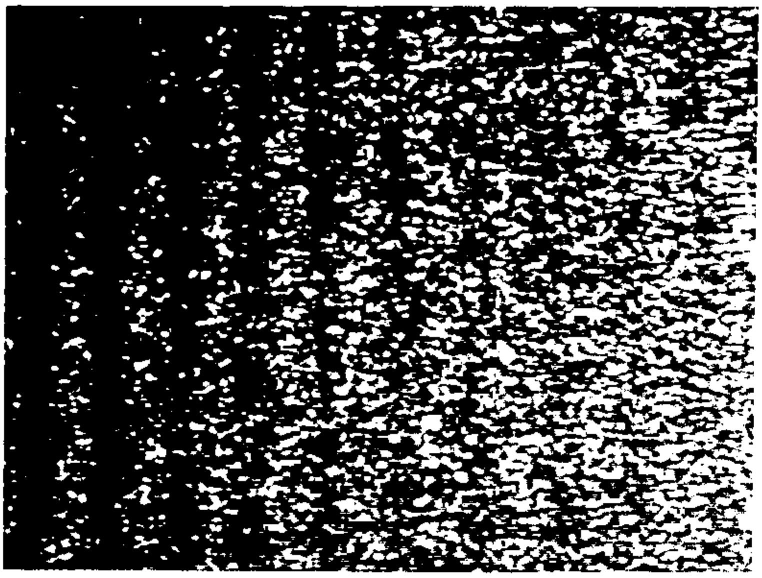

(b)

Figure 3.5
(a) $r = 2$, $V = 0.4170$ and (b) $r = 8$, $V = 0.3259$.

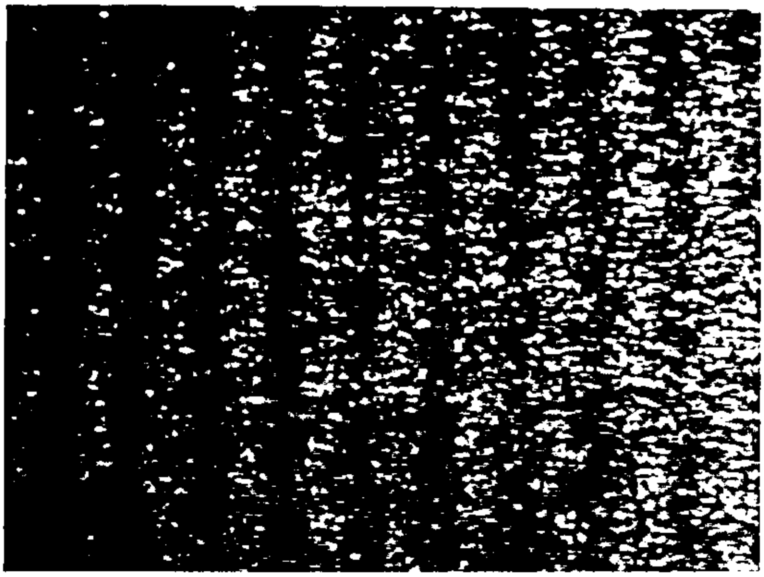

(a)

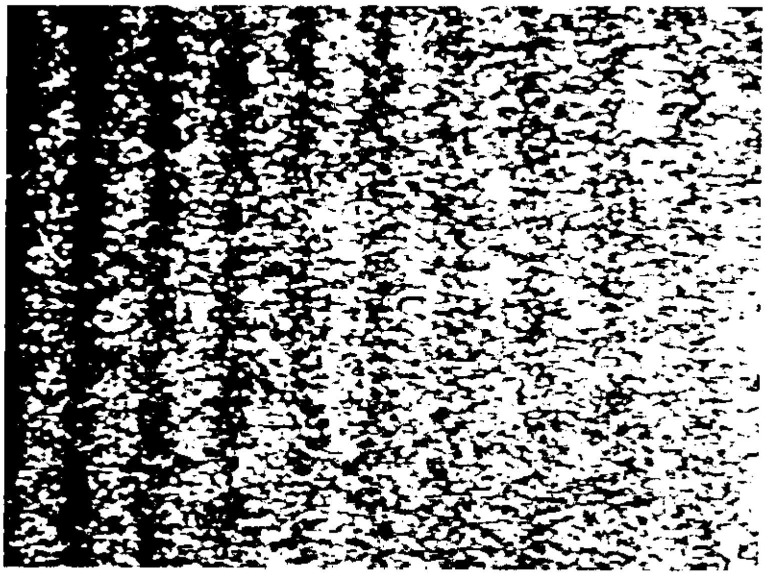

(b)

Figure 3.6
Photographs for a parallel reference beam: (a) $r = 2$, $V = 0.3447$ and (b) $r = 8$, $V = 0.3135$.

Table III

ratio (r)	Visibility	Uncertainty x 10^{-2}
2	0.3447	7.95
3	0.3417	6.09
4	0.3250	2.25
6	0.2857	7.08
7	0.3034	7.78
8	0.3135	5.98
9	0.2978	7.83

3.3.4 Oscillating Speckled Reference Beam.

With reference to figure 3.7, a piezoelectric mirror, driven by a sine square frequency oscillator, is employed to sweep (with a definite frequency) a convergent laser beam over the surface of a ground glass, such that the light scattered from it serves as the source for the speckled reference beam. Three different ground glasses were used for every scanning frequency. Some useful parameters, also cited in Chapter II, for these ground glasses are:

Ground Glass No.	σ (μm)	σ/λ
1	0.636	1.01
2	0.820	1.30
3	4.71	7.44

The last column representing a measure of the glass surface optical roughness.

The results for this experiment are given in table IV, for which the following data is used:

- Imaging lens focal length → $f = 200$ mm.
- Aperture Diameter → $a = 20$ mm.
- Object to imaging lens distance → $u = 600$ mm.
- Converging spot diameter (on GG) → $d = 5$ mm.
- Amplitude of mirror drive → $m = 0.1$ V peak to peak.
- Ratio of reference to object beam intensities → $r = 2$.
- $l_1 = 50$ mm.
- $l_2 = 65$ mm.
- The columns Mean and S.D. in table IV are taken over the whole field, i.e. for the whole fringe pattern (The high contrast of the images being reflected in the closeness of the mean and SD).

The results in table IV show an overall increase in visibility as compared to those values obtained previously. The reason for this increment is due to the averaging process carried while oscillating the speckled beam, reducing the optical noise and thus facilitating the subtraction process within the ESPI electronic apparatus.

In figure 3.8, 9 subtraction fringes are seen on the photographs taken at 140 Hz, for: (a) Ground Glass (GG) 1, (b) GG 2 and (c) GG3.

TABLE IV

Frequency (Hz)	Visibility	Uncertainty x 10^{-2}	Mean	S.D.	GG#
	0.5015	8.29	27.80	17.93	1
0)	0.4772	10.57	35.49	21.90	2
	0.4901	9.36	31.95	22.01	3
	0.3950	9.57	29.44	15.74	1
25)	0.4178	10.41	28.88	16.43	2
	0.4251	8.55	28.16	16.88	3
	0.3901	9.33	30.86	16.90	1
50)	0.4596	8.96	32.00	19.24	2
	0.4492	7.44	32.94	19.52	3
	0.5424	9.35	26.96	19.85	1
140)	0.5578	9.97	27.40	19.37	2
	0.4848	11.19	29.64	20.18	3
	0.4597	13.46	21.91	14.26	1
280)	0.5504	7.60	13.72	11.21	2
	0.5230	9.30	25.11	17.63	3
	0.4859	11.11	28.10	19.03	1
560)	0.5584	7.15	34.05	24.83	2
	0.5153	10.03	34.97	23.39	3
	0.5027	9.07	31.05	21.67	1
1400)	0.4771	8.30	31.93	21.54	2
	0.5264	7.86	33.12	23.05	3
	0.4820	11.63	31.75	20.13	1
2860)	0.5536	9.20	33.69	23.45	2
	0.5286	8.15	31.98	23.04	3
	0.5140	11.35	31.28	22.50	1
4200)	0.5655	6.60	30.43	21.73	2
	0.5003	11.60	33.44	24.72	3
	0.4794	9.32	30.79	20.74	1
6840)	0.5400	10.08	30.56	23.14	2
	0.5168	8.93	30.90	20.75	3
	0.4792	7.30	30.96	20.57	1
12090)	0.5673	8.37	31.77	22.35	2
	0.4787	10.85	34.83	23.80	3
	0.4861	8.75	29.85	20.99	1
15000)	0.5474	8.64	29.92	22.11	2
	0.5197	7.18	32.36	22.85	3
	0.5119	8.96	29.03	20.41	1
16230)	0.5425	9.61	31.96	23.38	2
	0.4760	7.92	34.53	22.58	3
	0.4422	10.88	31.94	20.07	1
19230)	0.4927	11.50	29.62	20.81	2
	0.5040	5.85	35.16	23.04	3

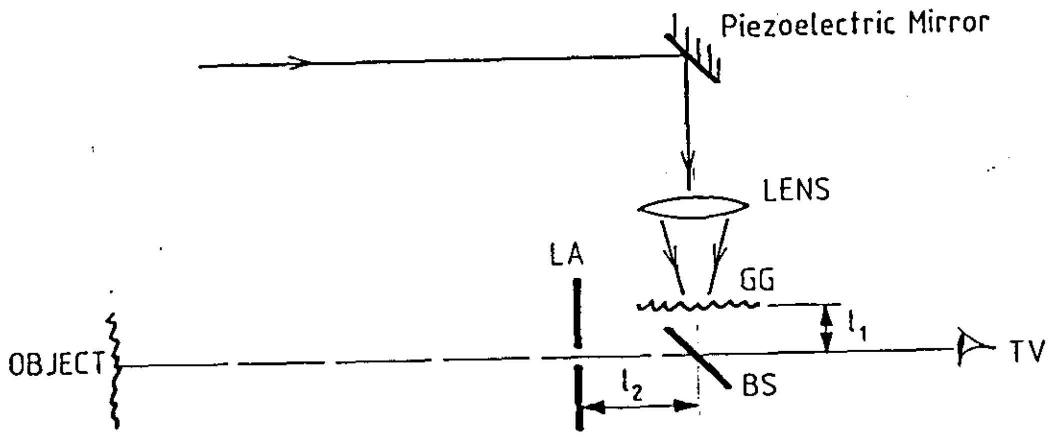

Figure 3.7
Optical set-up for the speckled reference beam.
GG is the ground glass, BS the beam splitter, l_1 is the GG to BS distance and l_2 is the BS to imaging lens distance. The lens L is used to converge the beam on the GG.

3.3.5 Stepping Speckled Reference Beam.

Figure 3.9 shows an optical arrangement for which the experiment consists in stepping the ground glass in a perpendicular direction to that of the illuminating convergent beam. The stepping distance given to the ground glass was of 10 μm at a time, i.e. a distance of the order of the average speckle size (7.72 μm) for the system given in the previous subsection.

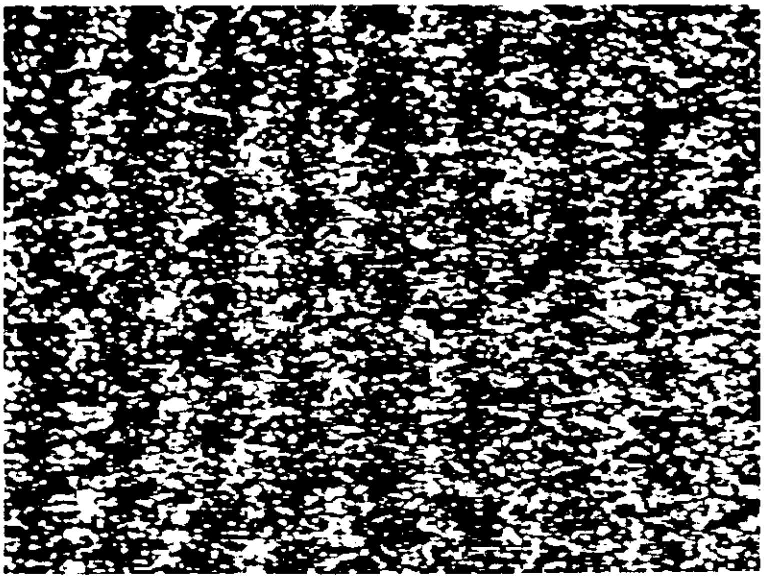

(a)

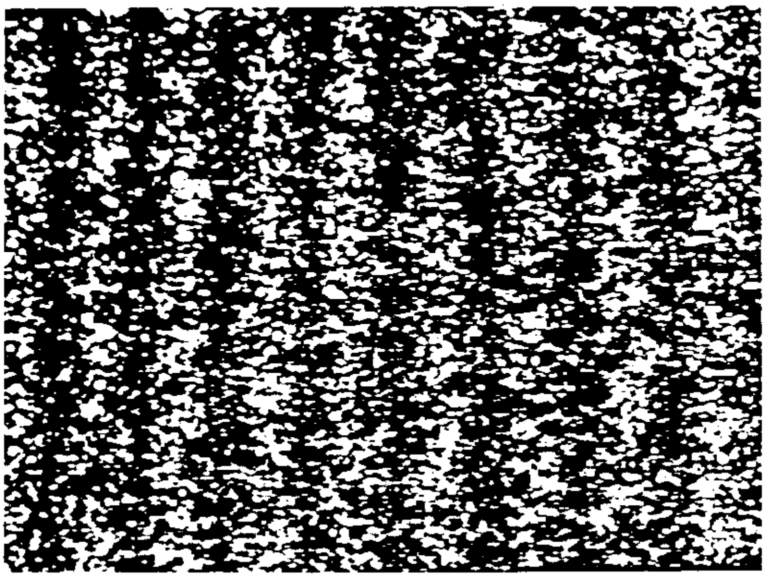

(b)

Figure caption in next page.

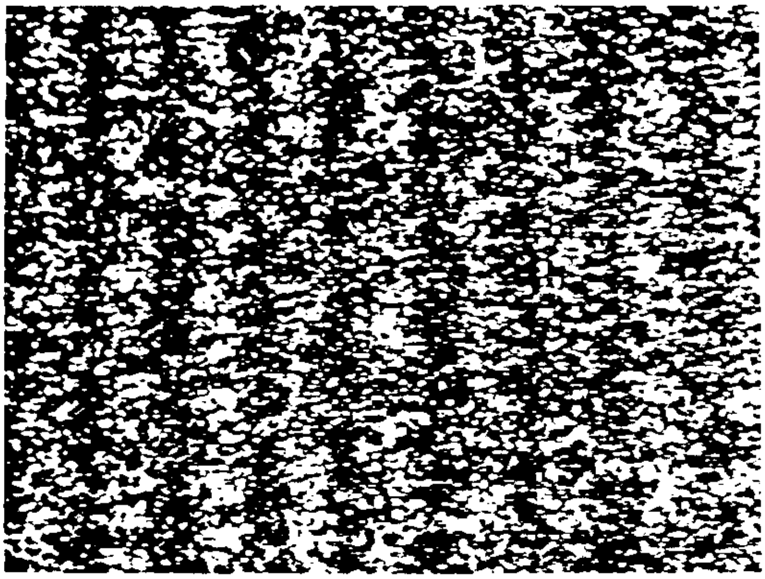

(c)

Figure 3.8

Photographs showing fringes obtained on subtraction using an oscillating speckled reference beam.

(a) V = 0.5424, (b) V = 0.5578 and (c) V = 0.4848.

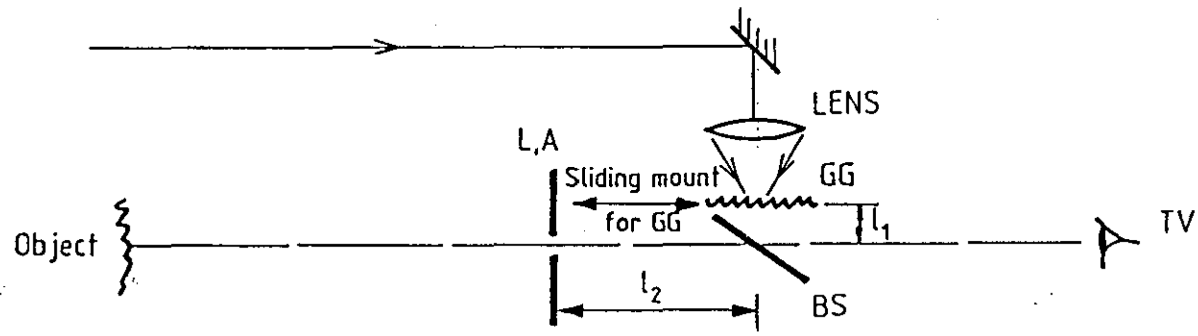

Figure 3.9
Lay-out for the translating ground glass (GG).
The motion is done in discrete steps of 10 μm at a time.
The terminology is the same as that in fig.3.4

Due to the nature of the experiment the image processing routine is slightly different from that described in section 3.2. The procedure is as follows:

a) Capture in a floppy disc 8 different correlation patterns, each with the same number of correlation fringes as the others. These patterns correspond to 8 discrete positions of the ground glass.

b) Form an average of these 8 patterns, displaying the final averaged image for processing.

c) Use procedure in section 3.2, starting in (b).

To compare these results a single correlation pattern chosen from any of the images obtained in part (a) above is analysed following the procedure in section 3.2. Table V shows the results for this subsection: the values of the visibility are shown for the corresponding number (in brackets) of processed patterns.

Table V

Ground Glass	1	2	3
Visibility(1)	0.4039	0.3721	0.3611
Uncertainty x 10^{-2}	8.72	7.01	8.64
Mean	26.78	28.56	29.27
S.D.	15.01	14.85	14.97
Visibility(8)	0.1908	0.1717	0.1505
Uncertainty x 10^{-2}	8.86	5.99	6.22
Mean	26.07	28.04	29.34
S.D.	6.44	6.5	6.43

The photographs in figure 3.10 depict the above results.

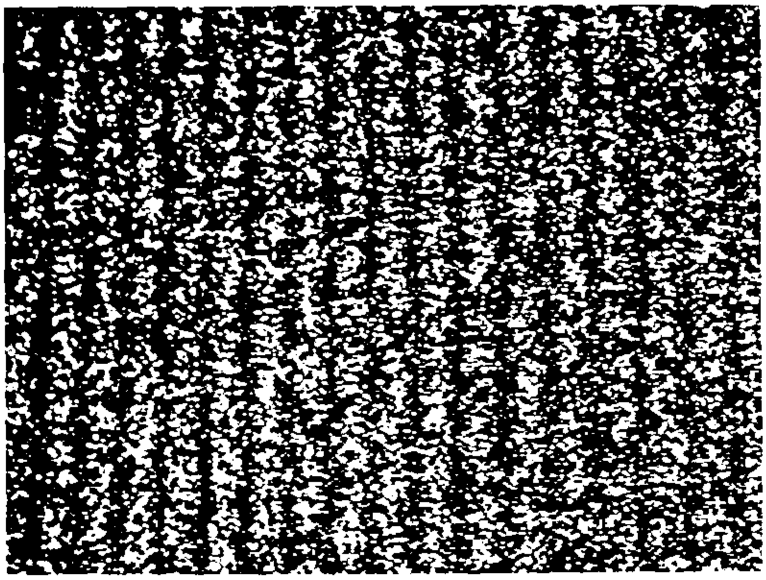

(a)
Single pattern

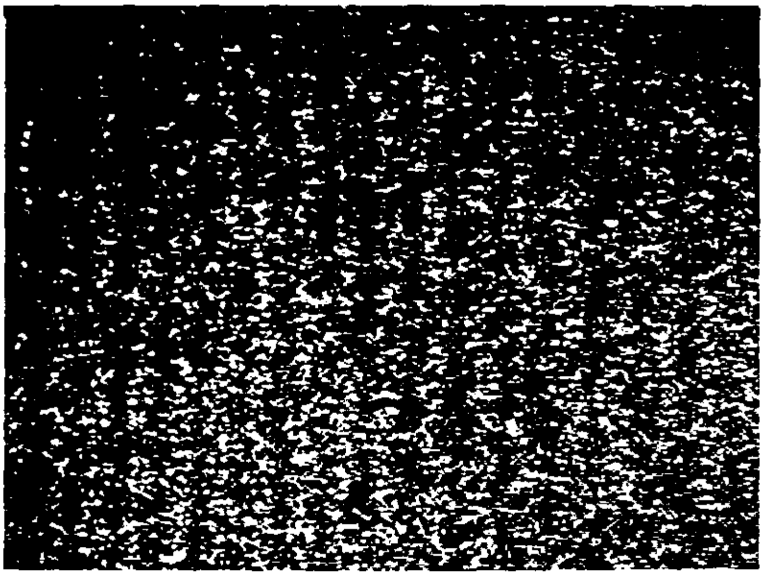

(b)
Average of 8 patterns.
Ground Glass 1. Visibilities as in Table V.

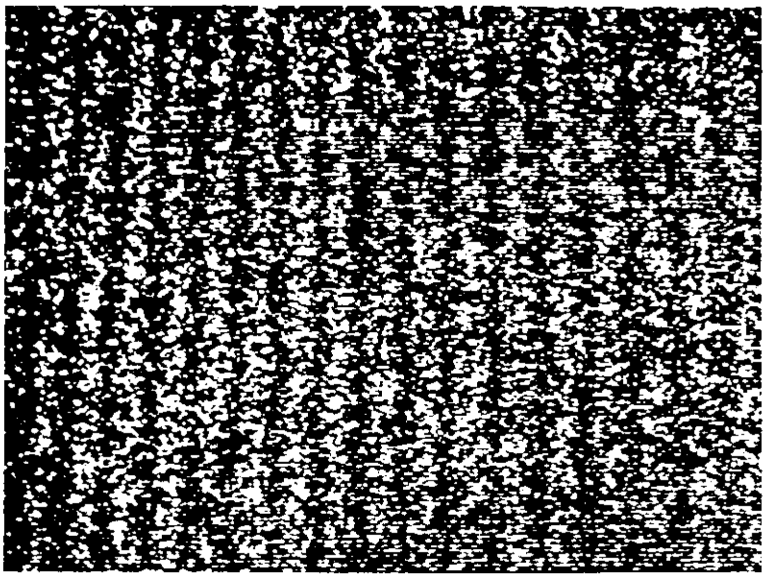

(c)
Single pattern

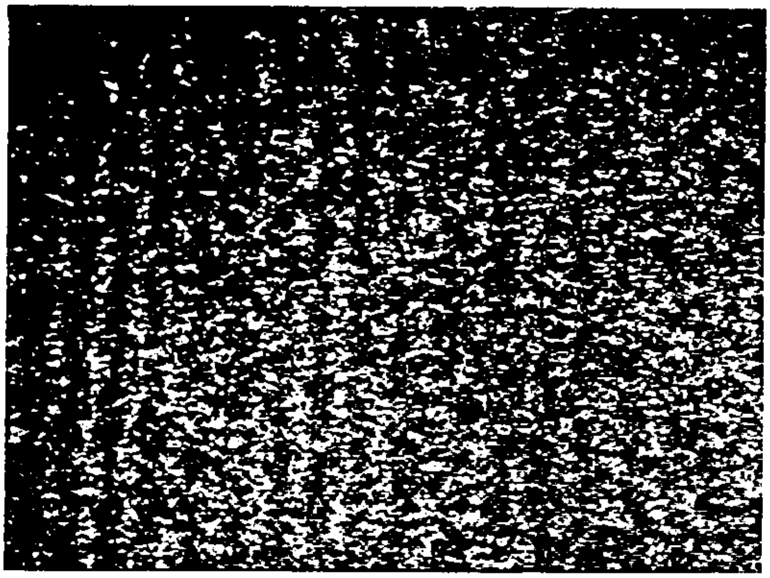

(d)
Average of 8 patterns.
Ground Glass 2. Visibilities as in Table V.

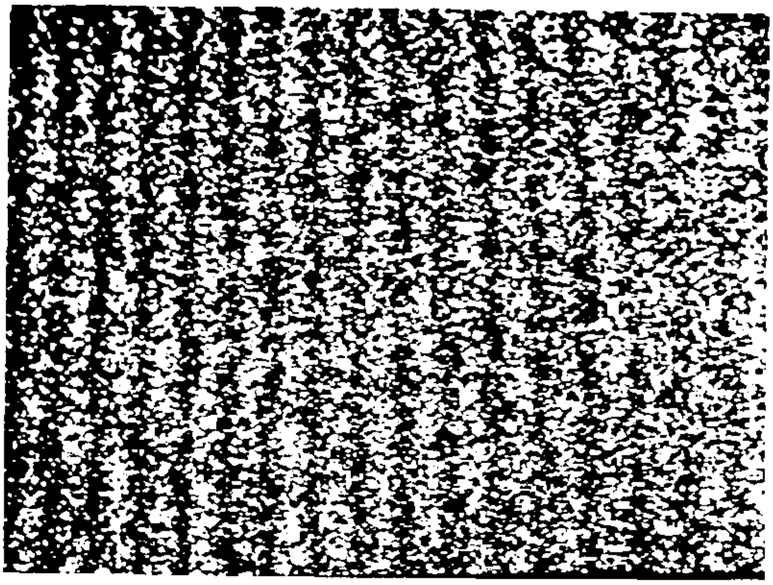

(e)
Single pattern

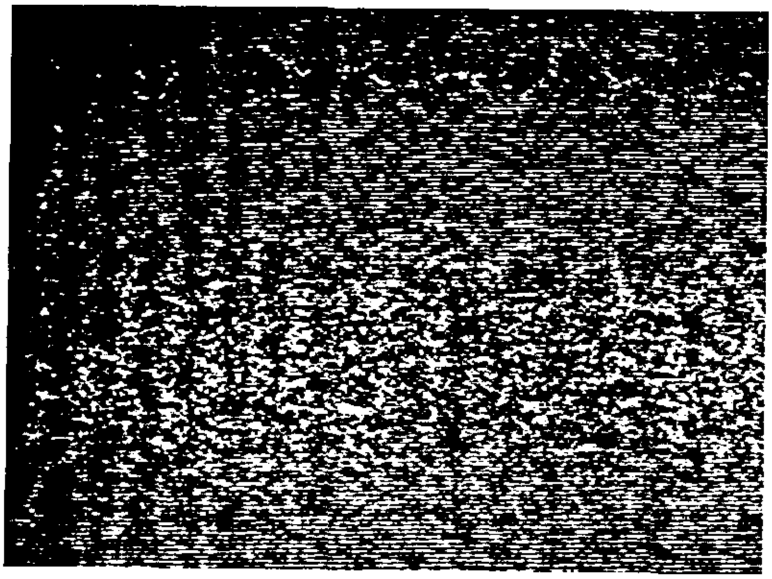

(f)
Average of 8 patterns.
Ground Glass 3. Visibilities as in Table V.
Figure 3.10

The difference between the visibility values for the case of a single and 8 processed patterns is noticed (viz., fig. 3.10). The discrepancy arises because of the impossibility to match exactly the position of the fringes corresponding to 8 patterns having the same number of fringes (they move due to air currents, etc.).

3.4 Beam Splitter in Front of the Lens.

3.4.1 Divergent Reference Beam.

With reference to figure 3.11 a microscope/spatial filter arrangement is mounted on a translation stage that allows it to move in a direction perpendicular to the system optical axis. In this way, and depending on the original position of the filter arrangement with respect to the imaging lens focal point, the reference beam curvature at the plane of the object image can be changed from divergent to convergent or viceversa (the parallel beam case is included in the divergent beam experiment). In this section the parameters associated with fig. 3.11 are:

- Imaging lens focal length → $f = 200$ mm.
- Aperture Diameter → $a = 22$ mm.
- Object to imaging lens distance → $u = 600$ mm.
- ratio of reference to object beam intensities → $r = 2$.
- $l_1 = 105$ mm.
- l_2 is the distance from the point source to the BS, and is variable.

The results in table VI are for a diverging wavefront at the plane of the object image. For $l_2 = 95$ mm the wavefront is plane.

TABLE VI

l_2 (mm)	Visibility	Uncertainty x 10^{-2}
95	0.4026	5.55
92	0.4163	6.30
89	0.4493	5.57
86	0.4371	7.76
83	0.4505	6.07
81	0.4226	7.61
79	0.4101	5.45
77	0.4537	5.29
75	0.4490	6.62
73	0.4555	5.06
70	0.4362	7.85

Since the reference beam is coming from a point in between the imaging lens focal point and the imaging lens, the true origin of the diverging wavefront is imaginary and it does not coincide with the actual physical position of the point source. The visibility data here is slightly higher than its equivalent case where the beam splitter is between the object image plane and viewing lens.

Figure 3.12 shows 9 fringes across the photograph for r = 2.

3.4.2 Convergent Reference Beam.

Reference is made again to fig. 3.11 and parameters associated to it, with the exception that l_1 = 215 mm, for the convergent beam to be feasible (its convergency point lies behind the TV camera plate, so converging wavefronts are impinging that plane). Table VII shows the results for this experiment where again r = 2.

TABLE VII

l_2 (mm)	Visibility	Uncertainty x 10^{-2}
70	0.4374	4.76
73	0.4222	7.54
75	0.4632	7.27
78	0.4579	5.67
81	0.4433	7.74
83	0.4750	6.19
86	0.4663	6.75
89	0.4337	6.91
92	0.4160	7.36
95	0.4456	8.75

The data shows an overall improvement with respect to its analogue case where the beam splitter is located behind the lens. In the present experiment when the point source (microscope/spatial filter combination) is taken away from the beam splitter the curvature of the beam increases on the TV plate. When the point source originates at the same distance than that of the object to imaging lens, the reference beam converges on the TV plate. Taking it further away creates a diverging wavefront on the TV plate. Table VII does not deal with the last two possibilities.

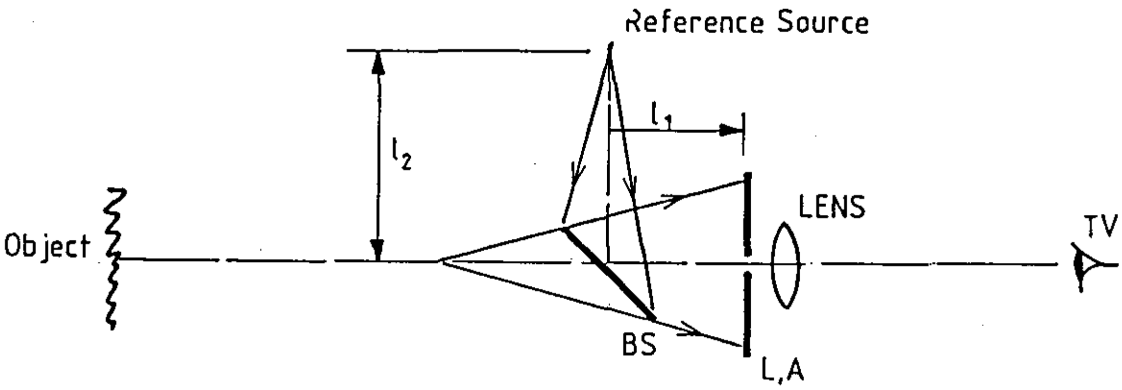

Figure 3.11
Optical head of the interferometer showing the beam splitter (BS) in between the object and the imaging lens. The microscope/spatial filter combination is mounted on a translation stage.

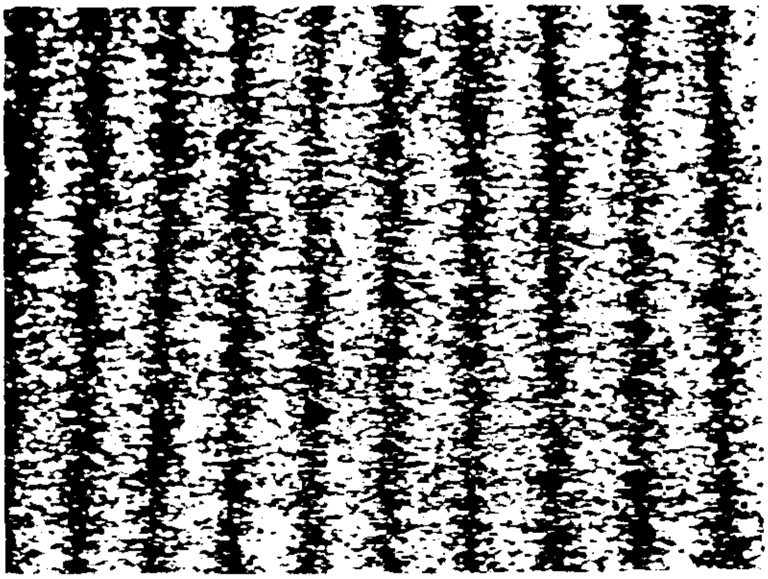

Figure 3.12
Divergent reference beam. V = 0.4555.

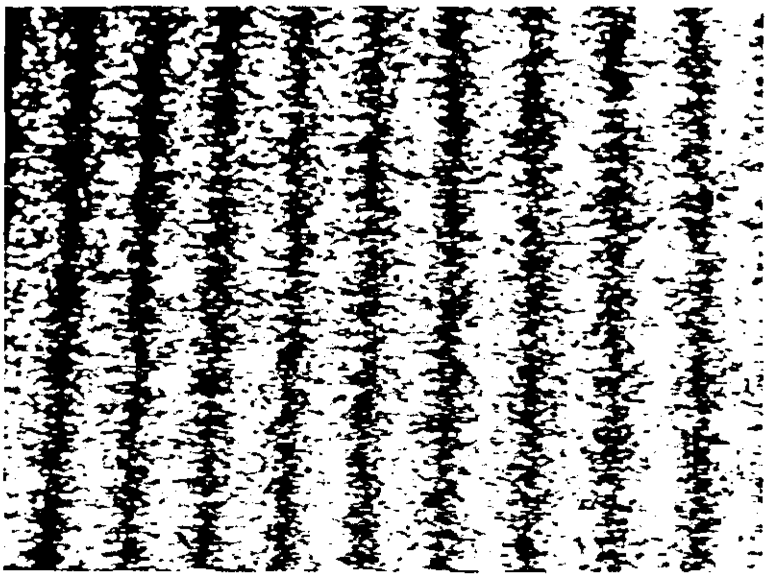

Figure 3.13
Convergent reference beam. V = 0.4750.

3.4.3 Oscillating Speckled Reference Beam.

The experimental procedure to be followed here is that of subsection 3.3.4., though here with reference to figure 3.14 for which the following applies:

- Imaging lens focal length → $f = 200$ mm.
- Aperture Diameter → $a = 20$ mm.
- Object to imaging lens distance → $u = 600$ mm.
- Converging spot diameter (on GG) → $d = 5$ mm.
- Amplitude of mirror drive → $m = 0.1$ V peak to peak.
- ratio of reference to object beam intensities → $r = 2$.
- $l_1 = 50$ mm.
- $l_2 = 210$ mm.

Table VIII shows the results for the present experiment, where the three ground glasses used before are employed again. The columns Mean and S.D. represent measurements over the whole field.

Overall the visibility values found in table VIII are higher (up to 18% in the best case) than those shown in table IV for the case of the beam splitter behind the lens.

Figure 3.15 displays the results for this experiment. The photographs were taken at 140 Hz.

TABLE VIII

Frequency (Hz)	Visibility	Uncertainty x 10^{-2}	Mean	S.D.	GG#
	0.5507	7.41	24.40	17.78	1
0)	0.5342	6.77	36.00	26.66	2
	0.5478	9.68	27.51	20.70	3
	0.4673	8.90	22.80	14.36	1
25)	0.4197	9.04	33.50	18.60	2
	0.4104	9.95	26.75	14.90	3
	0.4506	10.75	25.81	15.85	1
50)	0.4273	7.39	32.14	19.01	2
	0.4490	10.09	28.23	16.84	3
	0.5711	9.67	23.19	17.14	1
140)	0.5740	9.02	24.11	19.23	2
	0.5527	9.74	23.61	18.53	3
	0.5532	10.26	20.53	16.64	1
280)	0.5867	9.80	26.13	20.69	2
	0.5665	9.28	25.04	20.09	3
	0.5235	8.59	27.60	20.63	1
560)	0.4997	9.63	33.86	23.65	2
	0.5822	6.98	29.19	22.41	3
	0.5346	10.10	26.84	20.18	1
1400)	0.5680	7.12	35.26	25.98	2
	0.5619	8.27	28.19	21.30	3
	0.5588	6.59	27.31	21.57	1
2860)	0.5795	9.72	32.35	25.87	2
	0.5826	9.25	27.66	21.30	3
	0.5545	9.80	27.01	20.15	1
4200)	0.5458	8.92	32.91	24.04	2
	0.5133	10.42	27.87	20.39	3
	0.5682	9.06	26.06	19.94	1
6840)	0.5674	9.40	32.55	25.74	2
	0.5413	8.20	31.44	23.19	3
	0.5906	7.92	27.21	20.80	1
12090)	0.5224	11.02	34.83	26.26	2
	0.5627	7.34	28.99	23.08	3
	0.5801	8.84	25.49	19.91	1
15000)	0.5303	10.17	35.64	25.41	2
	0.5695	6.71	27.57	21.60	3
	0.5652	9.63	26.79	20.13	1
16230)	0.5563	9.23	30.50	22.28	2
	0.5553	8.20	29.95	23.01	3
	0.5750	7.44	25.92	22.28	1
19230)	0.5125	8.98	32.90	22.58	2
	0.5560	5.54	30.14	22.94	3

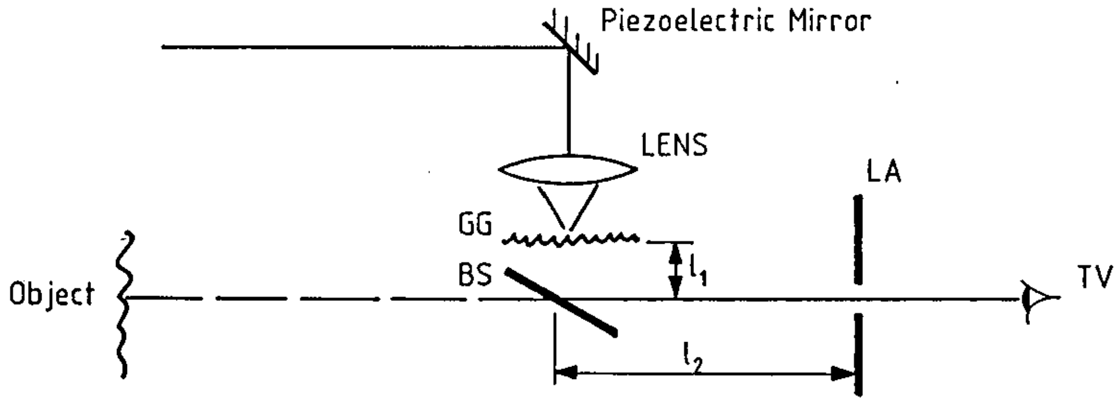

Figure 3.14
Optical set-up for the speckled reference beam. GG is the ground glass, BS the beam splitter, l_1 is the GG to BS distance and l_2 is the BS to imaging lens distance. The lens l is used to converge the beam on the GG.

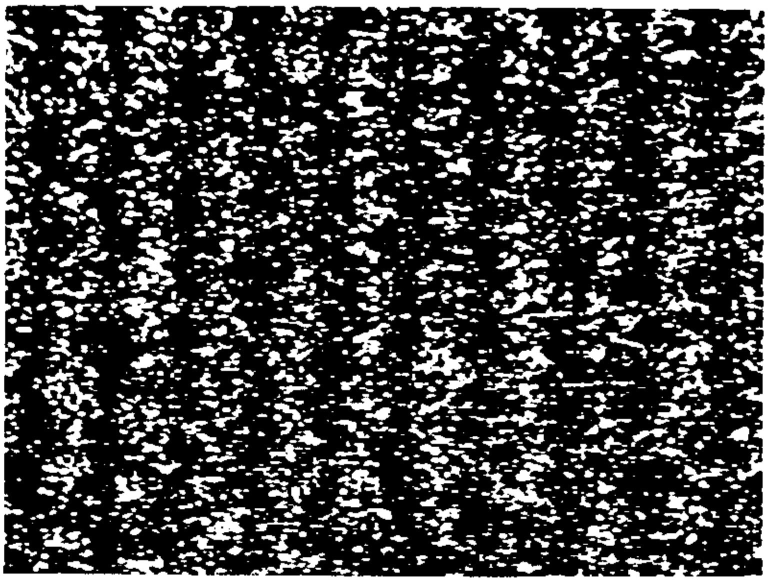

(a)

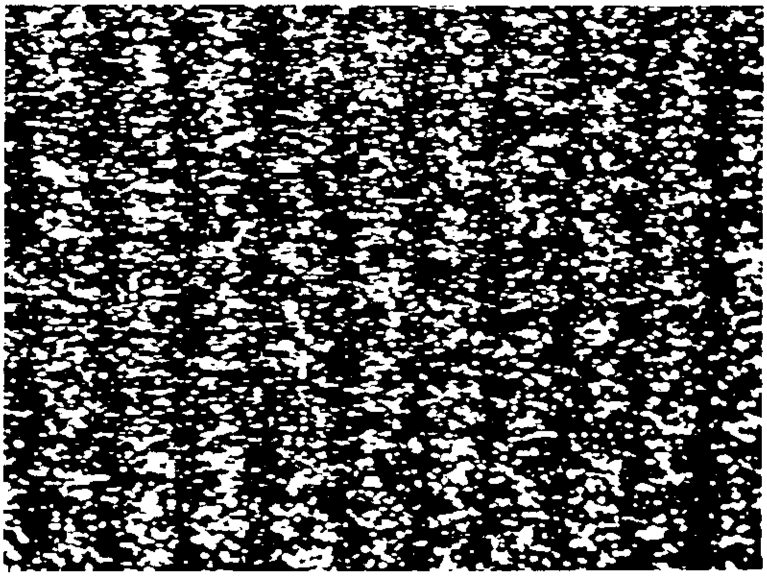

(b)

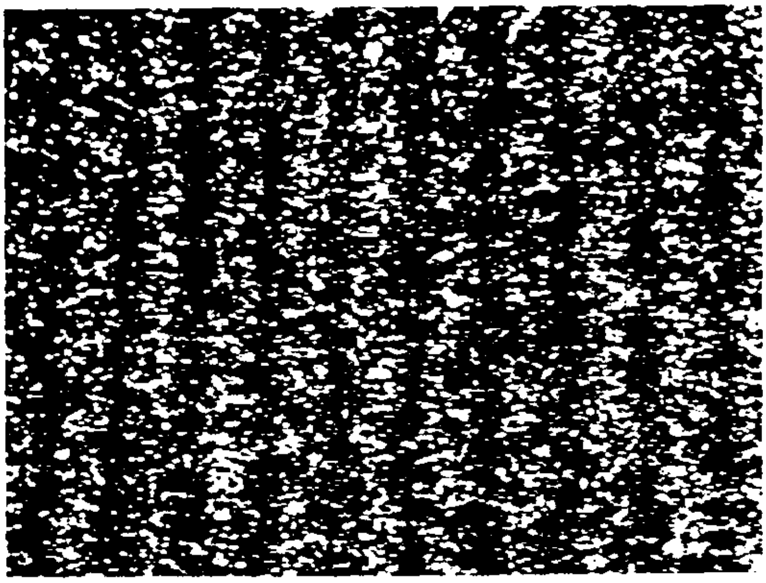

(c)

Figure 3.15

Oscillating speckled reference beam using the beam splitter in between the object and the imaging lens. (a) GG 1, V = 0.5711, (b) GG 2, V = 0.5740 and (c) GG 3, V = 0.5527.

3.4.4 Stepping Speckled Reference Beam.

The experiment in this part uses the same procedure as that of 3.3.5, but now it refers to figure 3.16. Table IX contains the results for this case.

Due to the nature of the experiment (the fringe patterns shifted their relative positions, even though the number of fringes remained the same) the integration routine did not prove successful and the values found for a single pattern are better than those for eight.

TABLE IX

Ground Glass	1	2	3
Visibility (1)	0.3915	0.3954	0.3977
Uncertainty x 10^{-2}	11.44	8.05	9.02
Mean	25.48	24.02	27.81
S.D.	15.22	14.89	16.36
Visibility (8)	0.1751	0.1912	0.2112
Uncertainty x 10^{-2}	5.39	6.93	6.87
Mean	25.91	24.11	25.63
S.D.	7.20	7.33	8.90

The photographs for this experiment are contained in figure 3.17.

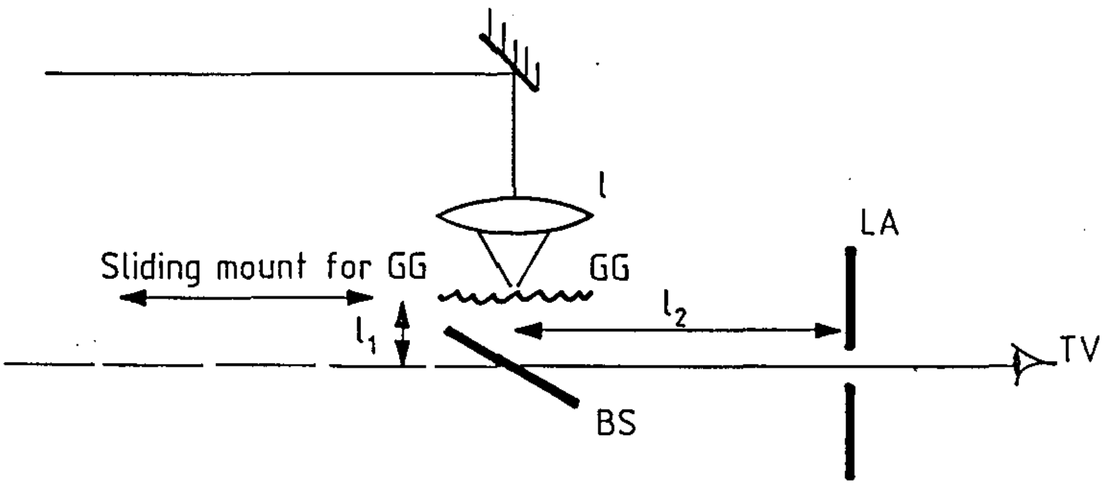

Figure 3.16
Lay-out for the translating ground glass (GG).
The terminology is the same as that in fig.3.7

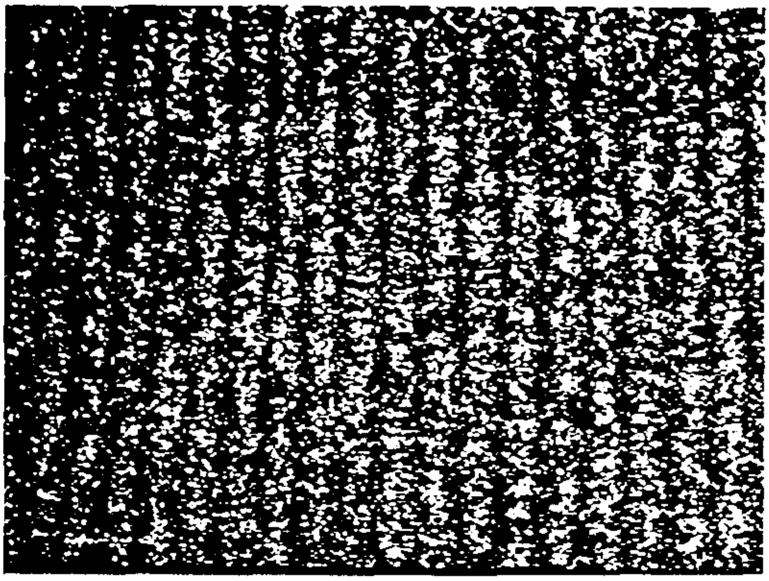

(a)
Single pattern

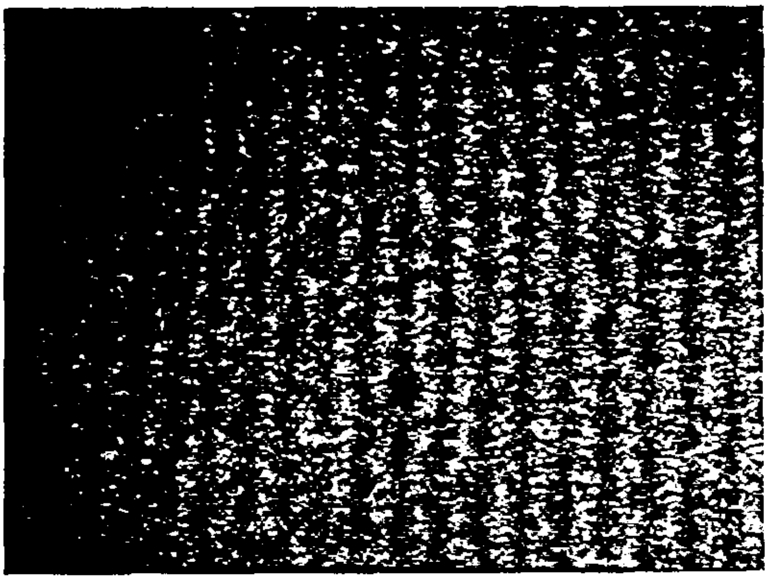

(b)
Average of 8 patterns.
Ground Glass 1. Visibilities as in Table IX.

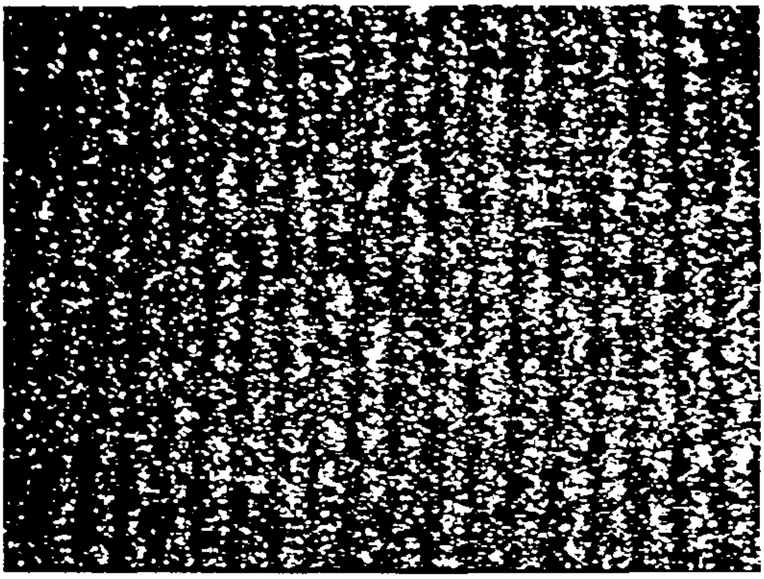

(c)
Single pattern

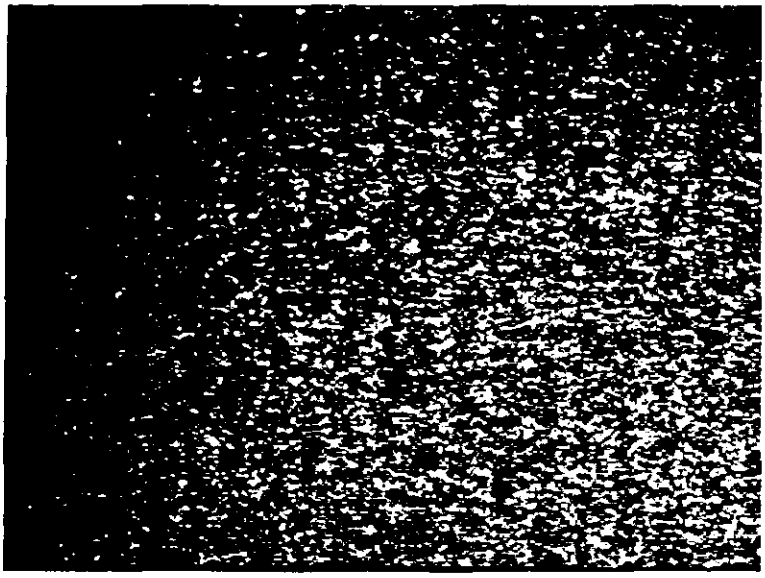

(d)
Average of 8 patterns.
Ground Glass 2. Visibilities as in Table IX.

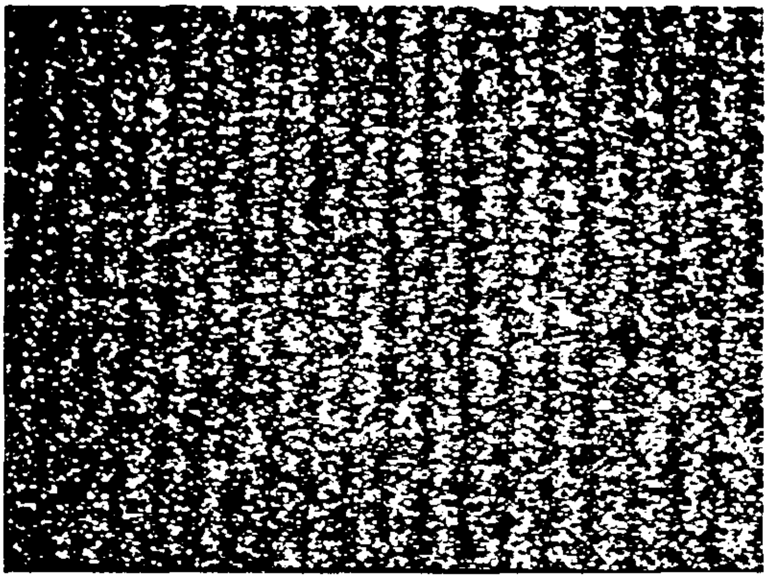

(e)
Single pattern

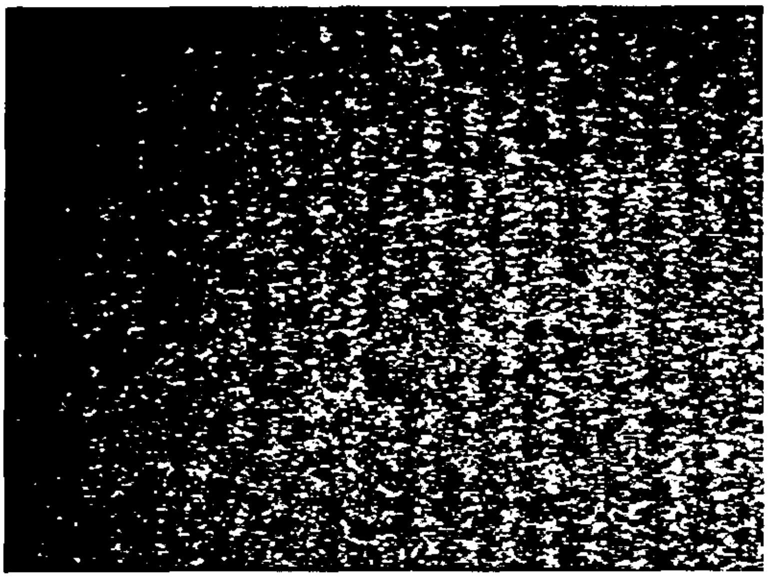

(f)
Average of 8 patterns.
Ground Glass 3. Visibilities as in Table IX.
Figure 3.17

3.5 Discussion.

Figures 3.18 and 3.19 are plots showing the visibility values obtained in tables I and II for the divergent and convergent beams, for two beam ratios (r = 8, 2), with lines of regression. Both graphs show the data fitting well inside the uncertainty bands for the visibility calculations. The visibility is seen to be higher for r = 2. It can be noticed from these plots the trend the data follows, i.e. the visibility increases for decreasing wavefront curvatures (divergent beam), and increases as the convergent curvature increases. From these results, a slightly converging reference beam with a large radius of curvature will be the optimum. The results for the parallel reference beam displayed in figure 3.20 (from table III) verify this. The plot shows a decrease in visibility with beam ratio.

The results above showed that the best visibility values are expected when r = 2, thus all the experiments that followed were carried out using this ratio.

Figures 3.21 and 3.22 exhibit the visibility obtained for the divergent and convergent reference beams corresponding to the case where the beam splitter is located in between the object and imaging lens (section 3.4, tables VI and VII). Again the regression lines fit well with the uncertainty values estimated. For the divergent beam the data shows a steady decrease in visibility with increasing radius of curvature (the minimum value seen there is for the case of the parallel reference beam), while for the convergent beam the slope of the regression line is nearly zero. The average value for the visibility is slightly higher for the converging reference beam, thus a convergent beam with weak curvature proves the best.

On comparing figs. 3.18 and 3.19 with 3.21 and 3.22, it is seen that the ESPI system has a very similar response for the cases treated in sections 3.3 and 3.4, namely beam splitter behind and in front the imaging lens. However, the average visibility values are higher for the later case by ABOUT 10% . This, together with the fact that for figs. 3.21 and 3.22 the f/# used was 10 as compared to that of f/# = 25 for plots 3.18 and 3.19, makes the optimum position for the beam splitter to be between the imaging lens and the object.

Figures 3.23 to 3.25 correspond to the oscillating speckled reference beam. They include the cases for the beam splitter in front and behind the imaging lens. The data is dealt with a linear regression showing a steady positive trend for both cases, i.e. the visibility increases as a function of the frequency with which the reference beam is driven. The averages of the visibility values obtained from table VIII (bottom of figs. 3.23 to 3.25), associated to the beam splitter in front of the lens are the highest from all the results available.

The integration routine applied to the case of the stepping speckled reference beam fails to give improved visibility values, mainly due to the fact that the ESPI electronic system lacks an appropriate locking device for the incoming signal (the fringes shifted due to air currents, etc.). It was expected that, since the density of correlation fringes was kept constant, the integration routine would have given less noisy, better visibility fringes. A comparison between tables V and IX is, however, possible, e.g. the visibility (for 8 images) values for the case where the beam splitter lies in between the object and the imaging lens are higher for ground glasses 2 and 3.

3.6 Closure.

The results presented here show that a wide range of reference beam geometries can be used in ESPI, making of the conjugacy requirement a clumsy and unnecessary design feature. This statement is supported by the fact that the beam splitter can be used in between the object and the imaging lens. Furthermore, ESPI working in this mode uses a smaller f/# (10 in this case, but results are believed to prove succesful if a smaller f/# is used) meaning that smaller (than 10 mW) laser powers are required. The earlier design of ESPI introduced astigmatism due to the beam splitter: this is now avoided by using the beam splitter in front of the imaging lens. In doing this the imaging lens can now be directly attached to the TV camera.

For the case of the beam splitter located in the usual configuration it is found that a slightly converging reference beam gives the best overall results for the visibility. This result is found to be the same for the beam splitter in between the object and imaging lens: the visibility values are higher in this case.

The ESPI system proved its best performance when using a speckled reference beam coming from a ground glass in the object space, i.e. the beam splitter in between the object and viewing lens.

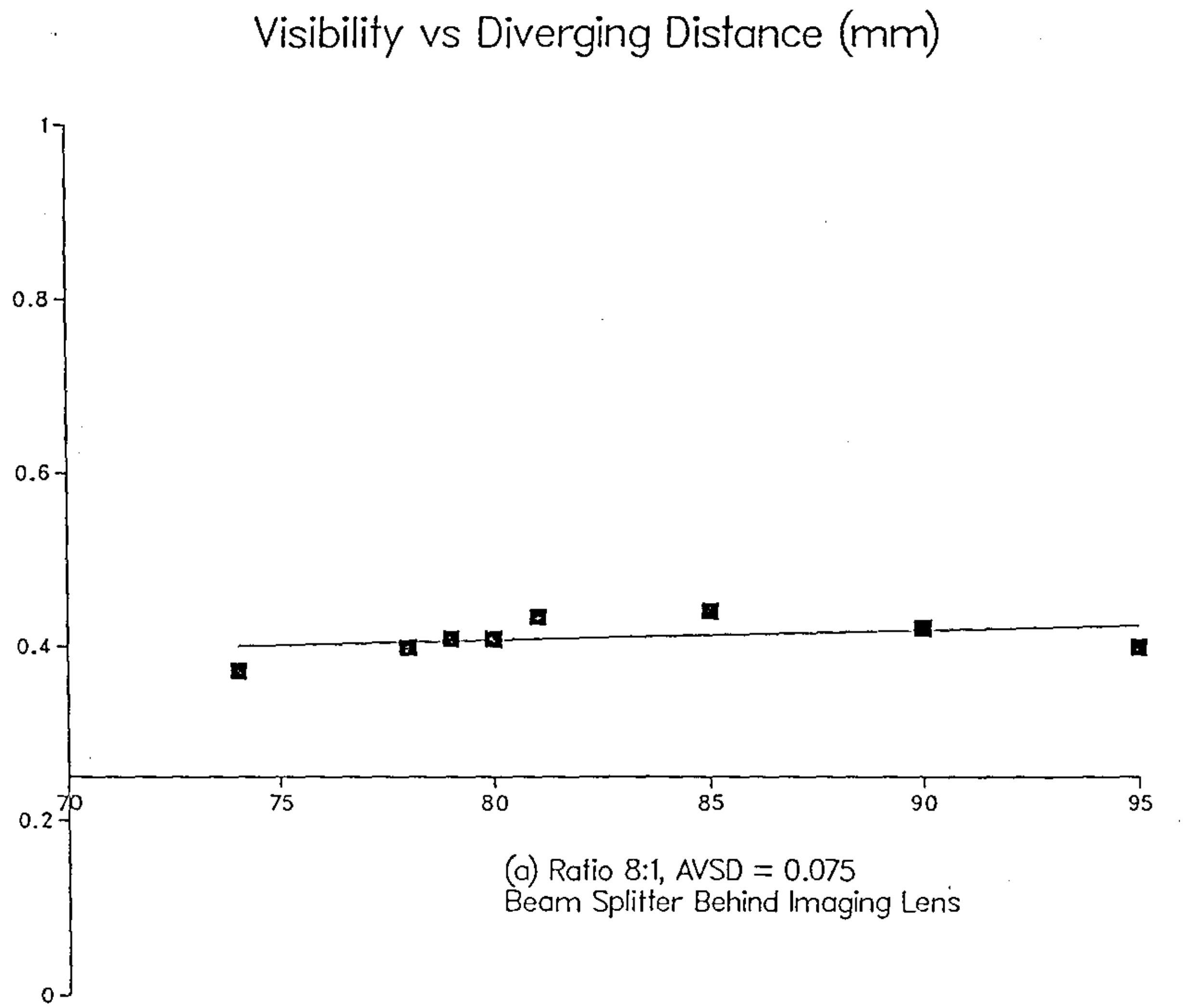
Visibility vs Diverging Distance (mm)
1
0.8
0.6
0.4
0.2
0
70
75
80
85
90
95
(a) Ratio 8:1, AVSD = 0.075
Beam Splitter Behind Imaging Lens

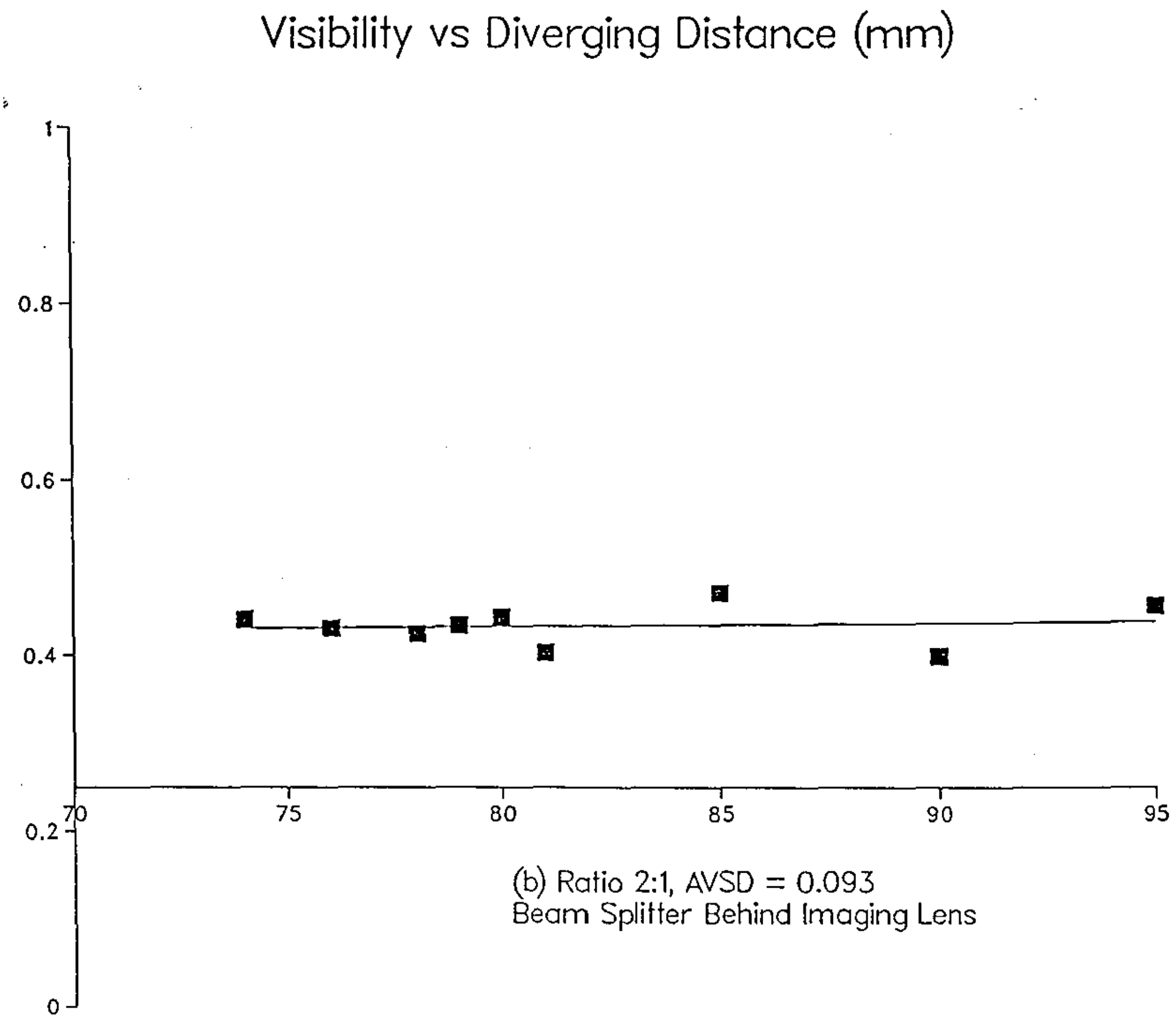

Visibility vs Diverging Distance (mm)
1
0.8
0.6
0.4
0.2
0
70
75
80
85
90
95
(b) Ratio 2:1, AVSD = 0.093
Beam Splitter Behind Imaging Lens

Figure 3.18

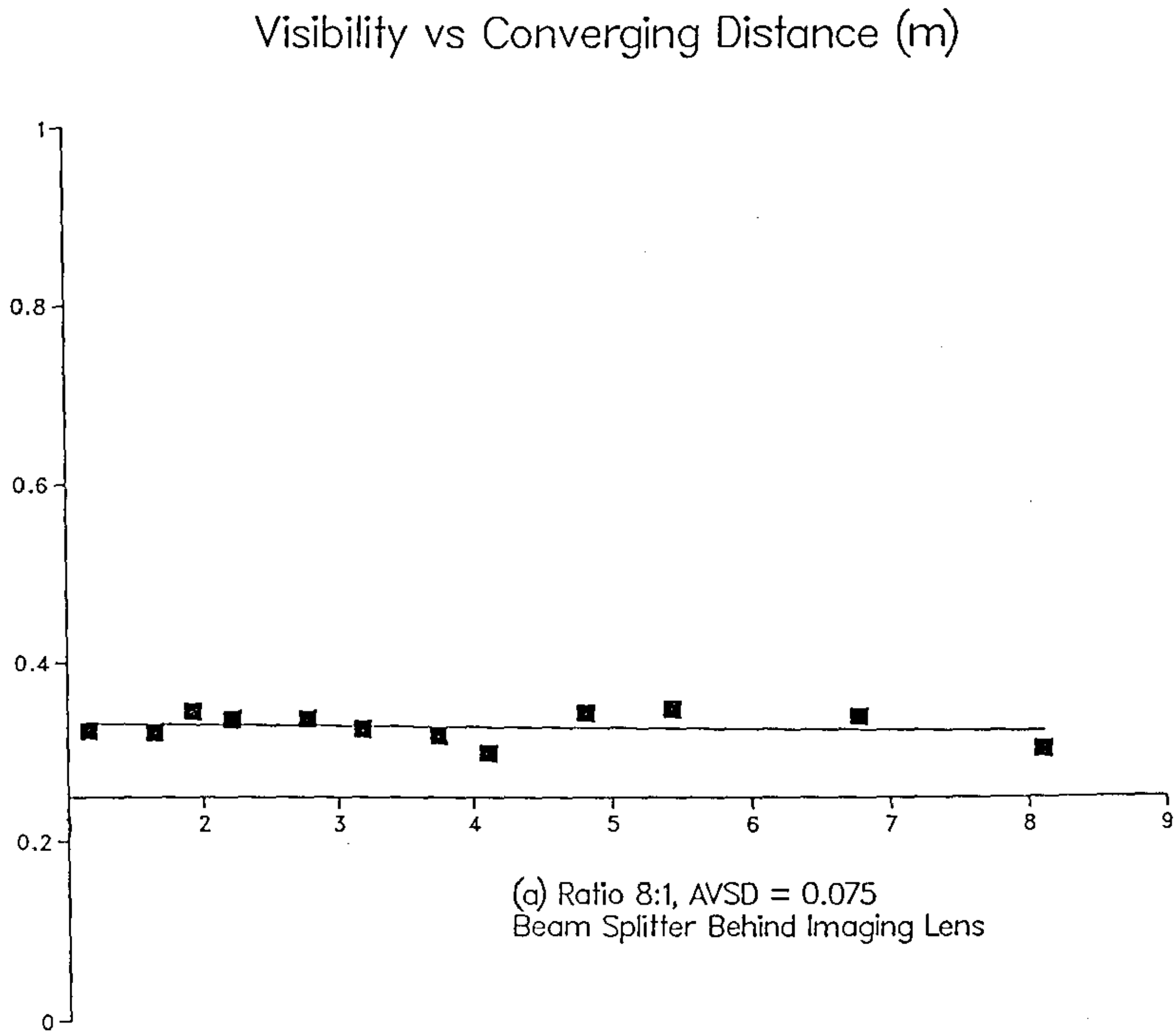

Visibility vs Converging Distance (m)
1
0.8
0.6
0.4
0.2
0
2
3
4
5
6
7
8
9
(a) Ratio 8:1, AVSD = 0.075
Beam Splitter Behind Imaging Lens

Visibility vs Converging Distance (m)

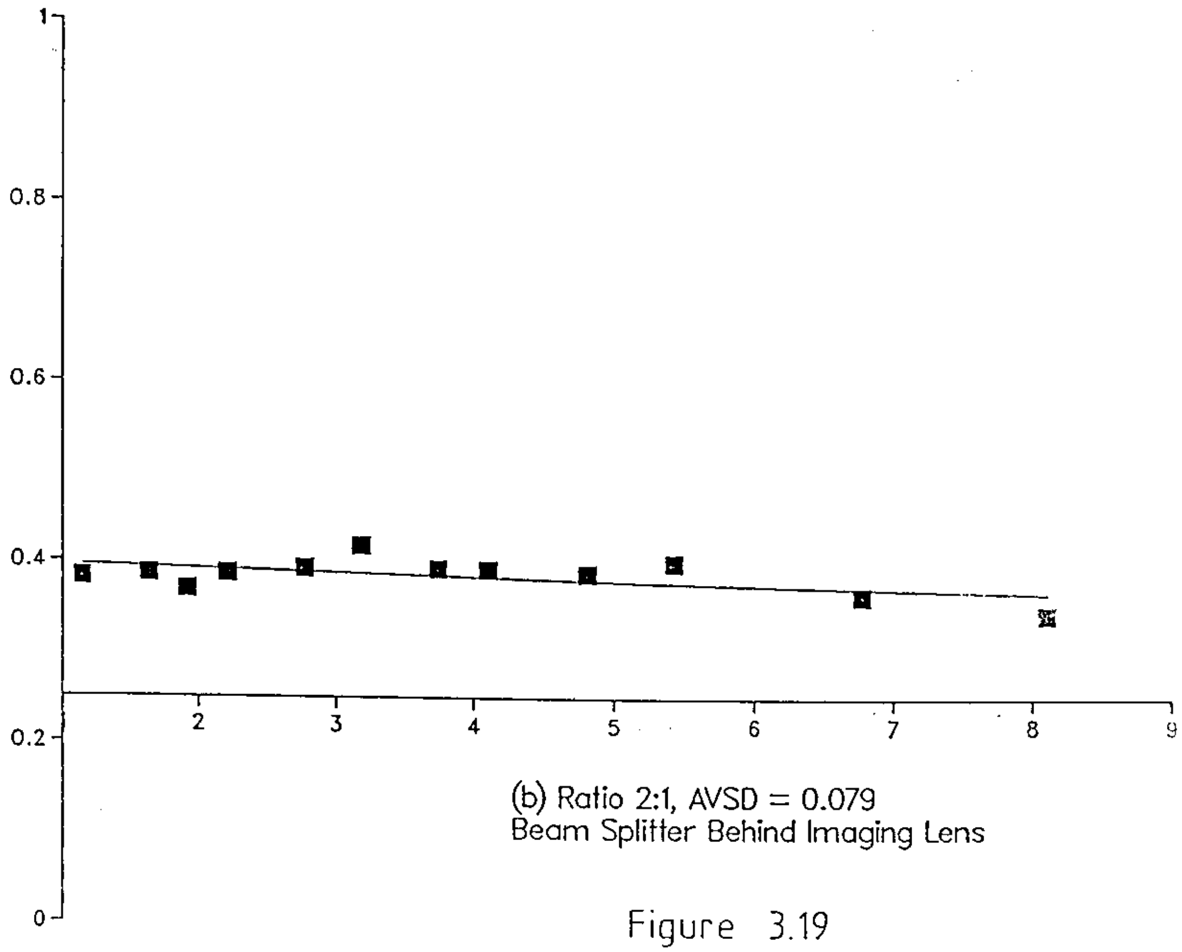

(b) Ratio 2:1, AVSD = 0.079
Beam Splitter Behind Imaging Lens

Figure 3.19

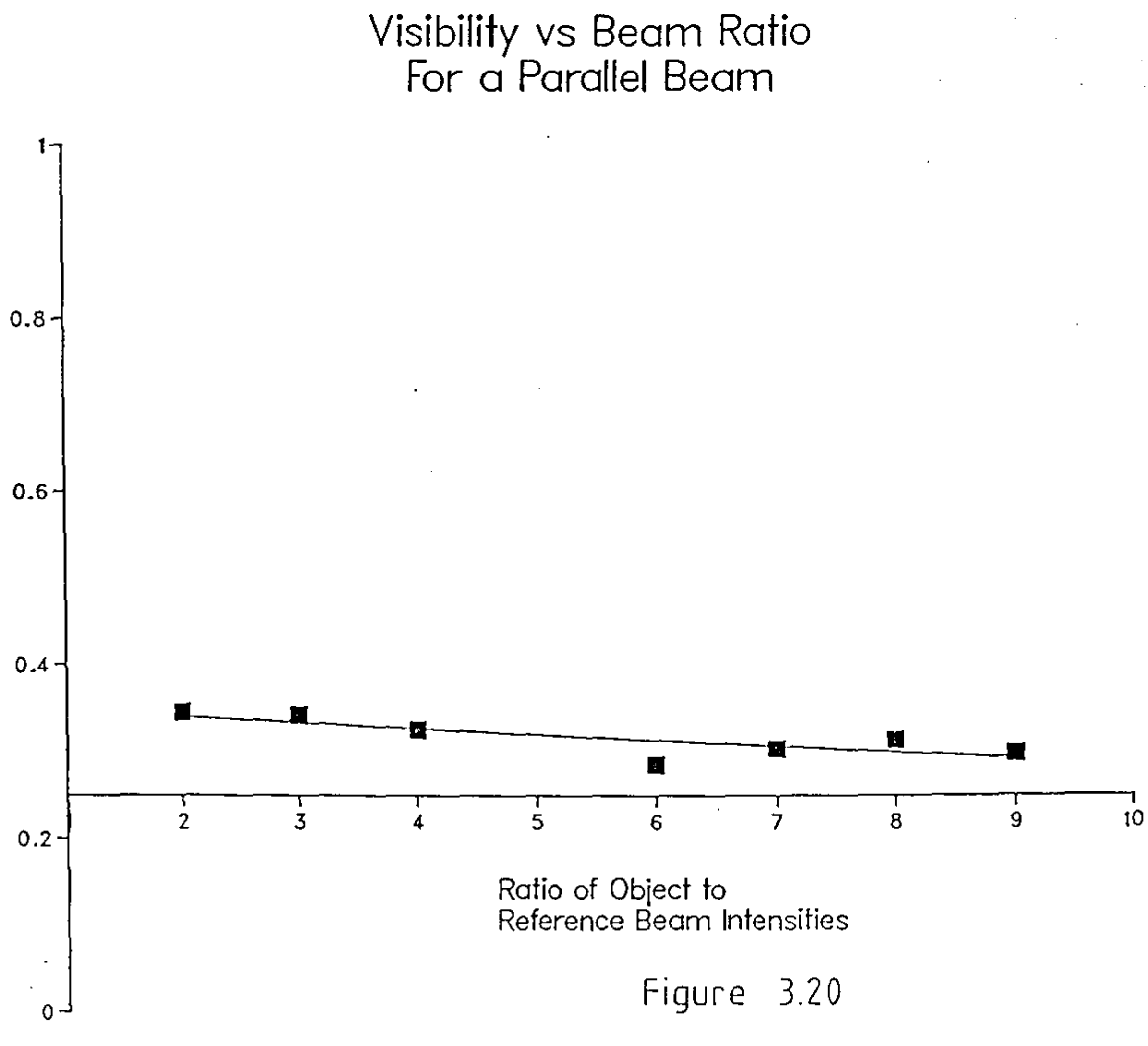

Visibility vs Beam Ratio
For a Parallel Beam
1
0.8
0.6
0.4
0.2
0
2
3
4
5
6
7
8
9
10
Ratio of Object to
Reference Beam Intensities

Figure 3.20

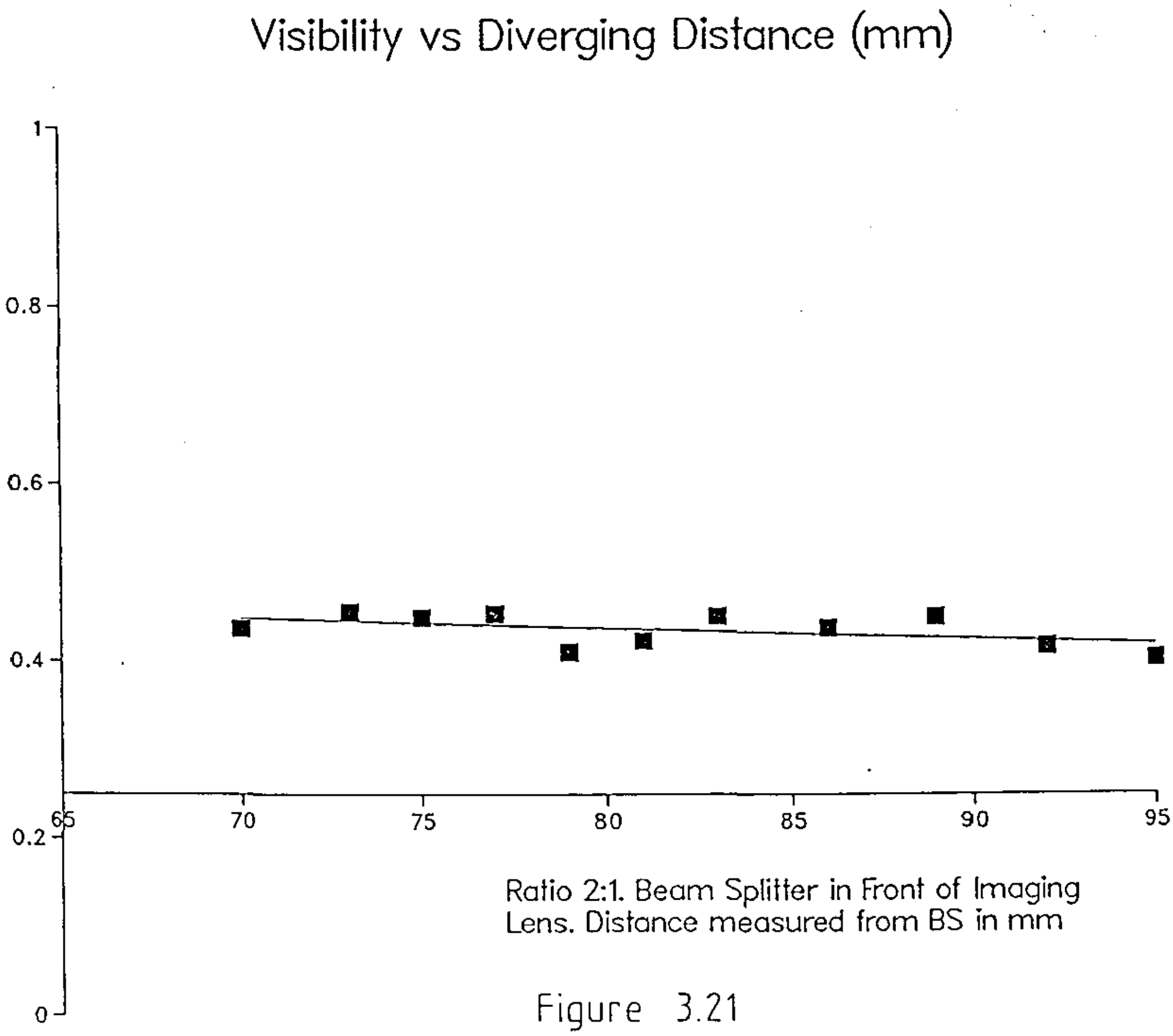

Visibility vs Diverging Distance (mm)
1
0.8
0.6
0.4
0.2
0
65
70
75
80
85
90
95
Ratio 2:1. Beam Splitter in Front of Imaging
Lens. Distance measured from BS in mm

Figure 3.21

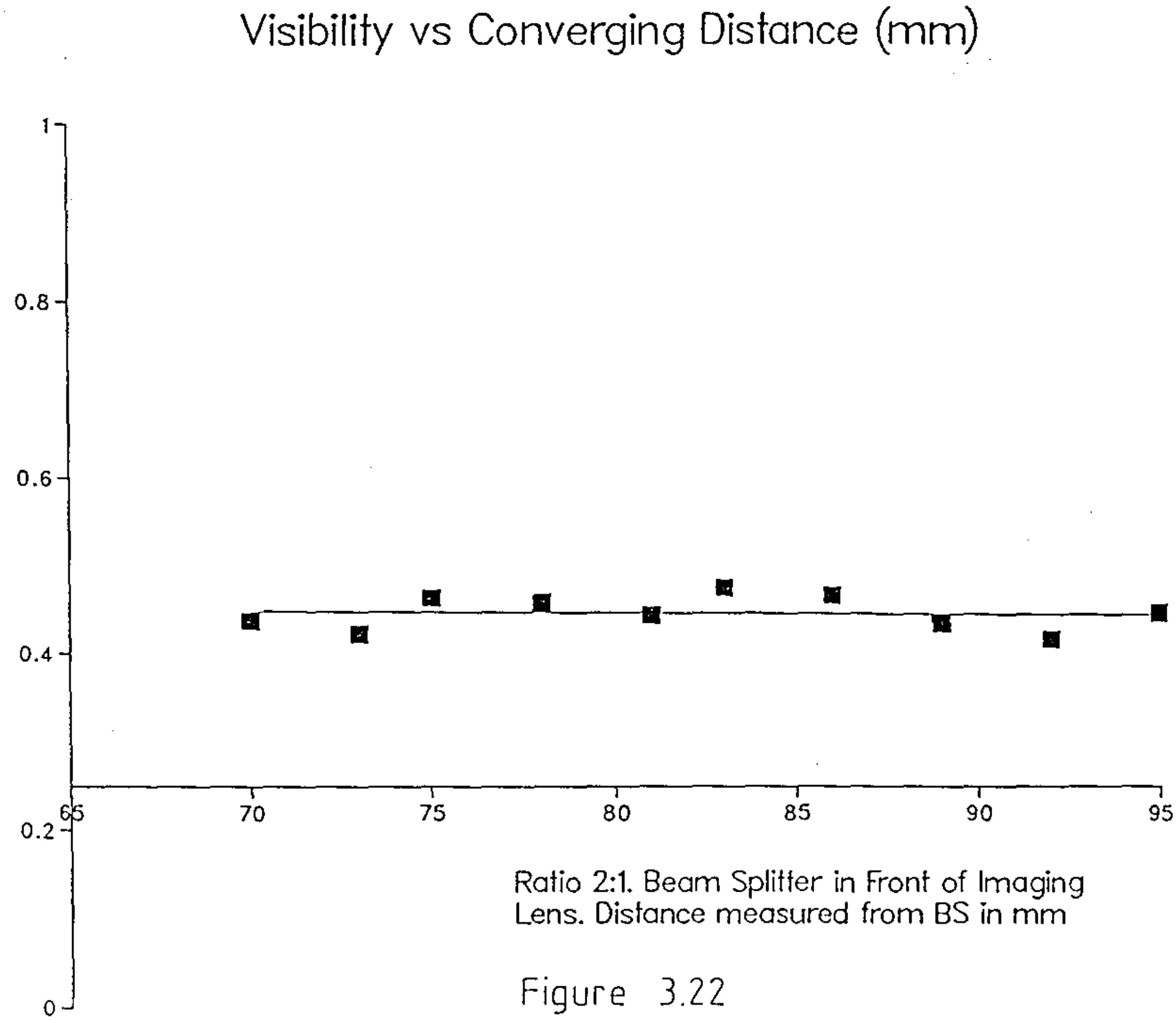

Ratio 2:1. Beam Splitter in Front of Imaging Lens. Distance measured from BS in mm

Figure 3.22

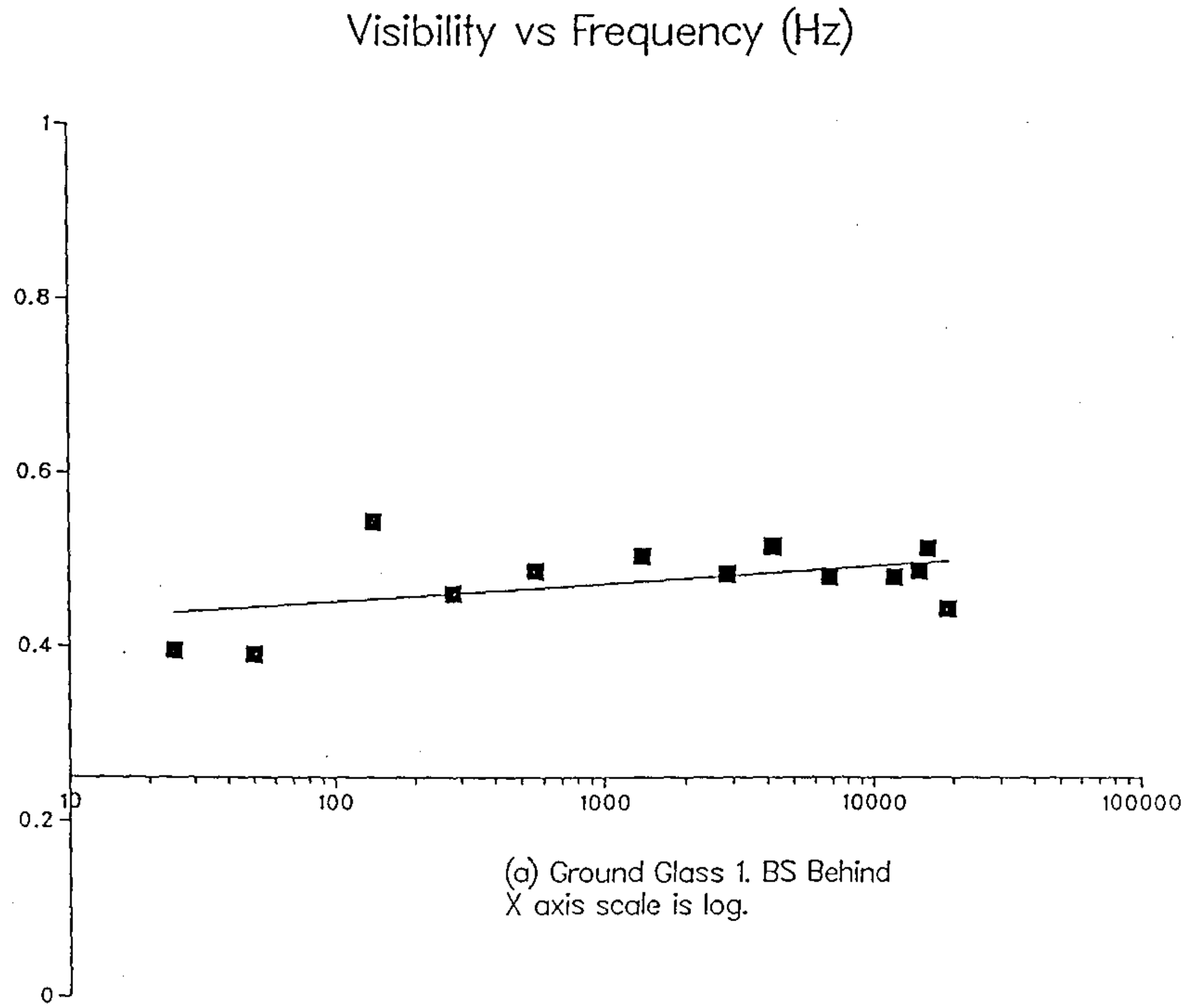

(a) Ground Glass 1. BS Behind
X axis scale is log.

Visibility vs Frequency (Hz)

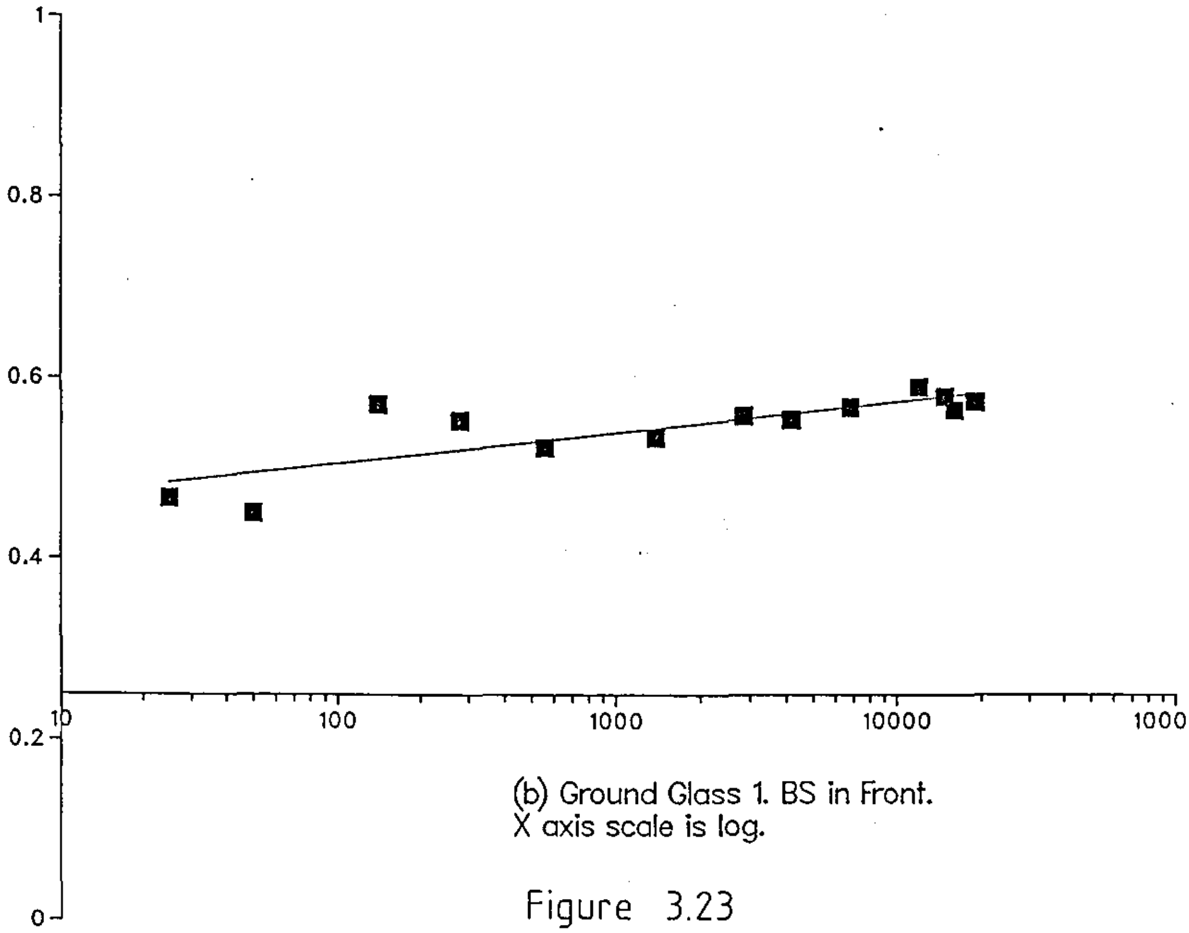

(b) Ground Glass 1. BS in Front.
X axis scale is log.

Figure 3.23

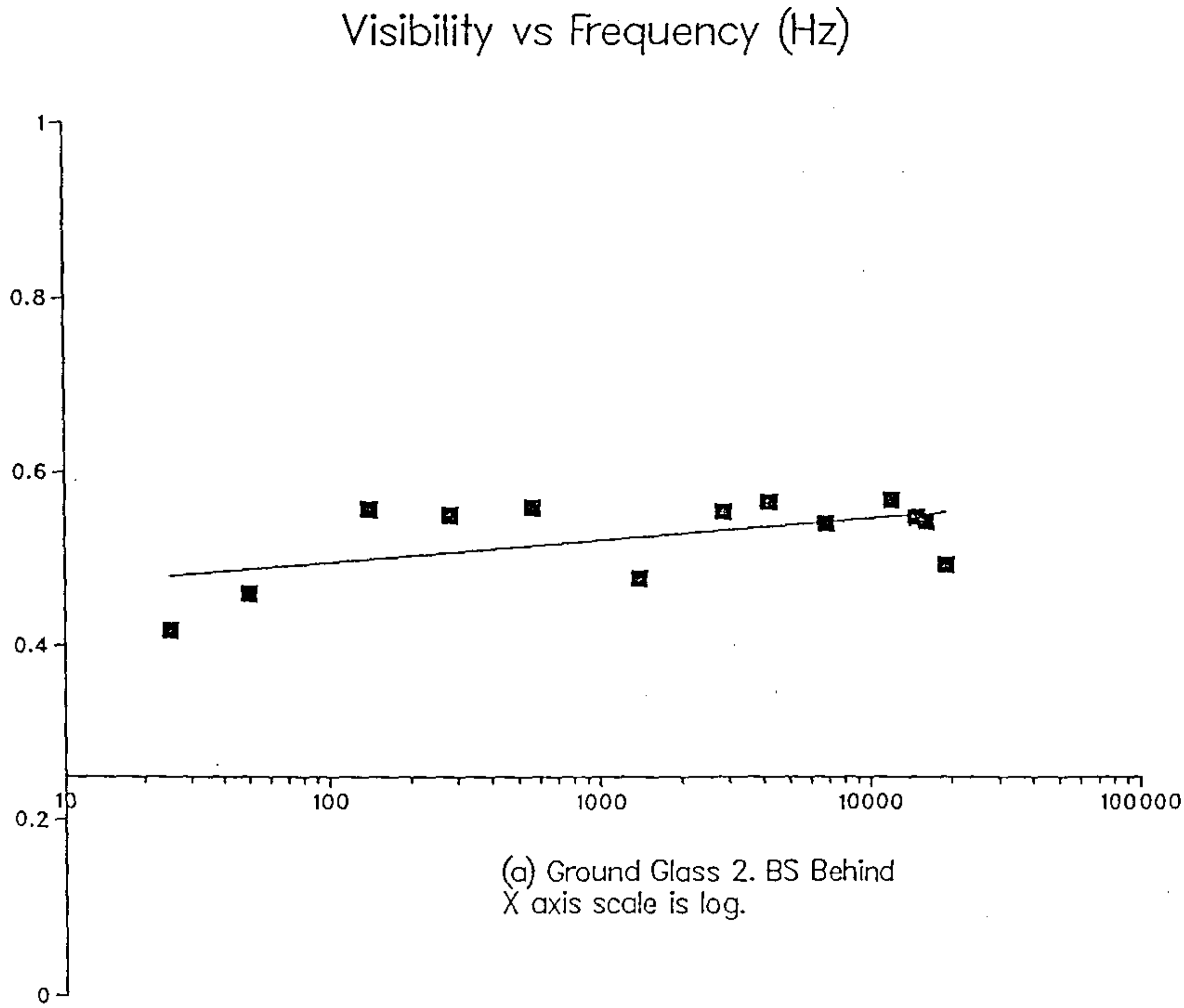

(a) Ground Glass 2. BS Behind
X axis scale is log.

Visibility vs Frequency (Hz)

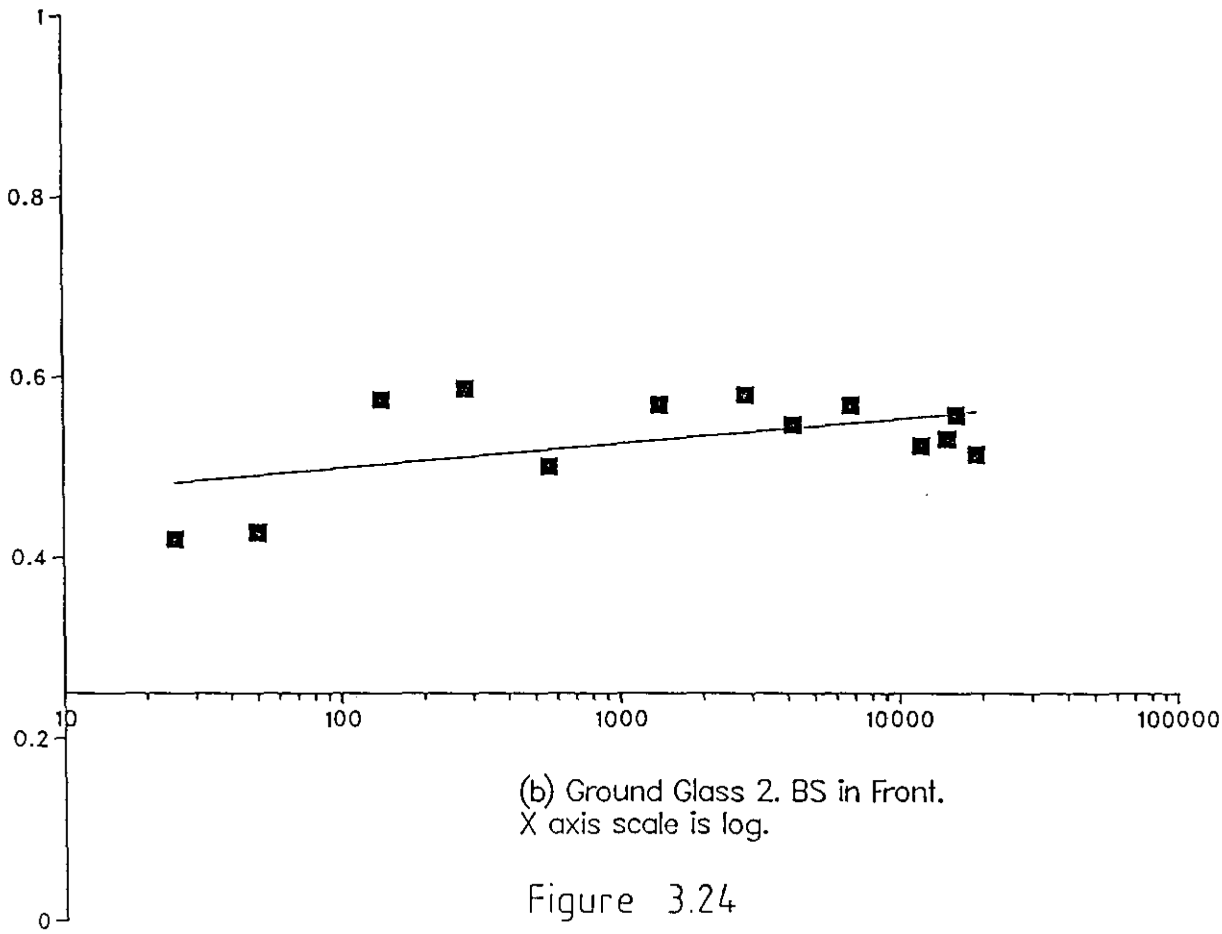

(b) Ground Glass 2. BS in Front.
X axis scale is log.

Figure 3.24

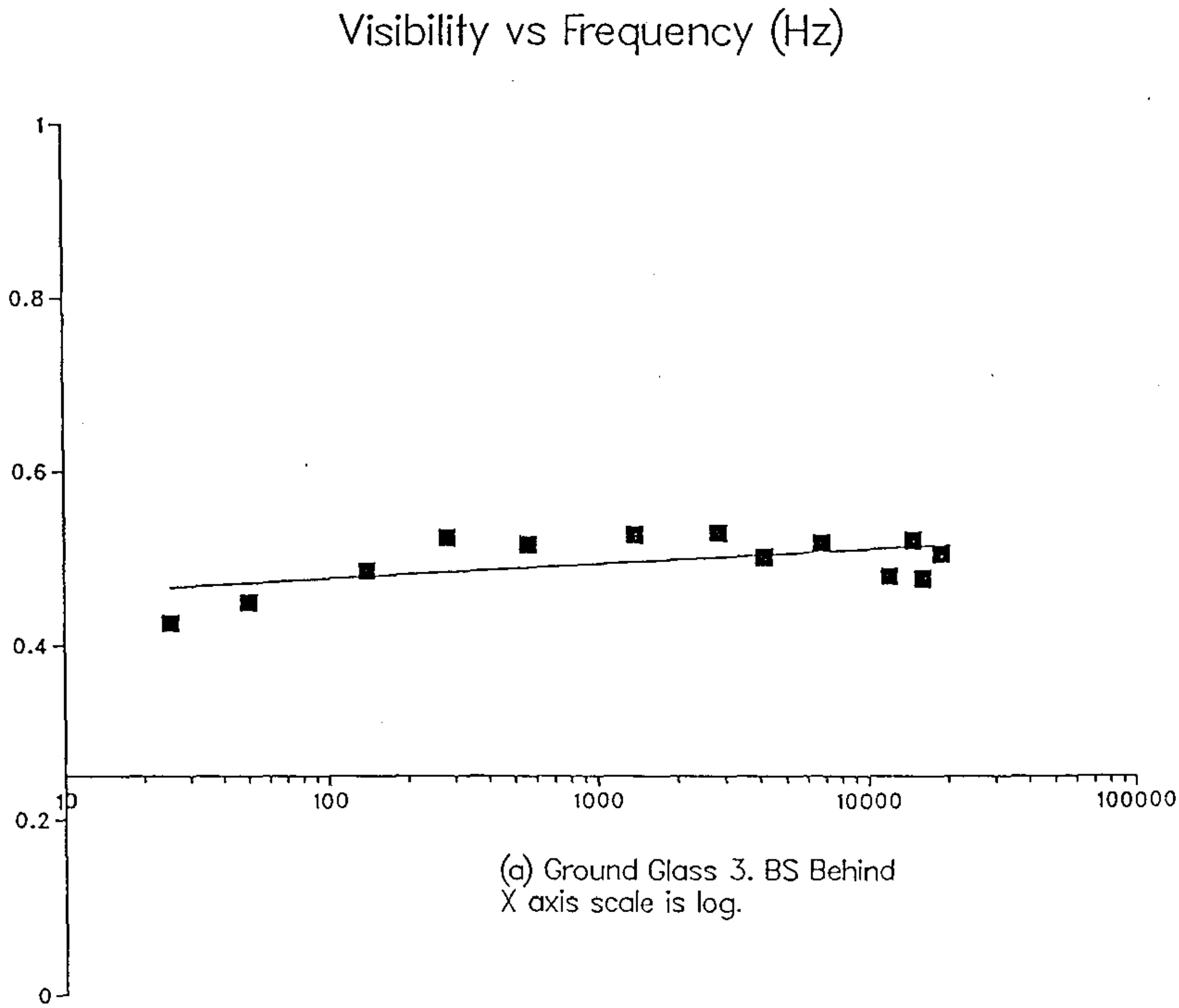

(a) Ground Glass 3. BS Behind
X axis scale is log.

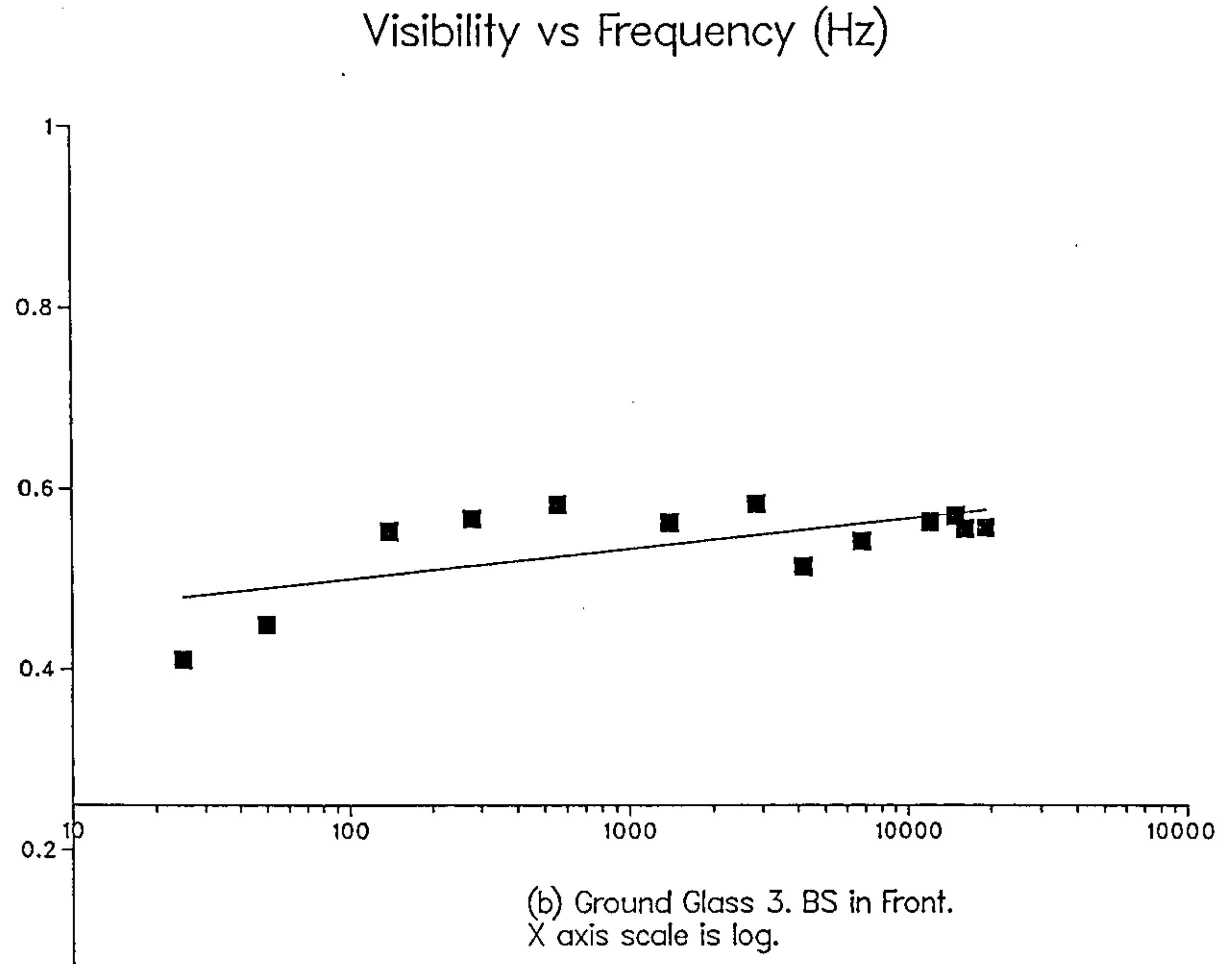
Visibility vs Frequency (Hz)
1
0.8
0.6
0.4
0.2
0
10
100
1000
10000
10000
(b) Ground Glass 3. BS in Front.
X axis scale is log.

Figure 3.25

CHAPTER IV
SPATIAL FREQUENCY RESPONSE

4.1 Introduction.

To establish the response characteristics of the electronic apparatus in an ESPI system experimentally, a straight line fringe pattern was created at the plane of the TV camera photosurface. This fringe pattern was stored in the system memory and a subsequent straight line fringe pattern was subtracted from it. The results obtained were used to examine the response of the ESPI electronic system. Smooth wavefronts were used throughout.

A theoretical treatment of an equivalent procedure will be given in Chapter V.

4.2 Use of Mach-Zehnder Interferometer.

A Mach-Zehnder interferometer was employed (because of two available fringe fields) to create the straight line fringes used to find the response characteristics of the electronic system in ESPI. The interferometer is illustrated in figure 4.1.

A well collimated beam of monochromatic light was required to create parallel (vertical with respect to the horizontal scanning of the photosurface) fringes of equal spacing at either end of the interferometer arms. Tilting one of the mirrors will vary the spacing of the fringes, thus having a range of spatial frequencies available.

Figure 4.1 shows in one of the instrument's arms the TV camera photosurface being directly exposed to the incoming fringes, and in the other a magnifying lens that is used to help counting the fringes to ensure the right number of fringes/mm are present at the plane of the TV photosurface.

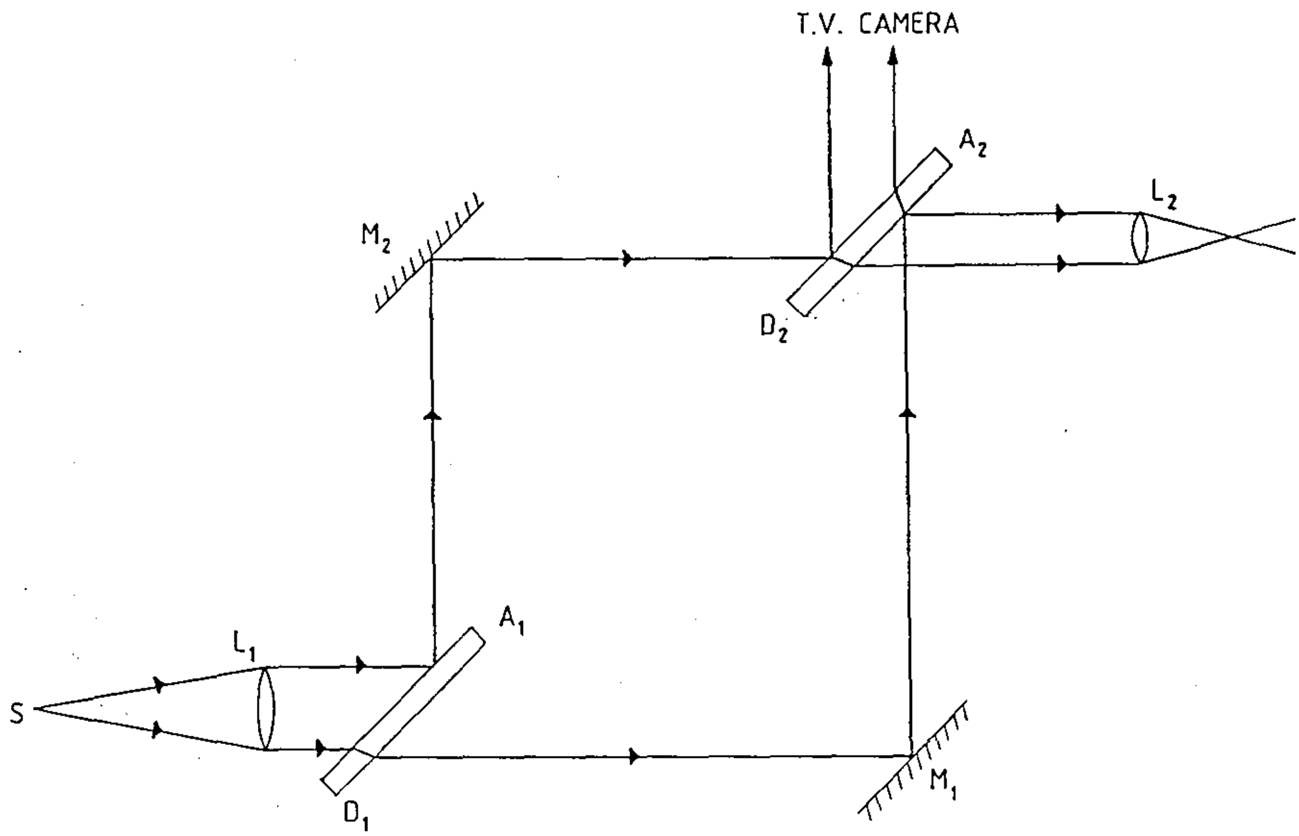

Figure 4.1
Mach-Zehnder interferometer. The four reflecting surfaces were approximately parallel, with their centers at the corners of a parallelogram. S → Source; L_1, L_2 → Corrected lenses; A_1, A_2 → Semireflecting surfaces; D_1, D_2 → identical plane parallel plates and M_1, M_2 → plane mirrors.

4.3 Experimental Technique.

The TV camera photosurface had the following characteristics:

1) Active horizontal length of 12 mm ± 0.25.

2) Horizontal scan rate: 52 μs. (This figure did not consider recuperation, porch and flyover times).

3) 5 MHz bandwidth.

4) ⇒ Horizontal pixel size of: 23.08 μm.

5) Vertical pixel size (set by line spacing) of: 15.6 μm.

To assess the spatial response of the TV system, the following procedure was followed:

a) Store a first set S1 of n1 fringes/mm in the memory.

b) Next produce a second set S2 of n2 fringes/mm to be subtracted from the first S1 set. A number n of subtraction fringes were obtained and stored.

c) Repeat the above steps by changing the spatial frequency of the first and second sets of fringes in such a way as to obtain always the same number of n subtraction fringes.

The method described gave as result a series of subtraction patterns whose visibility values were calculated from:

$$V = (I_{max} - I_{min}) / (I_{max} + I_{min}) \qquad (1)$$

Each of these subtraction patterns was analysed by a computer that carried out readings of intensity values along different horizontal lines, finding all the maximum and minimum values for every fringe that was encountered over the particular inspected line. These values were subsequently averaged and a figure was calculated for the visibility of the entire pattern. Once the visibility for all the subtraction patterns was obtained, a comparison among them was possible.

4.4 Results and Discussion.

Table I shows some typical results obtained for the subtraction patterns. It gives, in the first column, the number n1 of fringes/mm used as the S1 set, and in the second column the number n2 of fringes/mm needed to get n = 24 subtraction fringes across the monitor or 2 fringes/mm (this figure was chosen for visual simplicity). The last column displays the values for the visibility, eq.(1), of the pattern.

The experimental uncertainties found relate primarily to measurements done while counting the fringes, i.e. a lens was used to project the fringes on a screen (thus facilitating their counting) so that the lens focal length and the distance from this to the screen were taken into consideration for the uncertainty values. Therefore 24 fringes across the field $\rightarrow$ 2 fringes/mm $\pm$ 0.5. Table I shows this for the first row, but it applies to all the results.

TABLE I

Fringes/mm (S1)	Fringes/mm (S2)	Visibility
90 ± 0.5	22 ± 0.5	0.0886
80	22	0.1020
75	22	0.0963
68	22	0.0806
60	22	0.1153
52	22	0.0825
46	21	0.1215
38	21	0.1104
32	29	0.1120
25	23	0.3478
23	19	0.2140
19	16	0.3213
16	14	0.3707*
14	11	0.2588*
11	14	0.3943*
6	9	0.2404*
3	21	0.1604

These results were plotted in figure 4.2, which shows a characteristic response of the electronic system to a square wave signal represented by the vertical fringes, i.e. the successive peaking along the frequency axis. This event will be accounted for next.

The horizontal pixel size was found to be 23 μm, which meant that the maximum number of resolvable fringes the electronic system can perceive in that direction was 22 fringes/mm (i.e. 22 bright fringes/mm or 44 bright and dark fringes/mm). However, the electronic system will not be able to resolve fringes at above approximately 14 to 16 fringes/mm. This problem of resolution together with the fact that the system did not lock the phase of the incoming signal brought as a result the well known phenomenon of aliasing, which was reflected in fig. 4.2 as harmonics and sub-harmonics of the TV scanning rate. In fact all the results of subtraction in table I except those marked with an asterisc were spurious.

Figures 4.3 to 4.11 are photographs (all taken from the monitor, showing a scratch caused by the beam splitter, on the bottom left) depicting this phenomenon. Fig. 4.3 was for n1 = 16 fringes/mm, i.e. a fringe width of 31 μm. The lack of a phase lock together with a slight inclination of the incoming fringes gave the picture an aliasing shape. This is also noted in figs. 4.6 (8 fringes/mm), 4.7 (10 fringes/mm), 4.9 (12 fringes/mm) and 4.10 (17 fringes/mm).

Fig. 4.4 was the result of subtracting 16 with 19 fringes/mm to get 31 subtraction fringes across the field. Notice the similarity with a Moire pattern in this image and in figs. 4.8 (10 - 12 fringes/mm) and 4.11 (17 - 20 fringes/mm).

Fig. 4.5 shows the monitor image for 19 fringes/mm, i.e a fringe width of 26 μm.

The irregularities shown in Table I, with specific reference to the number of fringes being subtracted each time, reflect the inability of the system to resolve beyond 15-16 fringes/mm. This could only mean that, particularly for high spatial frequencies, the electronic apparatus in ESPI carries out an average of intensity per pixel. The higher the spatial frequency of the fringes the noiser the resulting subtraction picture will be. The disparity (exacerbated with the lack of a phase locker) in the visibility values found was also a consequence of this.

reflected in fig. 4.2 as harmonics and sub-harmonics of the TV scanning rate. In fact all the results of subtraction in table I except those marked with an asterisc were spurious.

Figures 4.3 to 4.11 are photographs (all taken from the monitor, showing a scratch caused by the beam splitter, on the bottom left) depicting this phenomenon. Fig. 4.3 was for n1 = 16 fringes/mm, i.e. a fringe width of 31 μm. The lack of a phase lock together with a slight inclination of the incoming fringes gave the picture an aliasing shape. This is also noted in figs. 4.6 (8 fringes/mm), 4.7 (10 fringes/mm), 4.9 (12 fringes/mm) and 4.10 (17 fringes/mm).

Fig. 4.4 was the result of subtracting 16 with 19 fringes/mm to get 31 subtraction fringes across the field. Notice the similarity with a Moire pattern in this image and in figs. 4.8 (10 - 12 fringes/mm) and 4.11 (17 - 20 fringes/mm).

Fig. 4.5 shows the monitor image for 19 fringes/mm, i.e a fringe width of 26 μm.

The irregularities shown in Table I, with specific reference to the number of fringes being subtracted each time, reflect the inability of the system to resolve beyond 15-16 fringes/mm. This could only mean that, particularly for high spatial frequencies, the electronic apparatus in ESPI carries out an average of intensity per pixel. The higher the spatial frequency of the fringes the noiser the resulting subtraction picture will be. The disparity (exacerbated with the lack of a phase locker) in the visibility values found was also a consequence of this.

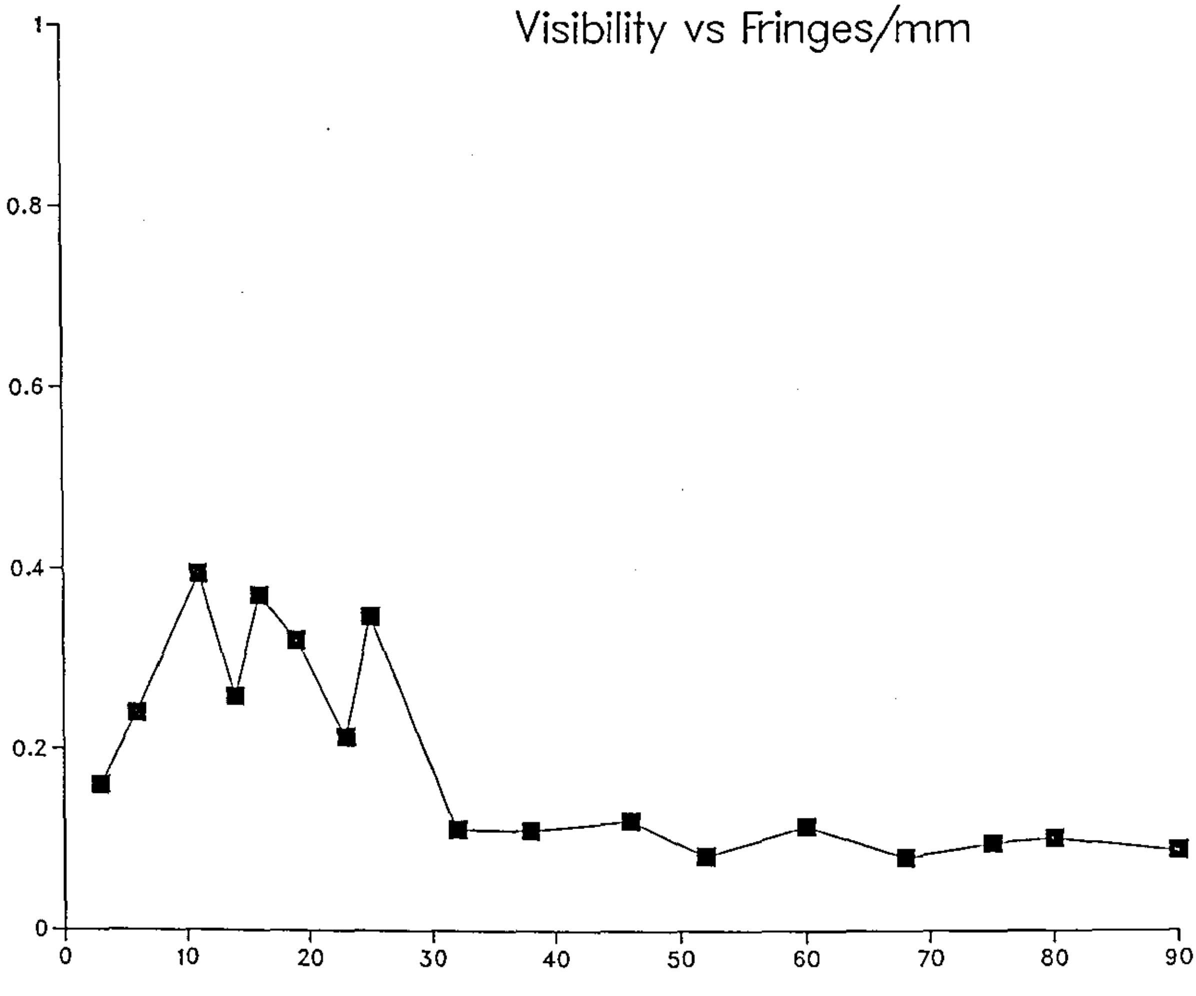

Figure 4.2
Plot of data in Table I. Aliasing is seen as harmonics
and sub-harmonics of the TV scanning rate.

FOOTNOTE: Amendment – page 114 does not exist.

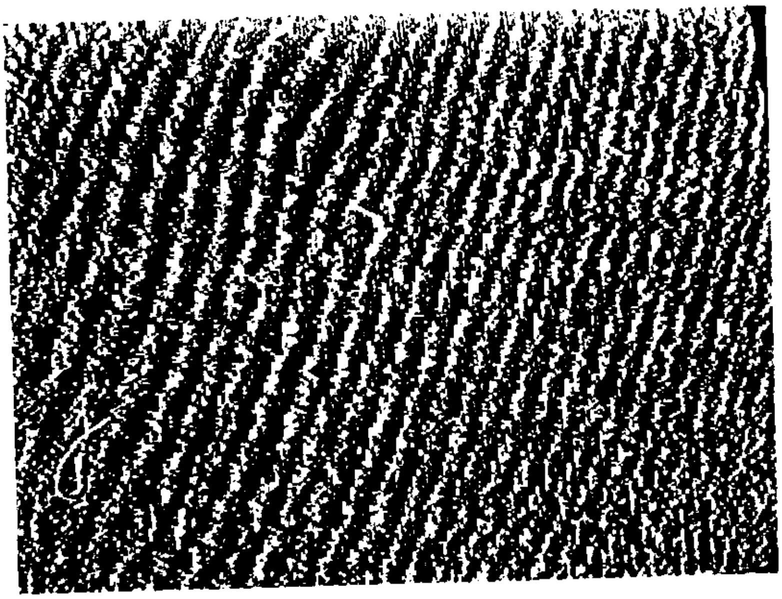

Figure 4.3
Photograph showing 16 fringes/mm
as seen on the monitor.

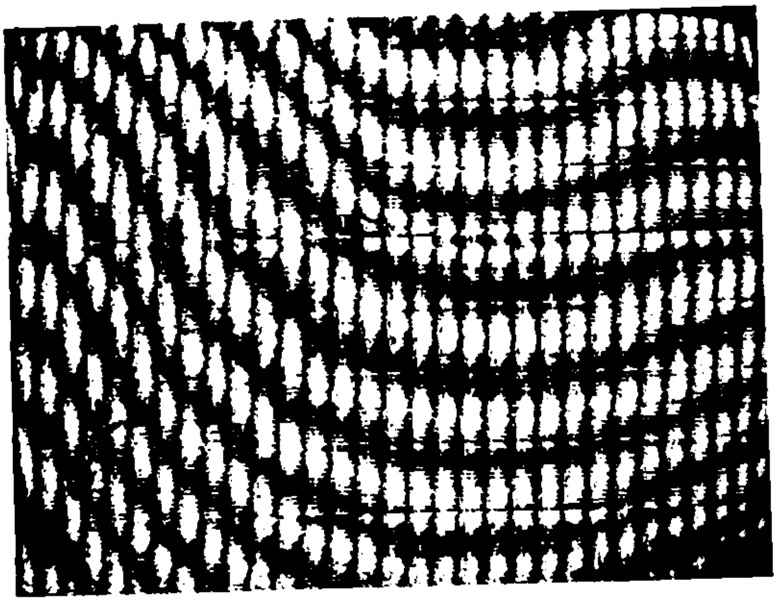

Figure 4.4
Subtraction of 16 - 19 fringes/mm to give
31 fringes across the monitor.

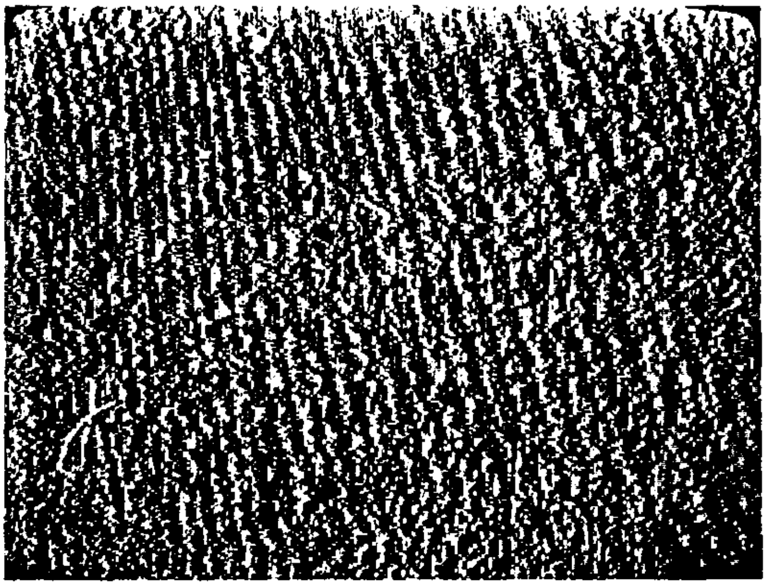

Figure 4.5
Photograph showing 19 fringes/mm.

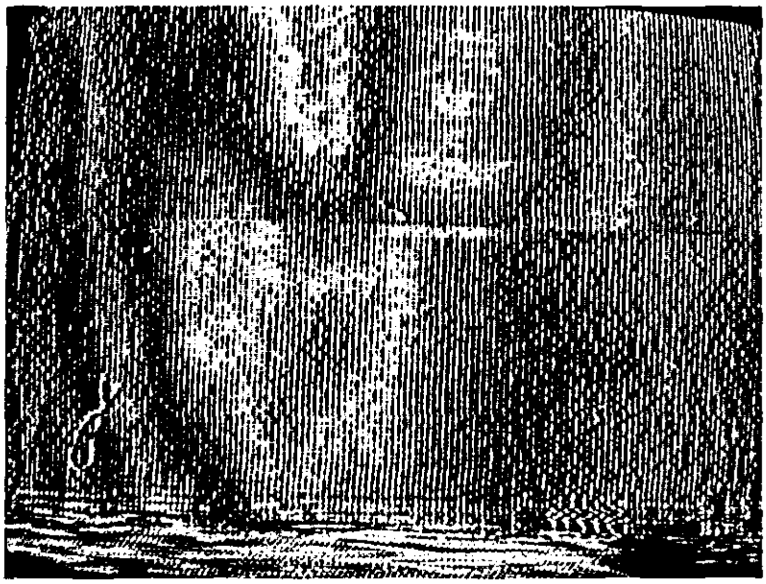

Figure 4.6
8 fringes/mm as seen on the monitor.

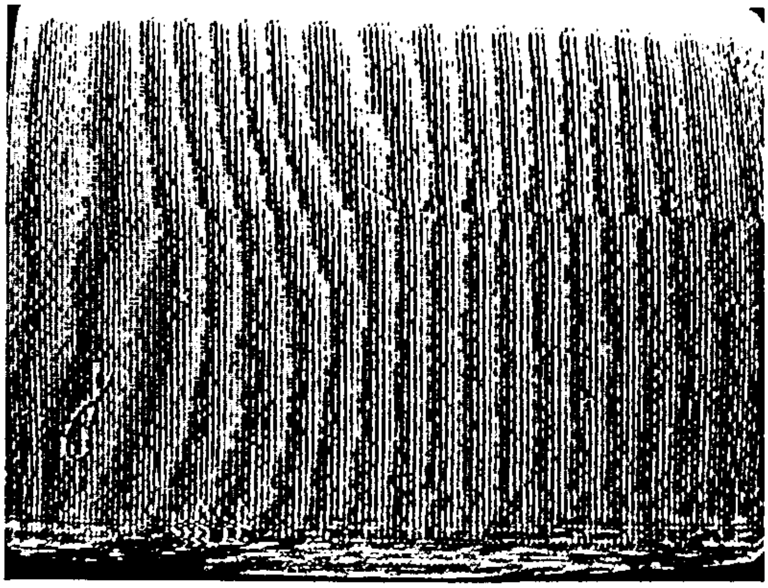

Figure 4.7
Photograph showing 10 fringes/mm.

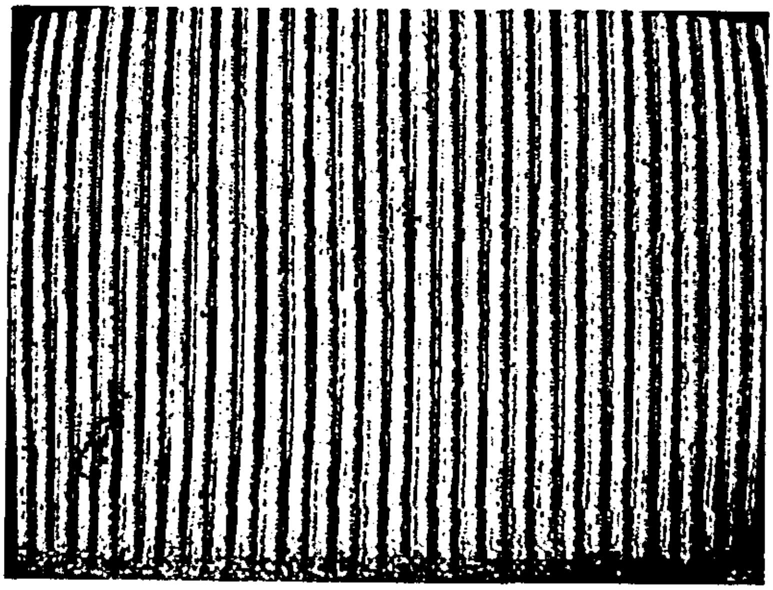

Figure 4.8
Subtraction of 10 - 12 fringes/mm to give
31 fringes across the TV monitor.

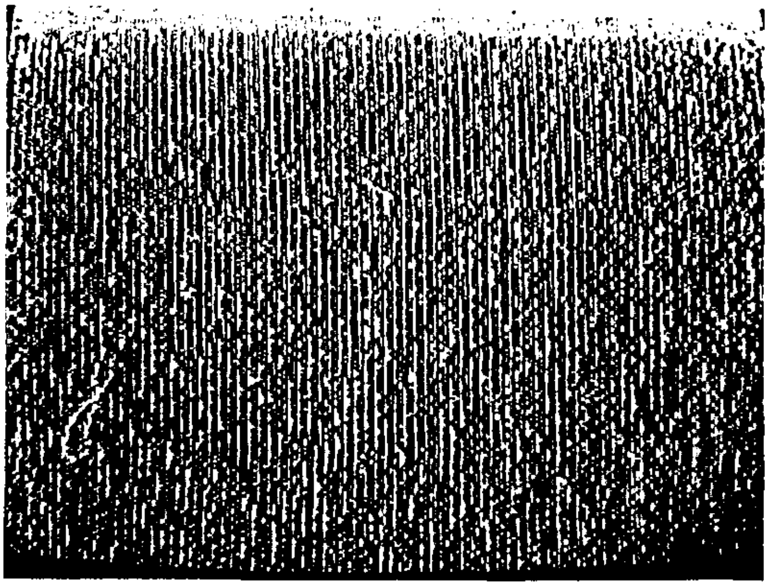

Figure 4.9
12 fringes/mm.

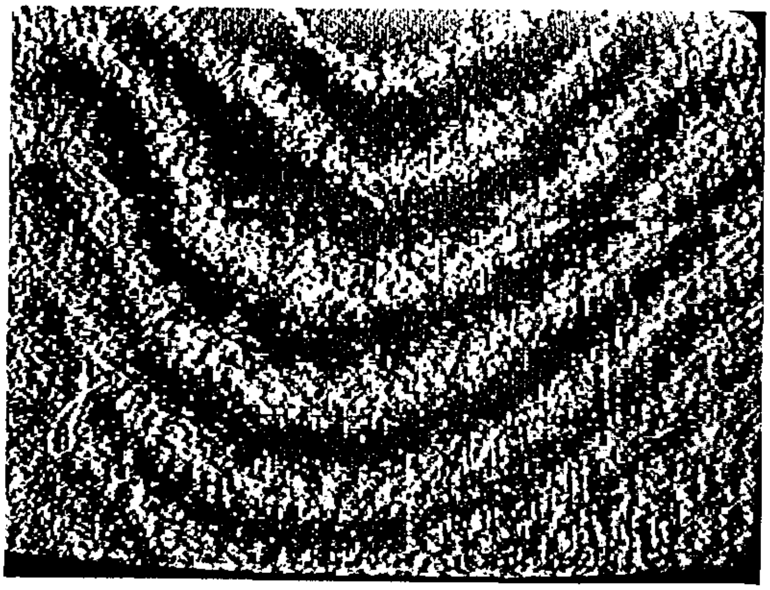

Figure 4.10
17 fringes/mm as seen from the monitor.

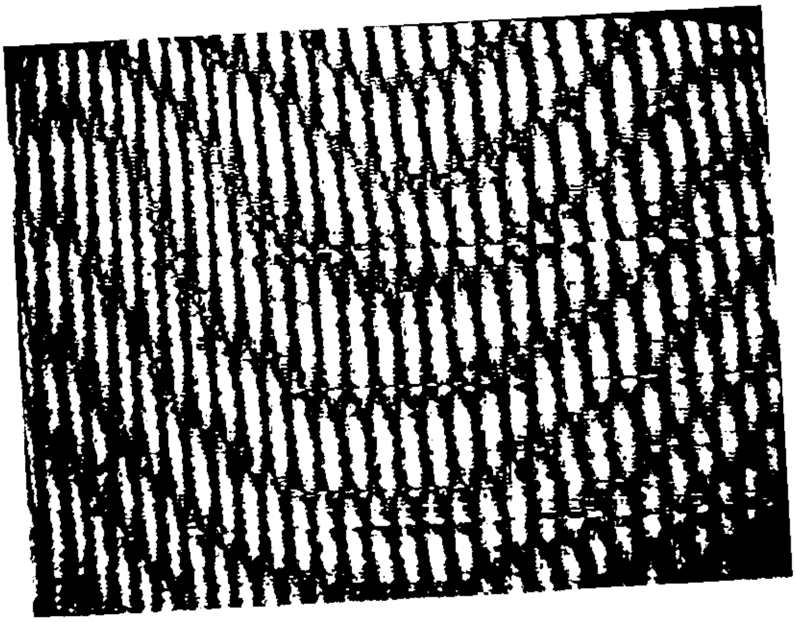

Figure 4.11
Subtraction of 17 - 20 fringes/mm giving
31 fringes across the monitor.

All the results given above relate to the performance of the electronic system in ESPI. On comparing the experiments done here with a real ESPI the following features are noticed:

The average size of a speckle (without including a reference beam into the picture) in an ESPI system is given by:

$$\sigma = 2(1.22\ \lambda\ f/\#) \tag{2}$$

with $f/\# = f/D$. f is the focal length of the imaging lens and D its aperture diameter. So, for the case when

$$f/\# < 29, \text{ and } \lambda = 0.6328\ \mu m \tag{3}$$

the average size of the speckles is smaller than the pixel size given in this Chapter, and bigger for $f/\# > 29$. In any case the ESPI correlation fringes obtained on subtraction of two consecutive speckle patterns are the result of the electronic system averaging the intensity falling over each pixel. The fact that aliasing is not present in (generally) ESPI correlation patterns is due to the randomness of the speckle pattern due to a normal object and reference beam. These results were obtained with virtually unspeckled wavefronts.

4.5 Closure.

Aliasing develops independently of the spatial frequency of the fringes, mainly due to the fact that there is no locking of the phase for the incoming signal, as happens for the particular case worked here. Therefore (as is shown in the Photographic Speckle Pattern Interferometry Chapter VI where the same type of correlation fringes were obtained without the use of electronic systems), aliasing does not occur in ESPI. The fringes displayed in ESPI are due to the correlation between the speckle patterns to be subtracted (added).

The random distribution of this patterns at the plane of the photosurface is the key to the absence of aliasing in ESPI. Thus the overall effect of the electronic system on the speckle pattern is to produce an average of the intensity falling in every pixel.

CHAPTER V
SYSTEM RESOLUTION

5.1 Introduction.

When object wavefronts coming from the resolution area defined by the viewing system interfere with reference wavefronts at the plane of the TV photosurface, they form a fringe pattern whose spatial frequency will be described next. It will then be possible to assess the resolution capabilities of the ESPI electronic system.

To calculate the interference at this plane, it is assumed that the reference beam is parallel to the optical axis (in the image space) and interfering at an angle θ with the object beam. This assumption will only simplify the theoretical solution, placing a lower limit to the high and intricate distribution of spatial frequencies found when the solution considers all the possible interference angles for the different beam geometries.

5.2 Electronic Resolution Limit.

With reference to figure 5.1, the effective measured dimensions of the TV photosurface in the X,Y directions are: i_x = 12 mm., and i_y = 8 mm. The electronic pixel addressing is 512 x 512. This figure is set by the space allocated in the system electronic memory. For this particular system the pixel size is: d_x = 23.4 μm., and d_y = 15.6 μm. Therefore if it is assumed that the maximum number of fringes to be resolved is 1 fringe/pixel, the maximum resolvable fringes will be

$$r_x = (1/2)\ d_x^{-1} \simeq 21 \text{ fringes/mm} \qquad (1)$$

and

$$r_y = (1/2)\ d_y^{-1} \simeq 32 \text{ fringes/mm} \tag{2}$$

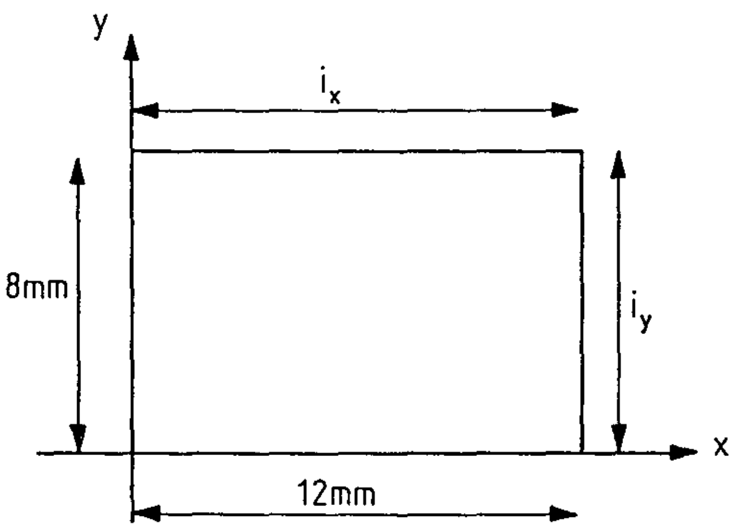

Figure 5.1
Dimensions of the TV photosurface.

The maximum phase gradient is:

$$(\partial \phi / \partial x)_{max} = \pi\ d_x \tag{3}$$

and

$$(\partial \phi / \partial y)_{max} = \pi\ d_y \tag{4}$$

for the X and Y directions respectively.

5.3 Spatial Frequency of the Interference Pattern.

Figure 5.2 shows the simple case of an object ray (coming from a point on the object surface) intersecting the photosurface at its corresponding image point. This ray represents the central ray of a light beam coming from the object resolution cell. It interferes with the reference beam, assumed to be parallel to the optical axis, forming a fringe pattern on the image plane of the object.

The fringe spacing for this kind of interference is:

$$d = \lambda/(2\sin(\theta/2)) \qquad (5)$$

with a phase gradient of

$$\nabla \phi = 2\pi\lambda/(2\sin(\theta/2)) \qquad (6)$$

The fringe spacing given by eq.(5) is that for a region of constructive interference to the next constructive zone, i.e. from bright to bright fringe.

If the TV system is to resolve the above interference pattern, then it is required that

$$d = \lambda/(2\sin(\theta/2)) \geq 2d_{x,y} \qquad (7)$$

$$\Rightarrow \sin(\theta/2) \leq \lambda/(4d_{x,y}) \qquad (8)$$

Therefore for object rays coming at an angle (in the image space)

$$\theta \leqslant \theta_{max} = 2\sin^{-1}(\lambda/(4d_{x,y})) = \begin{cases} \theta_{max\ x} = 0.7735^\circ \\ \theta_{max\ y} = 1.1602^\circ \end{cases} \qquad (9)$$

the ESPI electronic system will resolve the interference pattern formed by the object and reference beams under the assumptions made before.

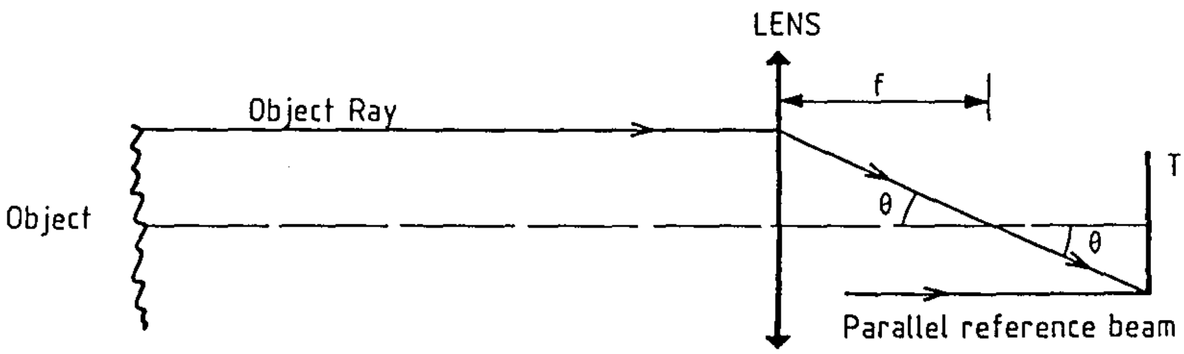

Figure 5.2
Interference of two parallel beams
at an angle θ.

Using figure B5.1 and eqs(B.5.10) and(B.5.11) in Appendix B, it follows that:

$$h_{xmax} = i_{xmax}\ u/v \qquad \text{and} \qquad h_{ymax} = i_{ymax} u/v \tag{10}$$

$$D_{xmax} = i_x + 2\ v\ \tan\theta_{xmax} \qquad \text{and} \qquad D_{ymax} = i_y + 2\ v\ \tan\theta_{ymax} \tag{11}$$

where:

a) $h_{x,y\ max}$ represent the extreme object points that contribute to their corresponding image points at the edge of the photosurface. The fraction u/v is the imaging lens magnification and therefore eq. (10) also represents any object point when $i_{x,y\ max}$ is replaced by the point conjugate.

b) $D_{x,y\ max}$ is the maximum aperture diameter to which the imaging system should be opened to for the system to resolve the contribution from the extreme points mentioned above. Increasing the aperture means that the electronic system will not be able to resolve the interference completely. This aperture is symmetrical with respect to the optical axis, but only a finite portion of it (in the shape of a cone of angle $2\theta_{x,y\ max}$) contributes with object rays whose interference with the reference beam is resolved (see Apendix B).

c) u is the object to lens distance; v is the lens to image distance; $\theta_{x,y\ max}$ are given by (9) and $i_{x,y}$ are the photosurface dimensions.

Table 5.1 shows different values for relations (10,11) for the angles in (9), the edges of the photosurface (i_x = 12 mm, and i_y = 8 mm) and u = 600 mm. M is the magnification of the imaging system and f its focal length.

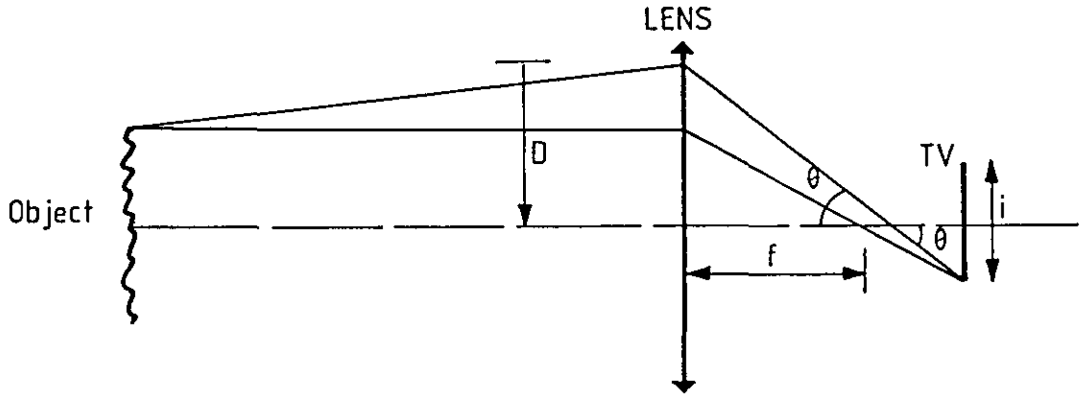

Figure 5.3
Geometrical optics raytracing of
object imagery.

TABLE 5.1

M	1/11	1/5	1/3	1/2	1/1	2.15
f (mm)	50	100	150	200	300	410
$D_{x\ max}$ (mm)	13.47	15.24	17.4	20.1	28.2	46.96
$D_{y\ max}$ (mm)	10.21	12.86	16.1	20.15	32.3	60.44
$h_{x\ max}$ (mm)	132	60	36	24	12	5.56
$h_{y\ max}$ (mm)	88	40	24	16	8	3.71
f/# $\geq$	3.71	6.56	8.62	9.93	9.29	6.78

For object points smaller than those represented by $h_{x,y\ max}$ the corresponding values for $D_{x,y\ max}$ change accordingly to (11) and the values taken for $i_{x,y}$. The f/# obtained in the previous table indicates that for values of the f/# less than the ones quoted above the electronic system will not resolve the interference at the edges of the photosurface.

Following the criteria of eq. (5) the maximum spatial frequency to be found at the edges of the TV photosurface can be obtained by first finding the maximum angles subtended from the edges of the photosurface to the rim of the aperture in the lens. So, assuming symmetry in the optical system and within the limits of geometrical optics, it is found that (see fig. 5.3):

$$\tan\theta_{x,y} = (i_{x,y} + D_{x,y\ max})/(2v) \qquad (12)$$

where $\theta_{x,y}$ is the maximum value of the angles arriving at the edges of the photosurface, and $D_{x,y\ max}$ are the values given in table 5.1. Thus the effective angular spread for the point $i_{x,y}$ goes from $\theta_{x,y}$ to $-\theta_{x,y\ max}$. Substituting the angles found by eq. (12) into eq. (5) the fringe separation of the interference pattern for the $D_{x,y\ max}$ values in table 5.1 is obtained, namely:

$$d_{x,y} = \lambda/(2\sin(\theta_{x,y}/2)) \qquad (13)$$

Eq. (13) gives the separation between bright fringes.

Table 5.2 gives some specific data obtained from eqs. (12) and (13). In this i_x = 12 mm, i_y = 8 mm, u = 600 mm, and $D_{x,y\ max}$ assumes the values given in Table 5.1

TABLE 5.2

f (mm)	50	200	300	410
θ_x (degrees)	13.14	3.06	1.91	1.30
θ_y (degrees)	9.47	2.68	1.92	1.51
$1/d_x$ (lp/mm)	361.7	84.45	52.91	35.97
$1/d_y$ (lp/mm)	261.1	74.08	53.05	41.75

The lp/mm figures appearing in table 5.2 are the maximum values found in the image plane for the particular cases calculated there. These values spread to their lower limit given by eqs. (1) or (2) for the angles given in (9).

5.4 Discussion.

Eq. (13) was plotted against the object to lens distance in figures 5.4 to 5.8. They were obtained using the horizontal (x axis) and vertical (y axis) characteristics of the system, respectively.

From tables 5.1 and 5.2 it is seen that there must be a compromise between the importance, if any, of resolving the interference pattern created from object and reference beams and the size of the object under study. That is, if what is required is to observe an object of dimensions in the order of decimeters or more it will be necessary to use (for a fixed working distance from object to imaging lens) a wide angle lens if the whole object is to be observed (unless it is possible to see it with a normal or telephoto lens).

Consider now a constant object to lens distance. If the interference pattern is to be resolved, then from the graphs it is noticed that the longer the focal length used the lower the spatial frequency becomes. For instance using a 410 mm telephoto lens with an f/# of 6.78 an object of 20.63 mm^2 will be fully resolved if a parallel reference beam is used.

Due to the non-square shape of the active photosurface the imaging system resolving power is different in the horizontal direction as compared to the vertical direction, this being reflected in figs. 5.4 to 5.8, and table 5.2. The spatial frequency behaviour did not show a considerable change for the case when the object profile changes appreciably in the optical axis direction, showing a rather small change for small surface variations. Thus for a given focal length lens some amount of depth of focus might be needed for large object profile changes, this dependence decreasing for bigger focal lengths. However, it should be pointed out that a small aperture system used to increase the depth of focus will not prove to be efficient, mainly due to the fact that it will increase the already high variation of spatial frequencies with distance existent on the photosurface (besides decreasing the light level at the plane of the image).

In most ESPI systems there is a tendency to use small apertures to increase the speckle size and therefore be able to resolve it. However, experiments done in Chapter III with the beam splitter in front of the imaging lens, and not in between this and the photosurface, show that a full aperture lens can be used, giving an overall improvement in the displayed fringe visibilities. The aperture in this case acts as an entrance pupil to the system.

In section 3 it was mentioned that there exists a slit like aperture (defined in Appendix B) immersed within the full real circular aperture, that allows object rays to get through the system and form a resolvable interference. This slit aperture has a definite angular interval such that angles outside this interval will contribute with highly oblique object rays whose interference at the image plane will not be resolved.

The attention is now drawn to the resolution cell on the TV photosurface, e.g. the pixel. The object contribution to the interference within the pixel comes from a cell the size of the resolution area given by the imaging system (depending inversely on the radius of the aperture). If the corresponding (conjugate to the pixel area) cell dimensions in the object space are bigger than the object resolution cell (as defined by the viewing system) then more than one point in the object space contributes to this pixel, and only one if the conjugate cell is smaller. In any case, within the pixel area only object rays having angles defined by relation (9) will contribute to the resolvable interference.

From the above, it is clear that the pixel averages (or integrates over its surface) the total intensity falling on it. This specific pixel operation is used throughout the Thesis.

Finally it must be mentioned here that the previous modelling of the present chapter problem was a particular solution of the more general case where the following items must be considered: 1) different beam geometries, 2) scattering properties of object surface (dealt with in Chapter II), and 3) introduction of aberrations, such astigmatism (exacerbated when using the plane-wedge beam splitter in between the lens and photosurface) or sphericity. Nonetheless, the solution presented here acts as a guideline to the general optical parameters required for an optimum system.

5.5 Closure.

The angles $\theta_{x,y\ max}$ for which the system resolved the interference between object rays and a parallel reference beam depended only on the photosurface dimensions and electronic addressing capabilities, e.g. number of pixels. To resolve this interference long focal length lenses should be used or a high magnification instead, both ways reduced the actual object area under study. There was not any aperture limitation other than that imposed by $\theta_{x,y\ max}$ and the edges of the photosurface (see table 5.1).

The use of small apertures will introduce a larger depth of focus and extra spatial frequencies that will only worsen the resolution problem. Increasing thus the speckle size is not needed. Thus large aperture can be used reducing in this way the need for greater laser outputs.

It can be safely said that due to the presence of high spatial frequencies dominating the complex pattern of interference and thus the inability of the system to resolve it the total intensity present on each pixel is averaged to give a mean intensity per pixel.

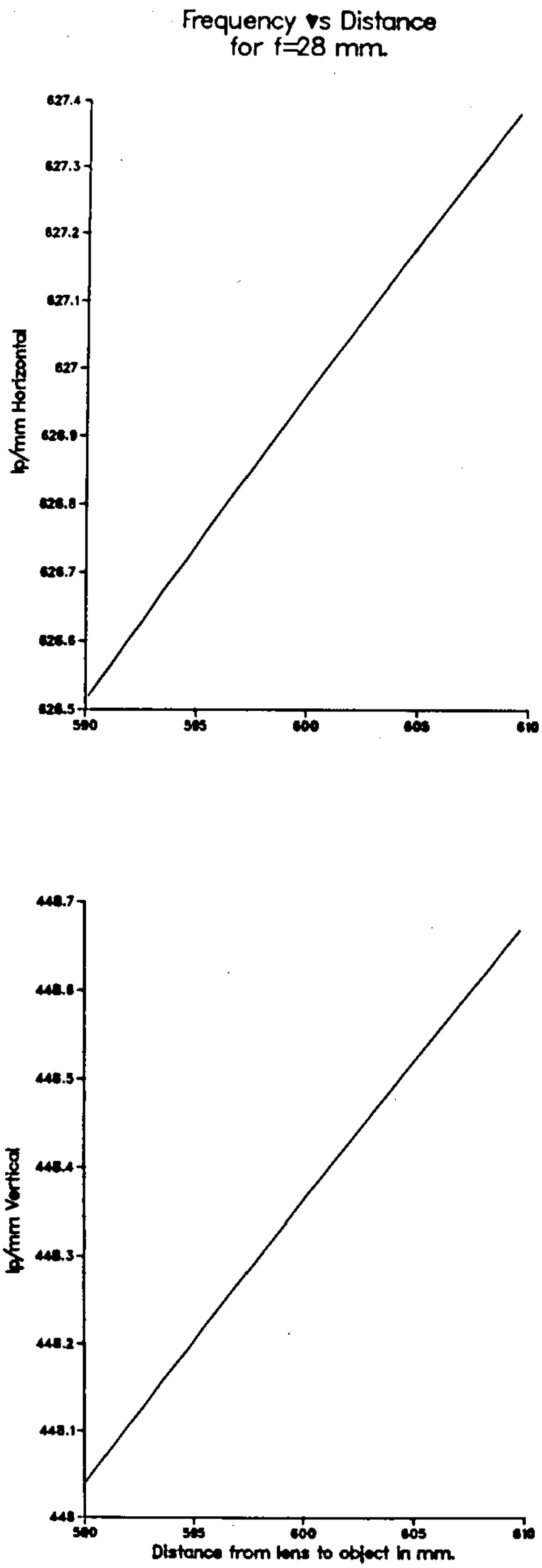
Frequency vs Distance
for f=28 mm.
627.4
627.3
627.2
627.1
627
626.9
626.8
626.7
626.6
626.5
lp/mm Horizontal
590
595
600
605
610
448.7
448.6
448.5
448.4
448.3
448.2
448.1
448
lp/mm Vertical
590
595
600
605
610
Distance from lens to object in mm.

Figure 5.4

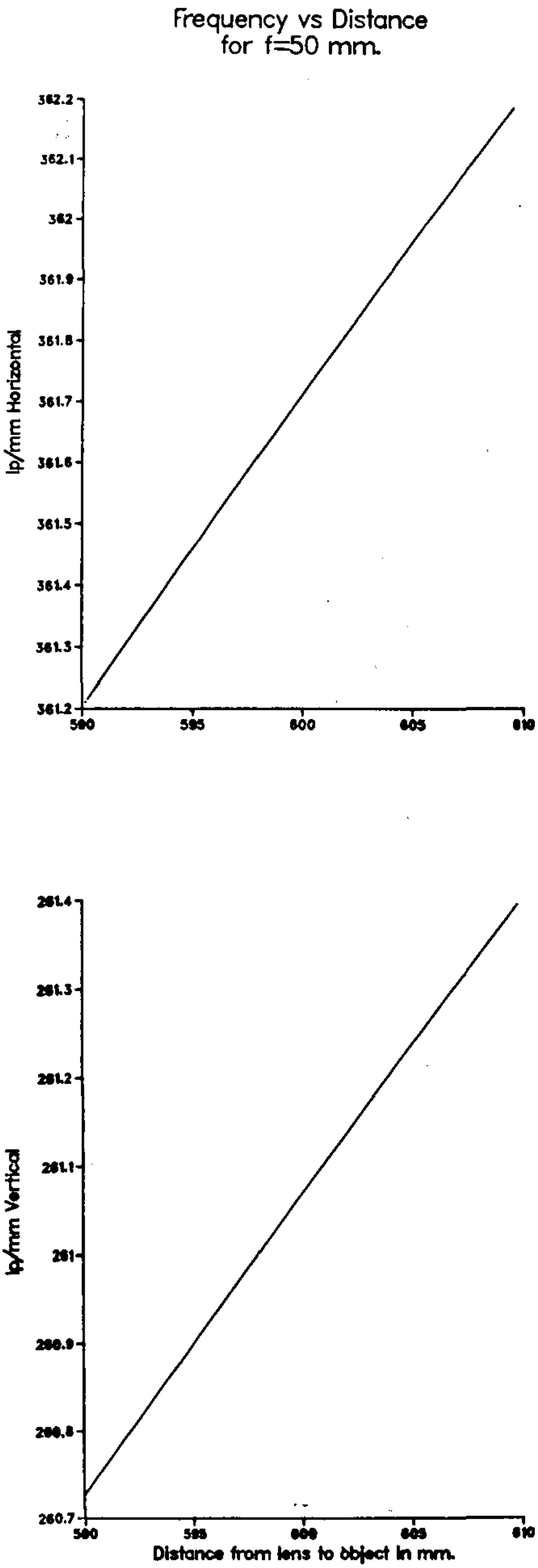
Frequency vs Distance
for f=50 mm.
lp/mm Horizontal
362.2
362.1
362
361.9
361.8
361.7
361.6
361.5
361.4
361.3
361.2
590
595
600
605
610
lp/mm Vertical
261.4
261.3
261.2
261.1
261
260.9
260.8
260.7
Distance from lens to object in mm.

Figure 5.5

Frequency vs Distance
for f=50 mm.

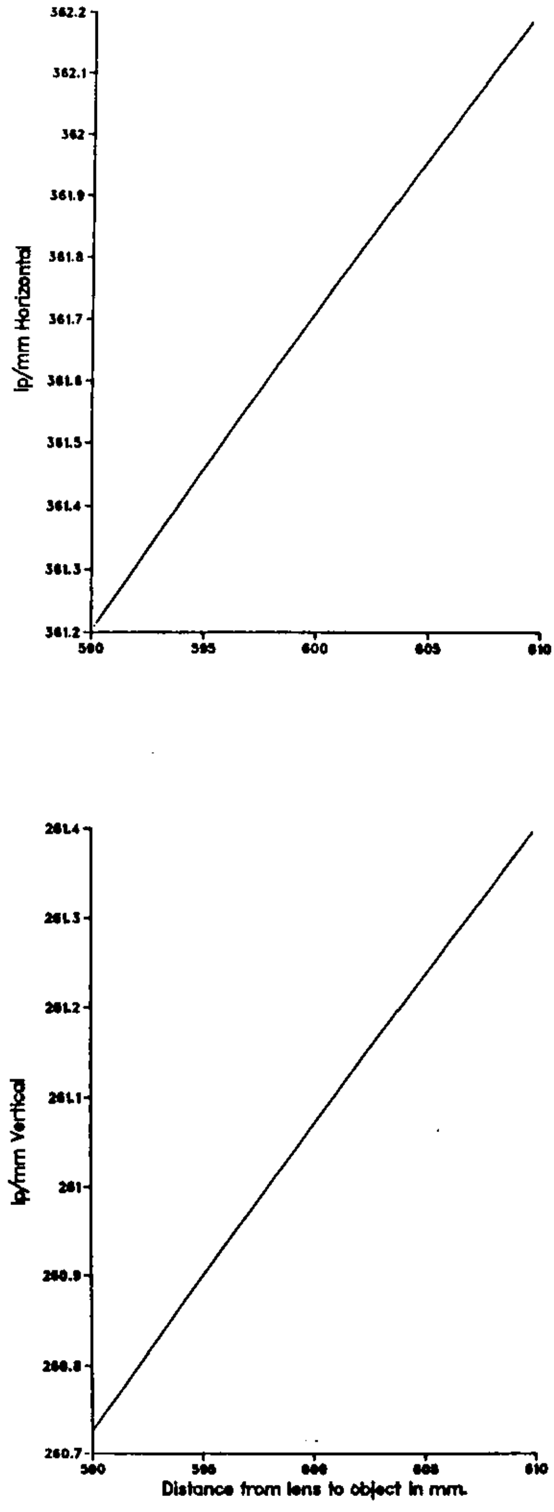

Figure 5.5

Frequency vs Distance
for f=200 mm.

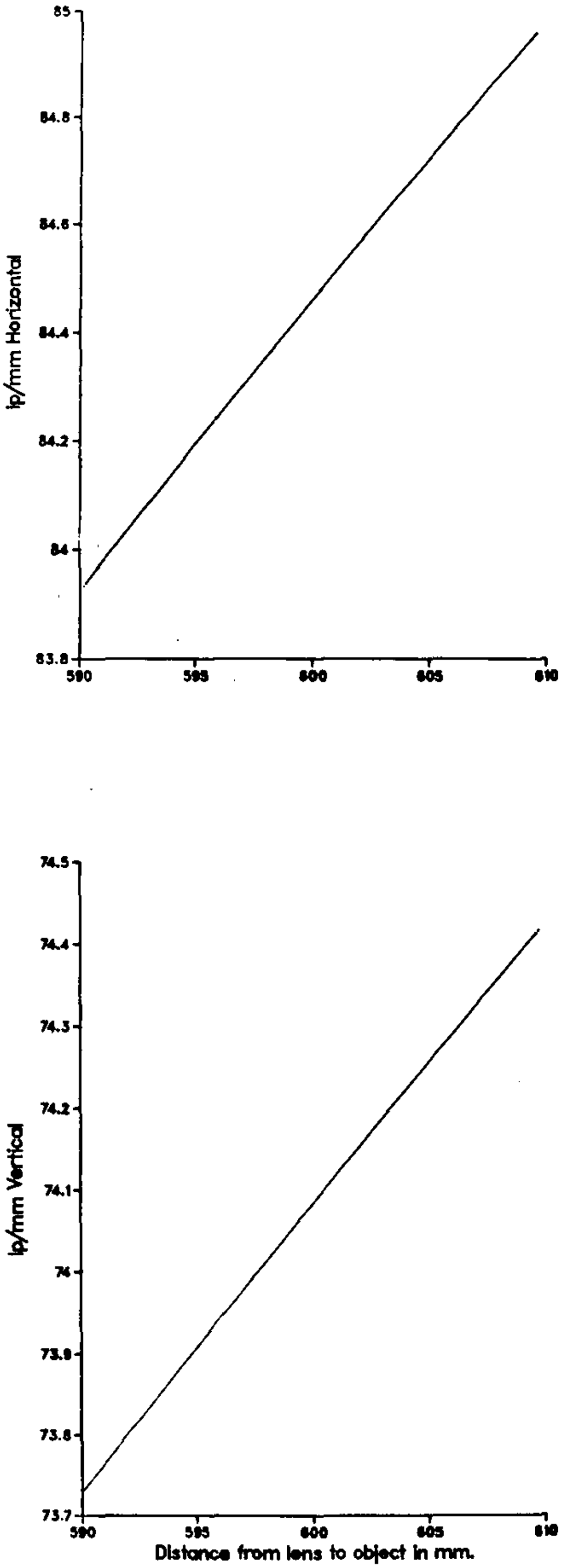

Figure 5.6

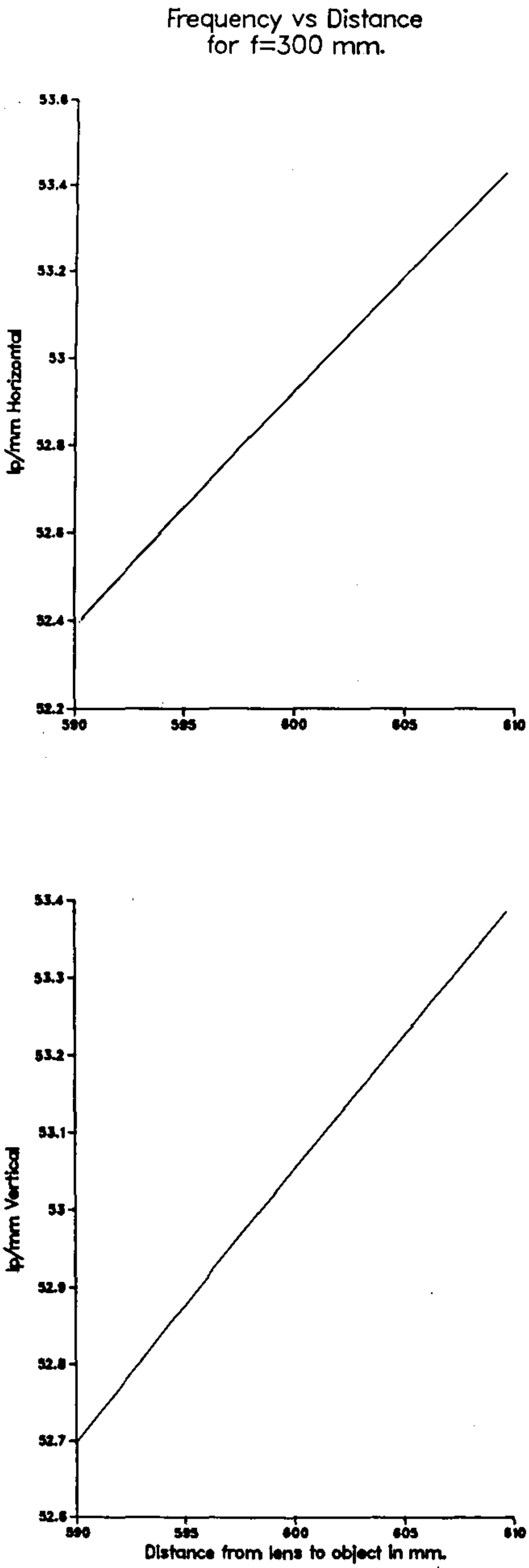
Frequency vs Distance
for f=300 mm.
lp/mm Horizontal
53.6
53.4
53.2
53
52.8
52.6
52.4
52.2
590
595
600
605
610
lp/mm Vertical
53.4
53.3
53.2
53.1
53
52.9
52.8
52.7
52.6
590
595
600
605
610
Distance from lens to object in mm.

Figure 5.7

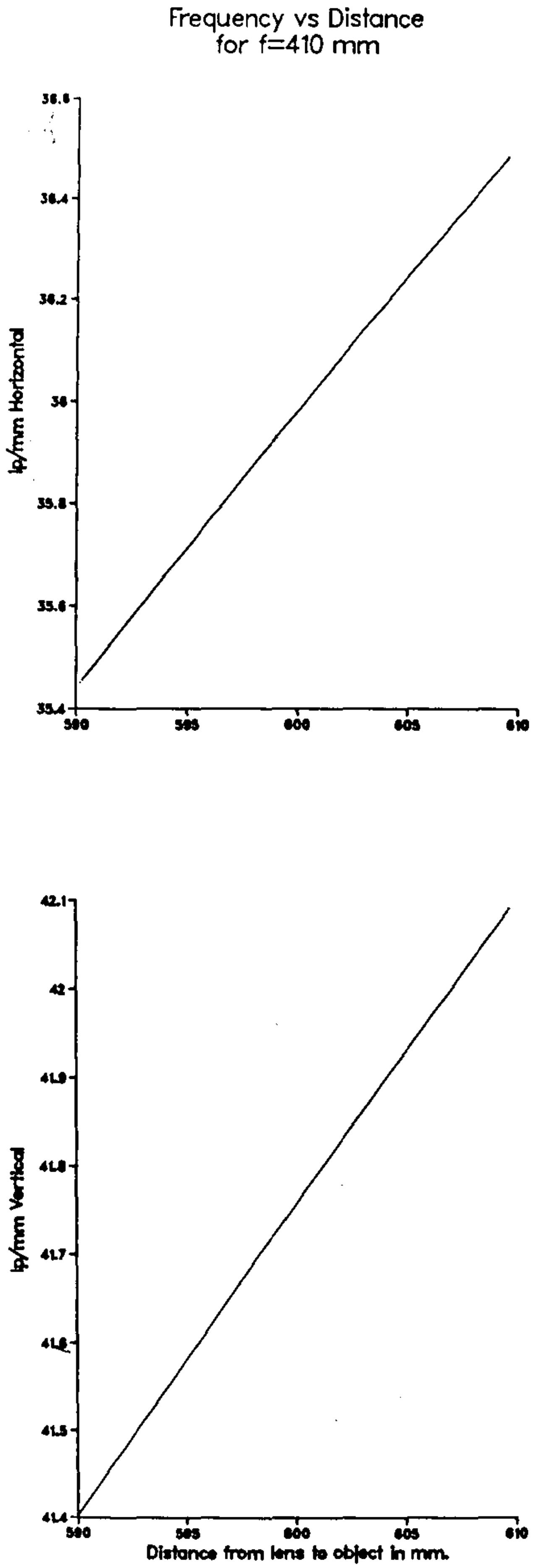
Frequency vs Distance
for f=410 mm
lp/mm Horizontal
36.6
36.4
36.2
36
35.8
35.6
35.4
590
595
600
605
610
lp/mm Vertical
42.1
42
41.9
41.8
41.7
41.6
41.5
41.4
590
595
600
605
610
Distance from lens to object in mm.

Figure 5.8

CHAPTER VI
PHOTOGRAPHIC SPECKLE PATTERN INTERFEROMETRY

6.1 Introduction.

The present Chapter introduces a double exposure photographic technique that displays, on a single film frame, speckle (addition) correlation fringes identical to those obtained (on subtraction) with ESPI. This double exposed photograph can be spatially Fourier filtered to eliminate the optical noise giving an image of holographic quality. The information given by the Fourier spatial spectrum of the deformed object is being introduced as an electronic filter into ESPI.

A theoretical account of the above process follows.

6.2 Theory.

It is possible to describe in simple terms the interference between the reference (divergent beam) and object waves as (fig. 6.1):

$$U_r + U_o \tag{1}$$

where,

$$U_r = u_r \exp\{i\phi_r\} \tag{2}$$

and

$$U_o = u_o \exp(i(\psi_o + \phi_o)) \tag{3}$$

are the complex amplitudes for the reference and object waves respectively; ϕ_r is the reference wave phase, ψ_o is the random speckle phase and ϕ_o is a phase term function of position across the object. A diverging reference beam has been assumed, as is commonly the case in ESPI. (Bergquist and Mendoza Santoyo [17] found that the optimum arrangement may well be a slightly converging reference wavefront).

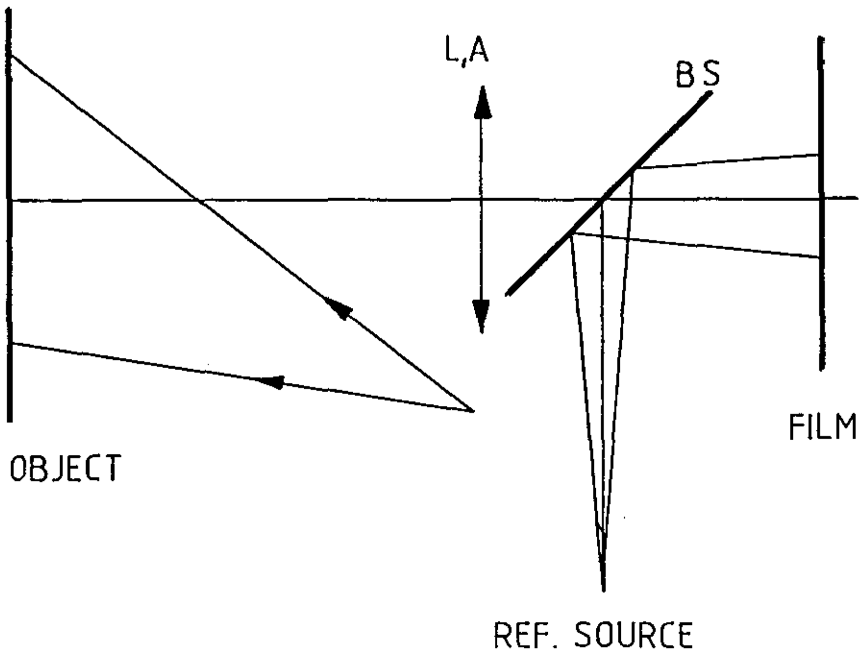

Figure 6.1.
Interferometer set-up for double exposure photograph. BS is the beam splitter and L,A is the lens aperture combination.

For a stationary object:

$$\phi_r = \phi_r(x,y)$$
$$\psi_o = \psi_o(x,y) \qquad (4)$$
$$\phi_o = \phi_o(x,y)$$

where the (x,y) coordinates are referred to the photographic film.

The incident intensity on the plate for the first exposure is:

$$I_1(x,y) = I_r + I_o + 2\ (I_r I_o)^{1/2}\ \mathrm{Re}(\exp(i(\psi_o + \phi_o - \phi_r))) \qquad (5)$$

The second exposure is taken after the object has been disturbed, introducing a phase change $\Delta\phi = \Delta\phi(x,y)$ in the object wave, i.e.

$$U_o' = u_o \exp(i(\psi_o + \phi_o + \Delta\phi)) \qquad (6)$$

where it has been assumed that the intensity on the plate, due to the object phase shift, has remained constant. Hence, the intensity on the plate for the second exposure takes the form:

$$I_2(x,y) = I_r + I_o + 2\ (I_r I_o)^{1/2}\ \mathrm{Re}(\exp(i(\psi_o + \phi_o + \Delta\phi - \phi_r))) \qquad (7)$$

To find the brightness of the final image on the film due to eqs.(5) and (7) the Hurter and Driffield (H-D) curve is recalled. It gives, over the linear region:

$$\log\ (D) = \Gamma\ \log\ (e) \qquad (8)$$

where: D is the film density, e the exposure, and Γ a constant dependent on the type of film, and developer used. Γ can be controlled over a wide range. Here, the usual assumption that $\Gamma = 2$ is made; the brightness obtained from eqs. (5) and (7) is then:

$$B(x,y) = (I_1 + I_2)^2 = 4(I_r + I_o + (I_r I_o)^{1/2}\ Mo)^2 \qquad (9)$$

where Mo is the fringe modulation function defined as:

$$Mo(x,y) = \cos(A) + \cos(A + \Delta\phi) = 2\cos(A + \Delta\phi/2)\cos(\Delta\phi/2) \qquad (10)$$

and $A = \psi_o + \phi_o - \phi_r$. The fringe function values are in the interval [-2,2].

The only noise component present in eq.(9) is optical noise of the form $(I_r + I_o)^2$. Accordingly an unrectified signal to noise ratio α can be defined as:

$$\alpha = Mo(Mo\ r + 2\ (r)^{1/2}\ (1 + r)) / (1 + r)^2 \qquad (11)$$

where: $r \equiv I_r/I_o$ is defined as the ratio of the reference to object beam intensities. α has a maximum for $r = 1$. Figure 6.2 shows plots of α vs $\Delta\phi$ for different values of A and two values of r. For $\Delta\phi = \pi$, $\alpha = 0$ in all cases. This represents the case for full phase reversal, i.e. dark fringes are obtained.

The contrast of the fringe pattern described by eq.(9) is usually defined as:

$$C \equiv (B_{max} - B_{min}) / (B_{max} + B_{min}) \qquad (12)$$

The actual contrast that can be achieved depends on the contrast and spatial frequency of the local speckle pattern. Interference fringe contrast approaching unity only occur when the speckle contrast is low, i.e. with smooth wavefronts. Typical values of contrast measured by averaging over many pixels are found to be up to 0.6 (Chapter III: for the case where the beam splitter lies in between the viewing lens and object). At the high spatial frequency limit, with high contrast speckles, the visibility is limited to 0.5. This is because the TV system sees an integrated speckle pattern due to the finite size of the TV pixel. For a half inch tube this measures some 12 x 7 μm, so spatial frequencies greater than 80 lp/mm are being considered here.

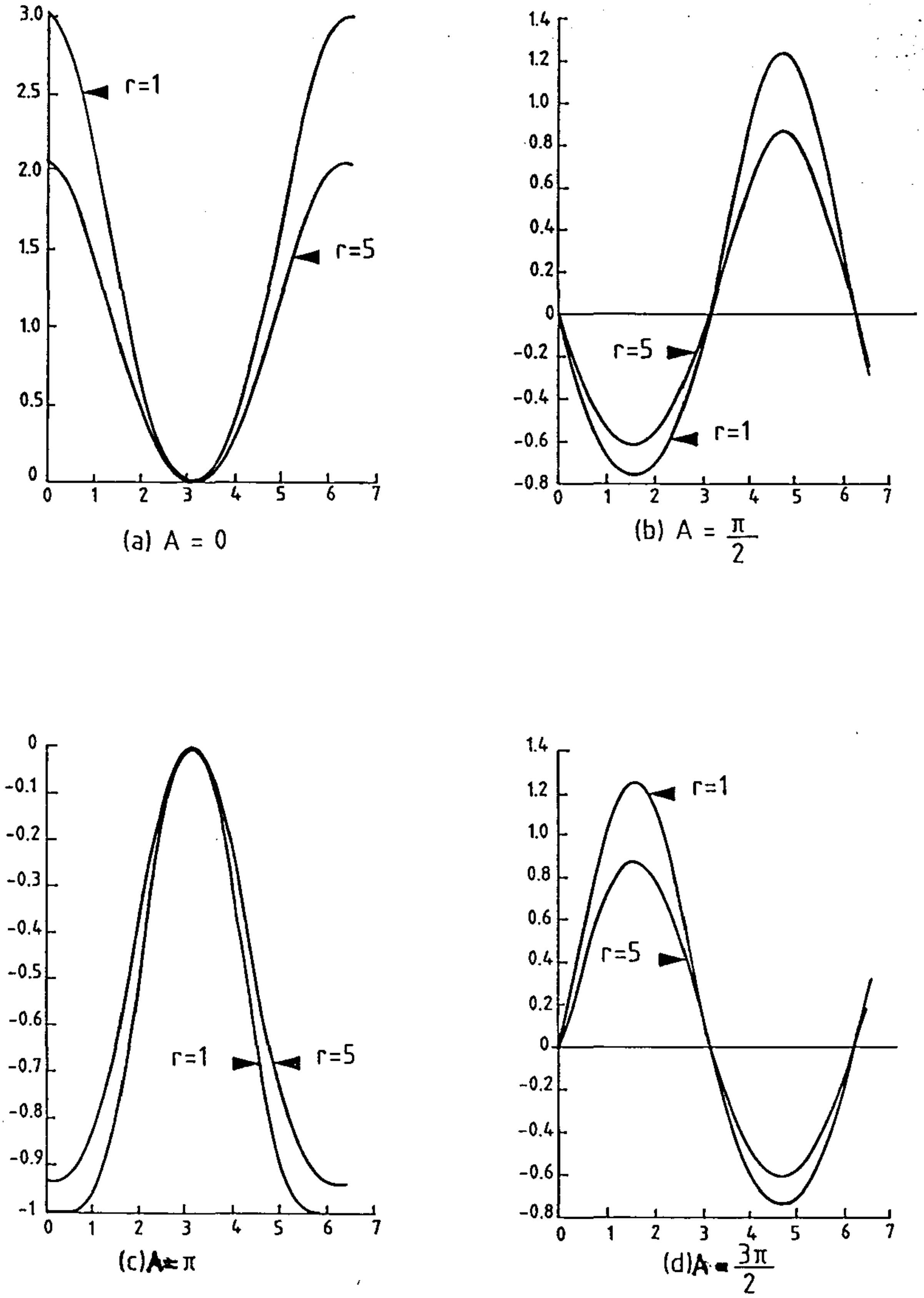

Figure 6.2
Plots of α, the unrectified signal to noise ratio, .vs. $\Delta\phi$ the object phase change (in radians). r is the reference to object beam intensity ratio.

After some basic algebraic manipulation eq.(12) becomes:

$$C = (2\ Mo_{max}\ (r)^{1/2}\ (1 + r))\ /\ ((1 + r)^2 + Mo_{max}^2\ r) \qquad (13)$$

Mo_{max} is the maxima of the fringe function Mo, eq.(10), for a constant value of $\Delta\phi$, and A as a variable. $Mo_{max}(\Delta\phi) \in [0,2]$. As expected, C has a maximum for r = 1. Figure 6.3 shows the plot of C vs $\Delta\phi$ for two values of r. For $\Delta\phi = \pi$ the contrast of the fringe pattern goes to zero.

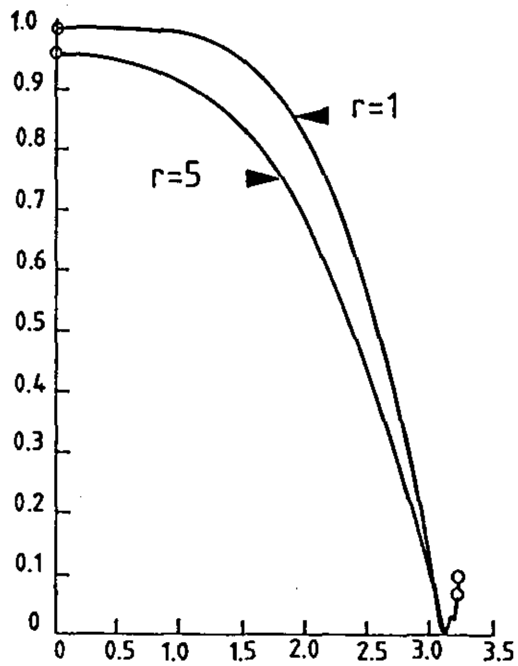

Figure 6.3
Plot of Contrast .vs. $\Delta\phi$ (in radians).

After the photographic film has been developed, a Fourier filtration system is employed to filter-out the optical noise from the transparency (figure 6.4a).

The total exposure at point (x,y) on the photographic plate is:

$$e(x,y) = (I_1 + I_2)\ t \tag{14}$$

having assumed that the individual exposure times are equal, e.g. $t_1 = t_2$ (this time will be taken as unity for the remaining part of the analysis). I_1 and I_2 are the intensities given by eqs. (5) and (7) respectively. If the exposures are confined to the linear part of the H-D curve of the film, the amplitude transmission g(x,y) of the plate is approximately:

$$g(x,y) = a - b\ e(x,y) \tag{15}$$

where a,b are positive constants. The Fourier transform of the transparency is then:

$$G(u,v) = \iint_{-\infty}^{+\infty} g(x,y)\ \exp(ik(ux + vy))\ dx\ dy \tag{16}$$

G(u,v) is the spectrum of the intensity distribution at the Fourier plane. The transform of eq. (15) is represented by (F(g) means the Fourier transform of g):

$$G(u,v) = a\ F(1) - b\ F((I_1 + I_2)) = a\ \delta(u,v) - b\ F((I_1 + I_2)) \tag{17}$$

The first term in eq.(17) occurs where the illuminating beam converges, i.e. the focal point of the lens in fig.6.4a. It contributes to the diffracted amplitude only at u = v = 0.

The Fourier transform of the second term is, using eqs.(5), (7) and (10):

$$F\{(I_1 + I_2)\} = \int\int_{-\infty}^{+\infty} (2(I_r + I_o) + 4 \ (I_r I_o)^{1/2} \ \cos(A + \Delta\phi/2) \ \cos(\Delta\phi/2))$$

$$\exp\{-ik(ux + vy)\} \ dx \ dy \tag{18}$$

Now, assuming I_r and I_o are constant during the double exposure experiment, eq.(18) takes the form:

$$F\{(I_1 + I_2)\} = 2(I_r + I_r) \ \delta(u,v) \ + 4(I_r I_o)^{1/2} \ F\{\cos(A + \Delta\phi/2)\cos(\Delta\phi/2)\} \tag{19}$$

Again the first term is light diffracted to the point u = v = 0, due to the reference and object beams. The second term is the Fourier transform of the fringe modulation function. Substituting eqs.(18) and (19) into (17) and then in (16), it is finally obtained:

$$G(u,v) = (a - 2 \ b \ (I_r + I_o)) \ \delta(u,v)$$
$$- \ 4 \ b \ (I_r I_o)^{1/2} \ \ F\{\cos(A + \Delta\phi/2) \ \cos(\Delta\phi/2)\} \tag{20}$$

Therefore outside the small area defined by u = v = 0 (which contains purely optical noise) it is seen that eq.(20) contains the information about the object distortion alone. Experimentally it is found that blocking the central portion of the transparency spatial spectrum in the Fourier plane, a neat and clear image of the object with the correlation fringes on it is obtained (see fig. 6.5).

To help visualize the physical significance of the Fourier transform appearing in eq.(20), the following geometrical example is given (fig. 6.4b). Using the real and imaginary notation of the Fourier transform ([32], pp. 63), F(Mo) takes the form:

$$F\{\cos(A + \Delta\phi/2) \ \cos(\Delta\phi/2)\} = \int\int_{-\infty}^{+\infty} \cos(A + \Delta\phi/2) \ \cos(\Delta\phi/2)$$

$$\exp\{-i \ k(ux + vy)\} \ dx \ dy \tag{21}$$

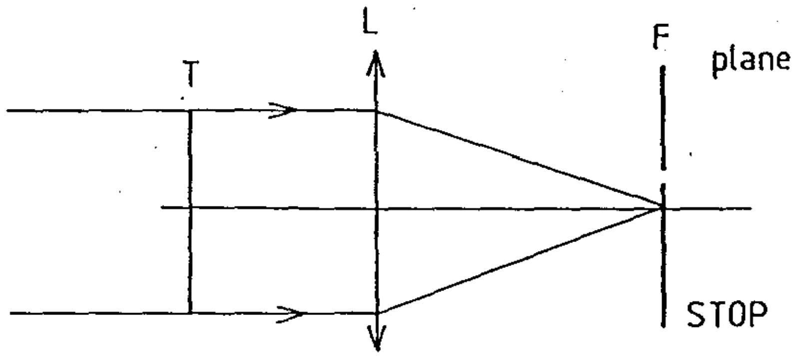

(a)

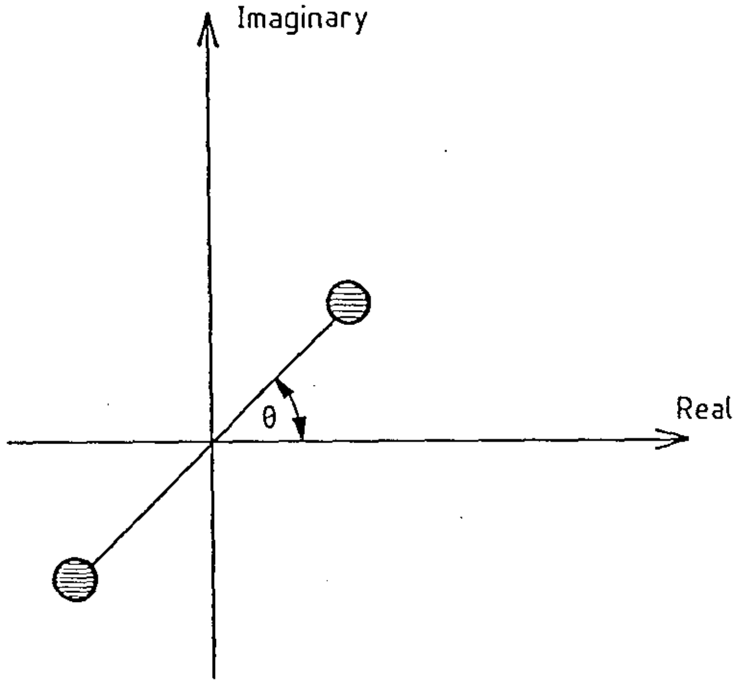

(b)

Figure 6.4
a) Fourier filtration technique used to recover the fringe information from the transparency (T). L is a single lens and F is the Fourier plane. b) A geometrical interpretation of eq.(20).

or

$$F\{\cos(A + \Delta\phi/2)\cos(\Delta\phi/2)\} = \iint_{-\infty}^{+\infty} (Mo(x,y)\cos(k(ux + vy)) + i\, Mo(x,y)\sin(k(ux + vy)))\, dx\, dy \qquad (22)$$

From this relation it is seen that the angle θ the secondary maxima (found in eq. (20)) make with the real axis (fig. 6.4b) is given by:

$$\theta = \tan^{-1}\left(\int_{-\infty}^{+\infty} Mo(x,y)\sin(k(ux+vy)))dxdy \Big/ \int_{-\infty}^{+\infty} Mo(x,y)\cos(k(ux+vy))dxdy \right\} \qquad (23)$$

Thus the secondary maxima will rotate around the origin $u = v = 0$ (see for instance the results in figures 6.5 and 6.8) depending on the functional form taken by the fringe function $Mo(x,y)$. In particular if $Mo(x,y)$ is given by a cosine function, θ will differ from 0 or 90° when the arguments of the Mo function and those of the sine and cosine appearing in the Fourier relation are equal, and thus $\theta = 45°$.

Returning to fig. 6.1, the marginal probability density function for the combination of the reference (smooth, coherent background) and object (speckled) intensities (I) at the image plane of the viewing lens (where the photographic film is placed) is given by ([33], pp. 29):

$$p_1(I) = (1/\langle I_N\rangle)\exp\{-(I + I_R)/\langle I_N\rangle\}\, J_o(2\,(I\, I_R)^{1/2}/\langle I_N\rangle) \qquad (24)$$

where the following assumptions were made:

a) The light intensity is measured at a single point,

b) The speckle pattern is polarized and independent of the coherent background,

c) The coherent background is of constant intensity and is co-polarized with the speckle pattern.

In eq.(24): $\langle I_N \rangle$ is the average intensity of the speckle pattern, I_R is the intensity of the smooth reference beam.

For the second exposure, when the object has undergone a displacement, the probability density function is the same as that of eq.(24), though individual speckle brightness may differ due to the change in phase while moving the object.

A double-exposed photograph is obtained of the undeformed and deformed object. The addition of the smooth reference beam to the speckle pattern creates a new overlying interference pattern resembling a speckle configuration in such a way that regions of this photograph where the interference between reference and object beams (for both exposures exhibit correlation between them) are alike will exhibit a probability density function given by eq.(25) where the most probable intensity is not zero (addition of two speckle patterns, [33], pp. 24 and full correlation).

$$p_2(I) = (4I/\langle I\rangle^2)\,\exp(-2I/\langle I\rangle) \qquad (25)$$

where $\langle I\rangle$ is the average intensity (measured at a single point) for the interference between the object and reference beams.

In areas where the phase shift has been equal to $(2n+1)\pi$, the overlying interference pattern of each exposure will be out of phase giving a probability density for uncorrelated speckle patterns of the form ([33], pp. 24):

$$p_3(I) = 1/\langle I\rangle\,\exp(-\,I/\langle I\rangle) \qquad (26)$$

where the most probable value of intensity is zero. As a result, the superposition of two overlying interference patterns (the one before the distortion and the one after) is displayed as fringes of correlated and uncorrelated patterns.

6.3 Experiments and Results.

Figure 6.1 displays the optical set-up where a 10 mW He-Ne laser was used to illuminate the object: a cantilever loaded plate. The imaging lens L had a focal length of 200 mm . An f/25 aperture was used in front of the imaging lens (ESPI works well down to apertures below f/4.5, [34]). The reference beam diverged from a point on the object-lens-film optical axis by means of a beam splitter. The image of the object was brought to a sharp focus, and at this plane the photographic plate was placed (Kodak Technical Pan film was used throughout). The first exposure was taken of the unloaded cantilever and then a second one with the load on. The film was then developed in Kodak D-19, and once dried is spatially Fourier filtered as in fig. 6.4a. The diffraction pattern of the transparency, fig. 6.5, consisted of a central undiffracted spot and two secondary maxima distributed symmetrically with respect to the central spot. Light from the secondary maxima was allowed to pass through the holes on the stop plate, shown in fig. 6.4a. A relatively noise-free interference pattern was observed against the object background. Photographic paper was used to capture this noise-free image. Figure 6.7 shows the spatially filtered transparency without the optical noise, displaying good visibility and high contrast fringes. Figure 6.6 shows the result (before filtering), where addition fringes are seen due to the bending of the cantilever. The optical noise (from the reference and object beams and from the beam splitter) reduced the visibility of the fringes. The effect of changing the loading conditions on the cantilever (and thus a change in Mo(x,y), eq.(10)) can be seen in figures 6.8, 6.9 and 6.10. The diffraction pattern of the transparency (fig. 6.8) showed the secondary maxima rotated with respect to those in fig. 6.5 as predicted by eq.(23).

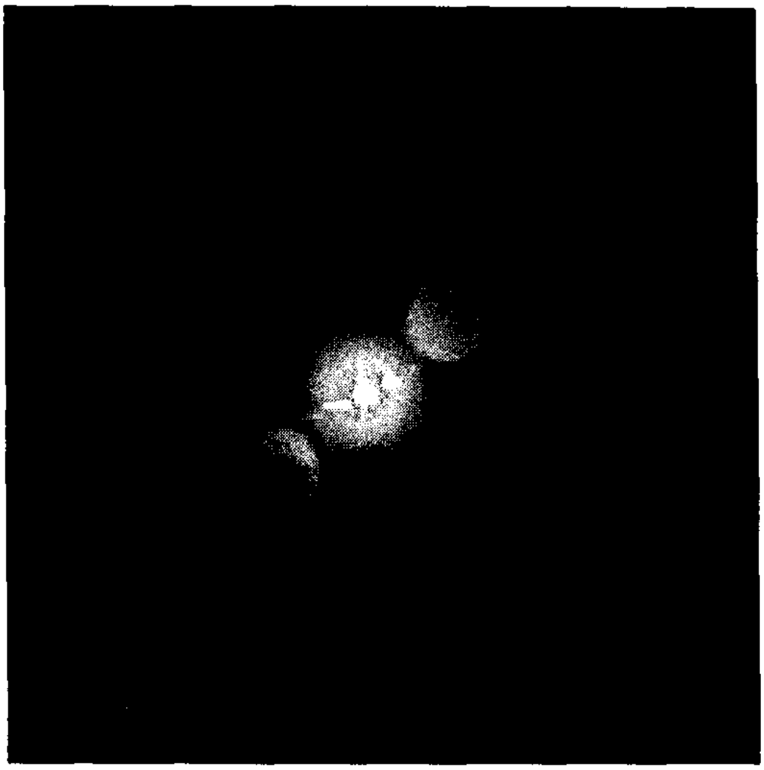

Figure 6.5
Spectrum of transparency in fig. 6.6. The two secondary maxima are easily seen (the one on the r.h.c. is +1).

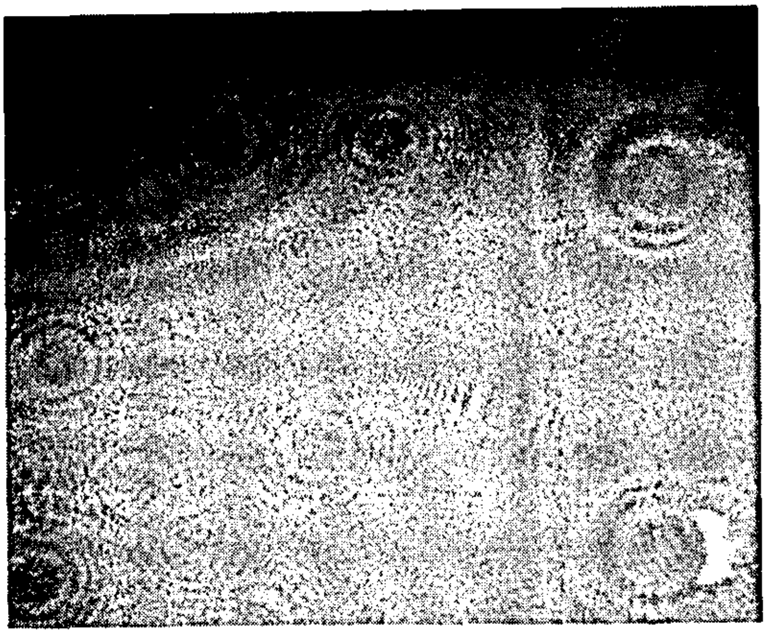

Figure 6.6
Photograph showing the double exposed object.
The optical noise is clearly seen.

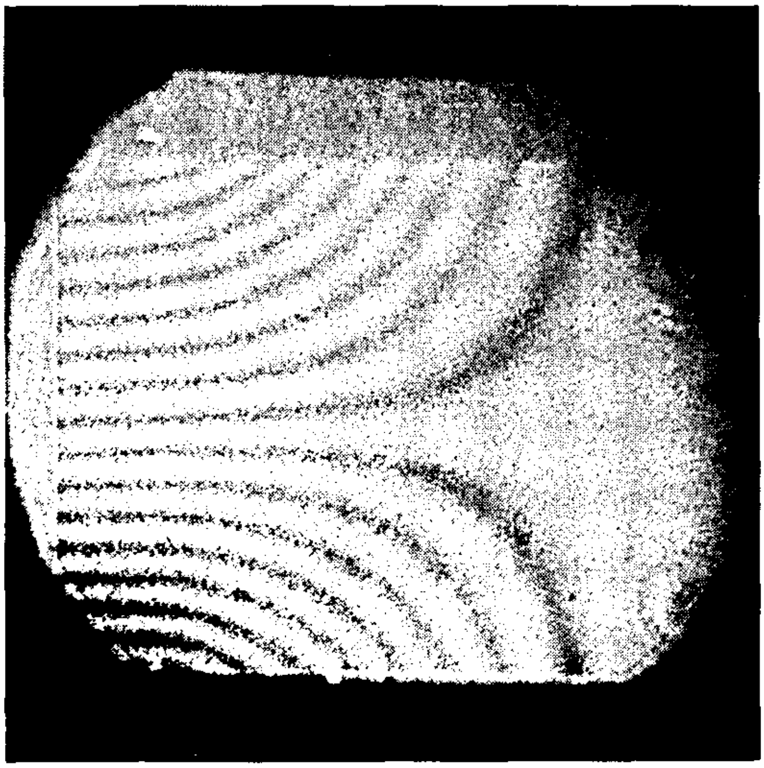

(a)

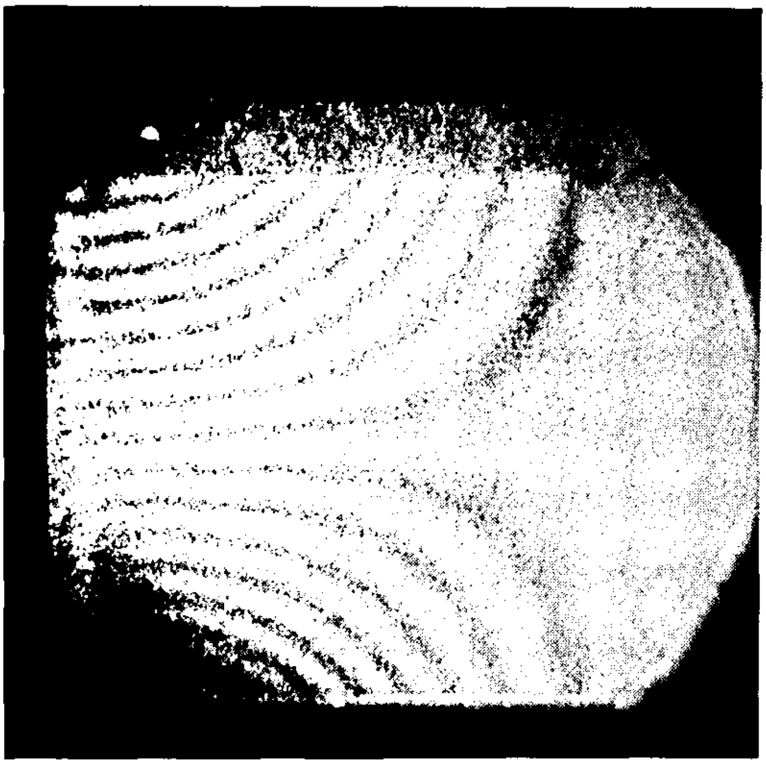

(b)

Figure 6.7
Photographs showing the secondary maxima of fig. 6.5. (a) is for +1 and (b) for -1.

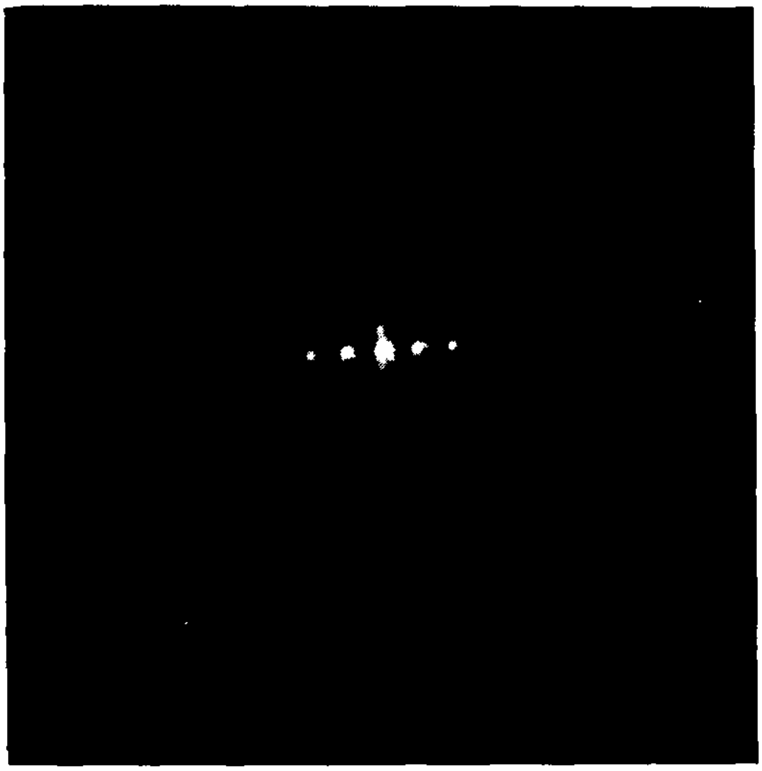

Figure 6.8
Spectrum of transparency in fig. 6.9. The two secondary maxima have rotated with repect to those in fig.6.5 (the one above the axis is +1).

Figure 6.9
Photograph showing a higher fringe density caused by the heavier load in the cantilever.

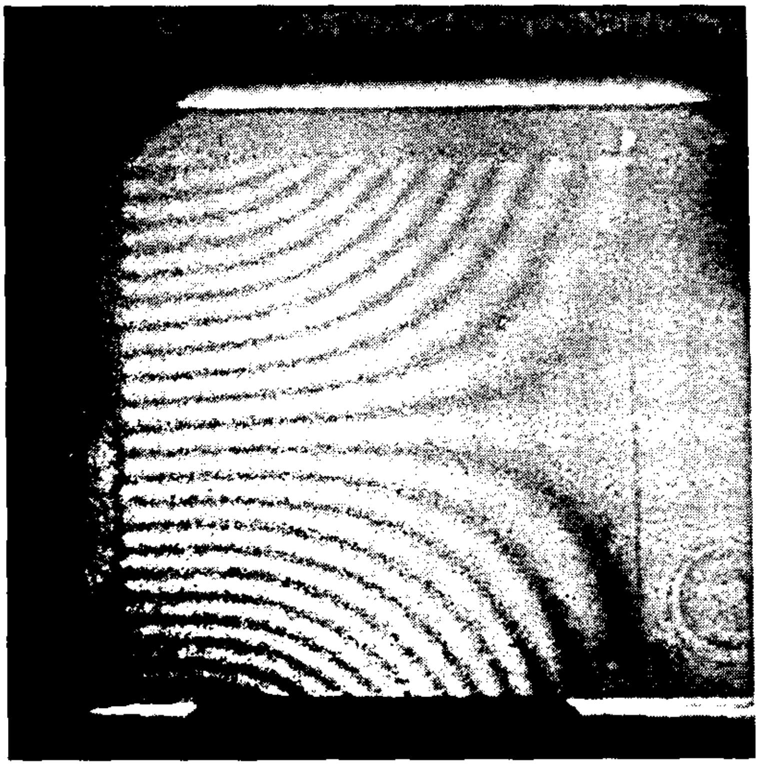

(a)

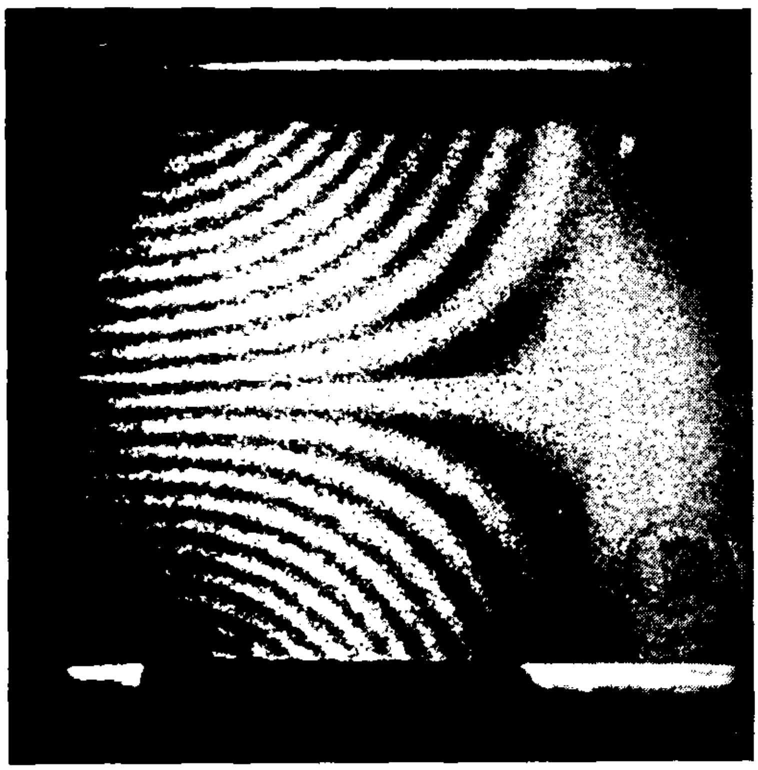

(b)

Figure 6.10
Photographs showing the secondary maxima of fig. 6.8. (a) is for +1 and (b) for -1.

6.4 Closure.

Equation (20) predicts in good agreement what is found experimentally at the Fourier plane of the double-exposed transparency: a central undiffracted spot and secondary maxima distributed symmetrically around the central spot. Stopping the first term in eq. (20) gives way to the noise-free result of figs. 6.7 and 6.10, thus obtaining only the fringe information required. This result suggests the introduction of a variable filter to be used in the electronic part of ESPI, whose final image will then be optically noise-free. An alternative solution for the electronic filter will be to create an addition (or subtraction) fringe pattern within a computer (avoiding the use of an electronic memory) and then calculate the Fourier spectrum of this pattern in such a way that only the fringe information will be passed through the filter. This method has been successfully applied in holographic interferometry, processing the real image of the hologram to get the Fourier spectral information identical to that found here, [35]. More recently a Fourier algorithm (FFT) has been applied to ESPI fringe patterns corroborating the results presented in the present Chapter (to be published [37]). One major drawback of this technique is that the Fourier computation will take some time to be performed and thus the ESPI will not be used in real time. However with the increasing developments in the electronic industry aimed to speed the processing of data (probably with the inclusion of Super conductivity) this problem will be surpassed in the near future.

The technique presented in this Chapter differs from previous reported analogous methods in that here fringes can be obtained right on the double-exposed film using a simple and inexpensive optical set-up. This is in contrast to other methods where two pieces of film have to be overlapped to obtain information about the object distortion or where more expensive holographic film has to be used for the double-exposure method.

CHAPTER VII
IMPLICATIONS FOR FUTURE DESIGNS OF ESPI

The results presented in the previous chapters suggest some design improvements for ESPI. These improvements will give better overall performance and easier operation of ESPI in an industrial environment.

- With the present ESPI system (currently being manufactured by Ealing Electro-Optics with the name of VIDISPEC) there exists a major drawback when alignment procedures are required, since the inexperienced operator will not be able to reach and manipulate the optics that control the alignment of the system.

Results in Chapter III show that this problem can be overcome by redesigning the system as follows (Figure 7.1):

By locating the Beam Splitter in between the object and imaging lens, and attaching the TV camera to the imaging lens, a new optical head for ESPI is realized that permits the easy access to the alignment of the system. Besides this important factor, the results show that the geometry of the reference beam is unimportant as long as it is colinear with the system optical axis and due care is taken with respect to the distance from its point of origin to the imaging lens.

The question of the (wedge) beam splitter introducing astigmatic aberrations and optical noise into the system as quoted by Montgomery ([2]) are avoided in this new design. The problems related to the proper focusing of the object image are therefore alleviated.

Full aperture systems can be used, minimizing the need for large laser power.

The TV camera can now be coupled to the viewing lens, i.e. no degrading light can get to the sensitive camera plate.

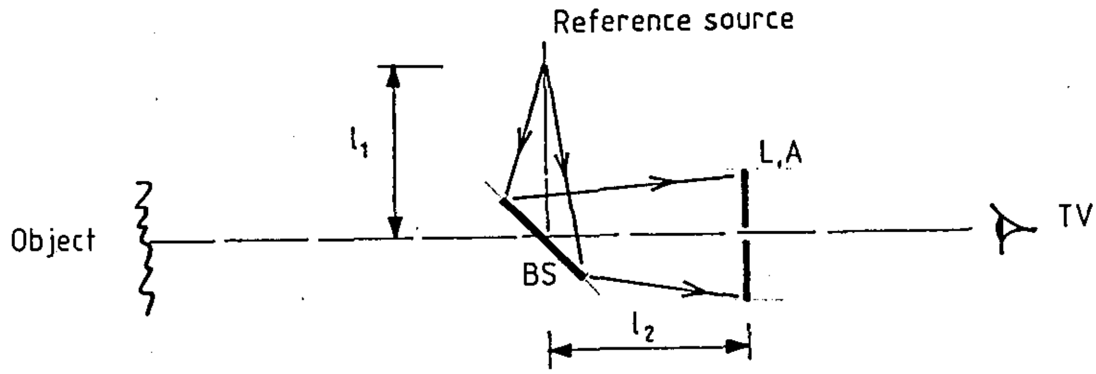

Figure 7.1
New design of ESPI head, including: Beam Splitter in between the object and viewing lens, and TV camera coupled to viewing lens.

From the above it can be concluded that the stringent concept of conjugacy can be disposed of, but good colinearity of the reference beam is required.

This new design for ESPI, reached to by studying its fundamental optical mechanism, is achieved with no more optical components than the ones already present in the existing system. Thus no more optical noise is introduced.

- Special attention should be put in the further development of the theory in Chapter II, since it will lead to the prediction of the shape and number of the fringes to be obtained in ESPI. The current model describes object distortions for limited angles of tilt.

- The theory in Chapters II and V with the information furnished in Chapter IV can be put together in a computer algorithm which will automatically optimize the different parameters in the system leading to a better quality image.

- Chapter VI indicates that a variable filter must be introduced in the electronic apparatus of ESPI to achieve holographic quality.

-With reference to the double-exposure technique implemented here using ordinary photographic film, the same method should be tried using polaroid film and a higher object magnification.

CHAPTER VIII
CONCLUSIONS

Previously the research done on the Electronic Speckle Pattern Interferometer was not based on studying its fundamental operation, but rather the techniques of how to reduce inherently noisy images. These techniques include studies on the statistical properties of the speckle phenomena, electronic signal processing, time average, and computer fringe analysis.

The work in this Thesis was concerned in studying the underlying optical mechanisms of ESPI. Here the way to implement better quality fringes by simple optical means was presented.

Conjugacy, thought to be the main prerequisite of ESPI, was abolished and instead the more easily met condition of colinearity for the reference beam was introduced. A new design for the optical head of the interferometer (without introducing new optical components) was found that gives a better overall performance of the system, e.g. the laser power required is less since a full aperture system can be employed; the optical noise coming from the beam spliter is avoided, and so is the astigmatism in the image; divergent, convergent, parallel or speckled reference beams can be used.

It was seen that aliasing developes independently of the spatial frequency of the speckle pattern, and therefore it is seen as spurious noise in ESPI (barely noticed for high spatial frequencies as those present in the speckle phenomena). Then ESPI fringes are originated from a correlation process between the speckle patterns to be subtracted (added). The net effect of the electronic system is to produce an average of the intensity falling in every pixel.

To further improve the quality of the final image in ESPI, and therefore eliminate the optical noise, a variable filter must be inserted in the electronic apparatus of the system. A final holographic quality image is expected.

It is the firm belief of the author that the introduction of his findings into a new ESPI design, perhaps with the additional use of a pulsed laser, will see the system launched to a successful life in research and industry.

APPENDIX A
THE SCATTERED FIELD

To work out eq.(68), eq.(66) is developed into an exponential series ([13], pp. 82):

$$\chi(V_z,-V_z) = \exp\{-(V_z\sigma)^2\} \sum_{m=0}^{\infty} (V_z^{2m}\,\sigma^{2m}/m!)\,\exp\{-m(r_v/MT)^2\} \qquad (A.2.1)$$

where m is an integer.

To elude problems relating the convergence of the series in eq.(A.2.1), consider the variance of the function ρ, defined as:

$$D\{\rho\} = \langle\rho\rho^*\rangle - \langle\rho\rangle\langle\rho^*\rangle = \langle\rho^2\rangle - \langle\rho\rangle^2 \qquad (A.2.2)$$

The averages are taken over the surface's profile variation. Therefore they are proportional to their corresponding characteristic function, i.e.

$$D\{\rho\} \approx \chi(V_z,-V_z) - \chi(V_z)\chi(V_z)^* \qquad (A.2.3)$$

Substitution of eqs.(55) and (67), and (A.2.1) into (A.2.3) results in:

$$[\chi(V_z,-V_z) - \chi(V_z)\chi(V_z)^*] = e^{-g} \sum_{m=1}^{\infty} (g^m/m!)\,\exp\{-m(r_v/MT)^2\} \qquad (A.2.4)$$

Replacing the above result in Eq.(A.2.2) gives:

$$D\{\rho\} = (2\pi e^{-g}/S)(F_3/M)^2 \sum_{m=1}^{\infty}(g^m/m!) \int_0^{\infty} J_0(V_{x,y}r_v/M)\,\exp\{-m(r_v/MT)^2\}\,r_v\,dr_v \qquad (A.2.5)$$

Summation and integration have been interchanged since the convergence of eq. (A.2.4) is uniform. Since $m > 0$:

$$\int_0^\infty J_0(V_{x,y} r_v/M)\exp(-m(r_v/MT)^2)\, r_v\, dr_v = (1/2m)(MT)^2 \exp(-(T^2/4m)(V_x^2 + V_y^2)) \qquad (A.2.6)$$

Finally substituting eq. (A.2.6) in eq. (A.2.5):

$$D(\rho) = (\pi/S)(F_3T)^2 e^{-g} \sum_{m=1}^{\infty} (g^m/m!\,m) \exp(-(T^2/4m)(V_x^2 + V_y^2)) \qquad (A.2.7)$$

There are three cases to be considered: a) $g \ll 1$ or a slightly rough surface; b) $g \approx 1$, a moderately rough surface and c) $g \gg 1$, a very rough surface.

a) $g \ll 1$. From eq. (A.2.7), and keeping the first term only:

$$D(\rho) = (\pi/S)(F_3T)^2 g \exp(-[g + (T^2/4)(V_x^2 + V_y^2)]) \qquad (A.2.8)$$

b) $g \approx 1$. Realising an estimate of the series in eq. (A.2.7):

$$g \exp(-(V_{x,y}T/2)^2) \leq \sum_{m=1}^{\infty} (g^m/m!\,m) \exp(-(T^2/4m)(V_x^2 + V_y^2)) < e^g \qquad (A.2.9)$$

where the left side of the inequality corresponds to the first term of the series, and the right term to the sum of the exponential series. So, from eq. (A.2.7), and putting $g = 1$:

$$D(\rho) = (\pi/eS)(F_3T)^2 \sum_{m=1}^{\infty} (1/m!\,m)\exp(-(T^2/4m)(V_x^2 + V_y^2)) \qquad (A.2.10)$$

c) $g \gg 1$. For the direction of specular reflection, i.e. $V_{x,y} = 0$, $\theta_1 = \theta_2$ and $\theta_3 = 0$:

$$m!m \simeq (m+1)! \tag{A.2.11}$$

$\therefore$ From eq.(A.2.7)

$$D(\rho) \simeq (\pi/S)T^2 \, (e^{-g}/g)(e^g - 1 - g) \tag{A.2.12}$$

But for $g \gg 1$, $g + 1$ is negligible with respect to e^g, so for the specular direction:

$$D(\rho) \simeq (\pi/gS)T^2 \tag{A.2.13}$$

For the nonspecular direction, $\theta_1 \neq \theta_2$, a "saddle point" integration procedure is carried out for eq.(68), as follows (e.g.,[13], pp. 87):

Eq.(68) receives significant contributions only from the neighbourhood of $r_v = 0$, then:

$$\exp(-(r_v/MT)^2) \simeq 1 - (r_v/MT)^2 \tag{A.2.14}$$

so that eq.(68) can be rewritten as:

$$\langle\rho^2\rangle = (2\pi/S)(F_3/M)^2 \int_0^\infty J_0(V_{x,y}r_v/M) \exp(-g(r_v/MT)^2) \, r_v \, dr_v \tag{A.2.15}$$

and using (A.2.6), it is finally obtained:

$$\langle\rho^2\rangle = (\pi/gS)(F_3T)^2 \exp(-(T^2/4g)(V_x^2 + V_y^2)) \tag{A.2.16}$$

So for $g \gg 1$, the variance of ρ takes the form, after eqs.(57) and (67):

$$D(\rho) = \langle\rho\rho^*\rangle - (F_3\rho_0)^2 \, e^{-g} \simeq \langle\rho\rho^*\rangle = \langle\rho^2\rangle \tag{A.2.17}$$

Eq.(70) and equations that follow it, can be obtained from the previous results.

APPENDIX B
GOVERNING EQUATIONS

Following figure B5.1 consider the case when the raytracing is done backwards, i.e. from an image point on the photosurface to the conjugate object point.

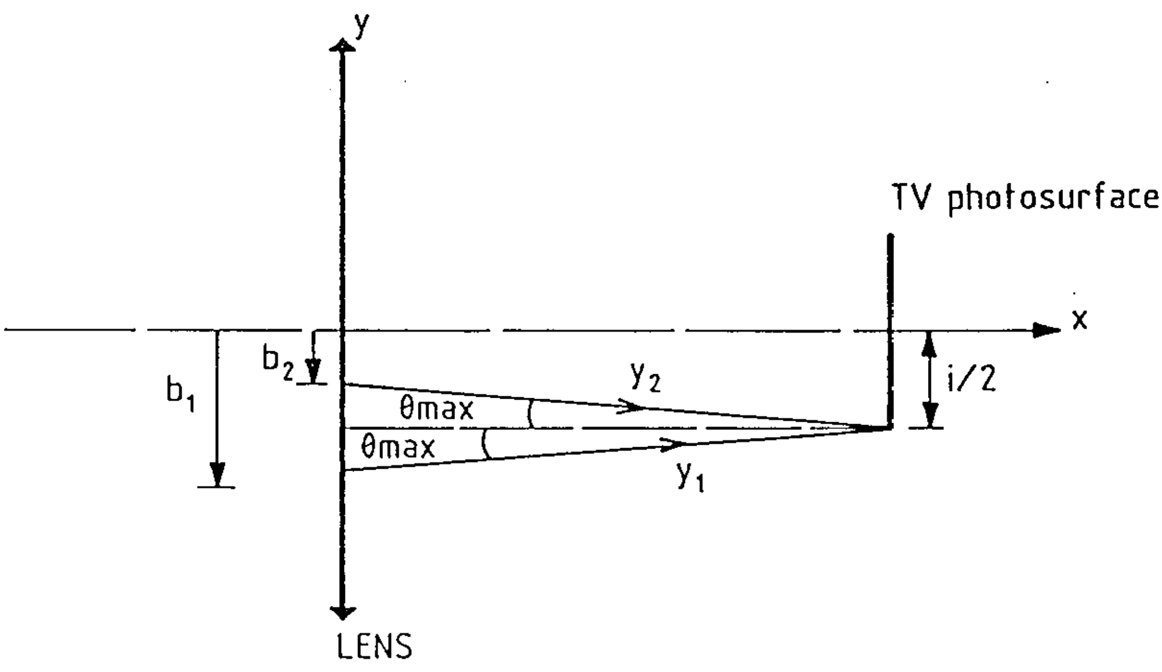

Figure B5.1
Diagram showing the geometrical optics ray tracing to derive eqs. (B.5.1, B.5.2).

The equations for ray 1 and ray 2 are:

$$y_1 = m_1 x + b_1 \qquad (B.5.1)$$

$$y_2 = m_2 x + b_2 \qquad (B.5.2)$$

with

$$m_1 = \tan\theta_{max} \qquad (B.5.3)$$

and

$$m_2 = -\tan\theta_{max} \qquad (B.5.4)$$

Therefore the values of b_1 and b_2 are found for a fixed location of the image point (e.g. $-i/2$, i being the photosurface dimension);

$$b_1 = -i/2 - v\tan\theta_{max} \qquad (B.5.5)$$

$$b_2 = -i/2 + v\tan\theta_{max} \qquad (B.5.6)$$

Thus the limiting semiaperture for the system is b_1. Object rays incident on the lens plane at apertures bigger than this will interfere with the reference beam, but this interference will not be resolved by the electronic sytem.

Once this semiaperture has been found, the object point location is found next with the aid of figure B5.2.

The equation for ray 3 is:

$$y_3 = m_3\, x + b_1 \qquad (B.5.7)$$

The value of m_3 is simply found by recalling that the image point and its conjugate object point are related to each other through the imaging system magnification, i.e

$$Mh_3 = h_2 \qquad \text{with } M = -v/u \tag{B.5.8}$$

$$\Rightarrow \quad m_3 = -i/(2v) + b_1/u \tag{B.5.9}$$

therefore substituting in eq. (B.5.7) for ray 3, it is found:

$$h_3 = -(i/2)/M \tag{B.5.10}$$

as expected.

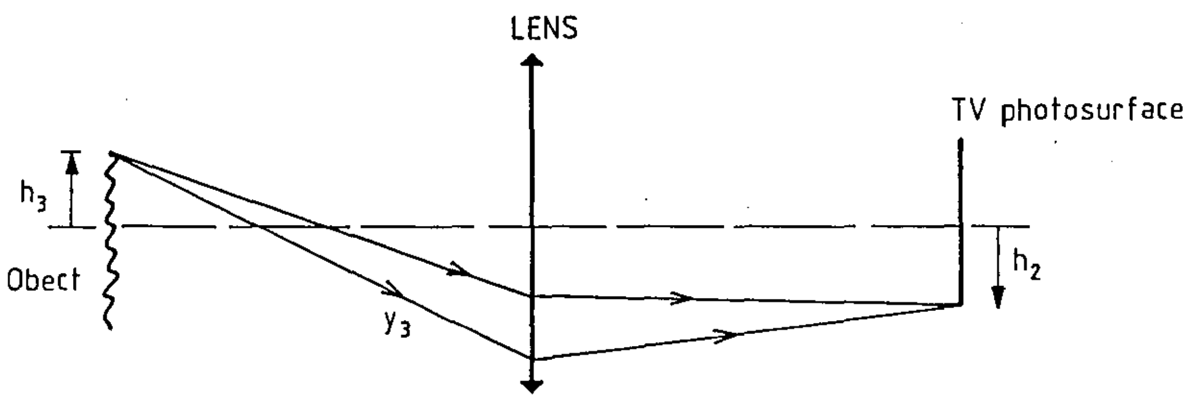

Figure B5.2
This figure shows the ray tracing used to derive
the location of the object point whose image is -i/2.

Since this problem has symmetry with respect to the optical axis the effective aperture diameter D_{max} for which incoming object rays form a resolvable interference on the photosurface plane (of size $i_{x,y}$) is:

$$D_{max} = 2|b_1| = i + 2\ v\ \tan\theta_{max} \tag{B.5.11}$$

The full object size that will give rise to these D_{max} is:

$$H = i|M|^{-1} \tag{B.5.12}$$

The aperture diameter given by eq.(B.5.11) allows in the system angles greater than $\theta_{x,y\ max}$, and thus the electronic apparatus in ESPI being unable to resolve the interference originating from angles outside the cone defined by $2\theta_{x,y\ max}$.

There exists the symmetrical cone of rays for the point below the optical axis that contributes to the resolvable interference in the same way as the point above the axis. With reference to figure B5.3 it is obtained:

$$\gamma = \alpha - \beta \tag{B.5.13}$$

with

$$\alpha = \tan^{-1}(-i/(2f) + M\ \tan\theta_{max}) \tag{B.5.14}$$

and

$$\beta = \tan^{-1}(-i/(2f) - M\ \tan\theta_{max}) \tag{B.5.15}$$

The angle γ given in eq.(B.5.13) is the real angular spread of rays from an object point that contributes to the resolvable interference on the photosurface.

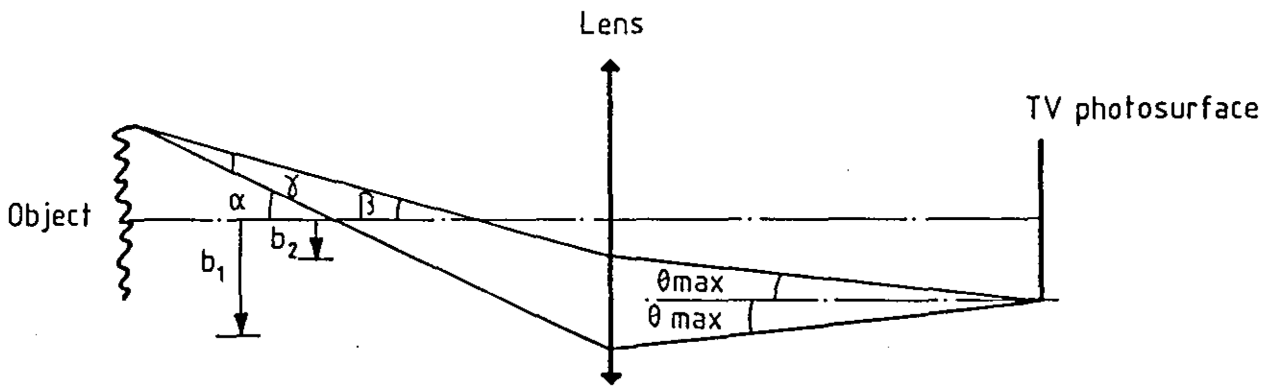

Figure B5.3
Diagram showing the effective cone of rays contributing to the resolvable interference.

Figure B5.3 and equations derived from it suggests the possibility of using an aperture in the form of slits instead of a circular one, to allow the system to resolve the interference pattern considered troughout this appendix.

APPENDIX C

NOMENCLATURE TO CHAPTERS II AND VI.

Chapter II

Vectors appear in bold face, corresponding magnitudes in normal type script, e.g. **r**, r.

r_{eo} → Object amplitude reflectivity.
r_i → Distance from object illuminating source to object surface.
r_o → Distance from the object where the scattered field is being observed.
r' → Position vector on the X'Y' object axes.
r → Position vector on the XY viewing lens plane.
u → Object to imaging lens distance.
v → Viewing lens to image plane distance.
f → Imaging lens focal length.
M → Viewing lens magnification.
u_v → Distance from the plane/point of origin of the reference beam to the camera plate (beam splitter behind imaging lens).
u_r → Distance from the plane/point of origin of the reference beam to the imaging lens (beam splitter in front imaging lens).
S → Object area under observation.
θ_1 → Angle of incidence of illuminating object beam.
θ_2 → Angle of scattering.
θ_3 → Angle of latteral scattering.
k → Wave number.
n → Refractive index of air.
n' → Refractive index of imaging lens.
λ → Wavelength of illuminating light.
ξ → Object surface roughness.
Δ_o → Lens central thickness.
α → Radius of aperture in front of the imaging lens.

P → Pupil or aperture function.

δ → Dirac Delta function.

J_o → Zero order Bessel function.

J_1 → First order Bessel function.

h → Impulse response function.

ρ → Scattering coefficient.

E_{2o} → Object field for the specular direction.

$U=E_2$ → Complex amplitude distribution of the scattered field.

U' → Complex amplitude distribution of the object field immediately after the lens plane.

U_{in} → Complex amplitude distribution of the object illuminating wave.

U_v → Complex amplitude distribution of the object field at the image plane.

U_{go} → Geometrical optics amplitude distribution for the object image field.

Ur_v → Complex amplitude distribution of the reference beam at the image plane.

A → Amplitude of plane wave.

I_o → Object intensity.

I_r → Reference beam intensity.

ϕ_o → Object wavefront phase.

ϕ_r → Reference beam phase.

ψ_o → random speckle phase.

$\Delta\phi$ → Change of phase caused by object deformation.

Mo → Fringe modulation function.

χ → Surface characteristic function.

w → The Normal distribution.

σ → Surface roughness function.

$C(\tau)$ → Density of surface irregularities.

τ, T → Correlation distances.

g → Parameter measuring the roughness of the surface.

Chapter VI

U_r → Complex amplitude distribution for reference beam.

U_o → Complex amplitude distribution for object beam.

ϕ_o → Object wavefront phase.

ϕ_r → Reference beam phase.

ψ_o → random speckle phase.

$\Delta\phi$ → Change of phase caused by object deformation.

r → Ratio of reference to object beam intensities.

D → Film density.

e → Exposure.

Γ → Constant.

B → Brightness.

Mo → Fringe modulation function.

α → Unrectified signal to noise ratio.

C → Contrast.

g → Amplitude transmission function of photographic film.

G → Spectrum of intensity distribution at the Fourier plane.

$F(g)$ → Fourier transform of g.

δ → Dirac delta function.

p_1 → Joint probability density function.

$p_{2,3}$ → Probability density functions.

APPENDIX D
LIST OF TABLES

Chapter V

APPENDIX E
LIST OF FIGURES

Chapter III

Chapter IV

Chapter V

Chapter VI

Chapter VII

Appendix B

APPENDIX F
PUBLICATIONS

The following is a list of papers published (or to be published) by the author during the Ph.D. work at Loughborough University.

1) Mendoza Santoyo F., Kerr D. and Tyrer J., "Manipulation of the Fourier components of speckle fringe patterns as part of an interferometric analysis process", to be submitted for publication to the Journal of Modern Optics.

2) Mendoza Santoyo F. and Bergquist B.D., "Photographic speckle pattern interferometry: an analisys of its Fourier components and their application to electronic speckle pattern interferometry (ESPI)", invited paper presented at the conference **Industrial Optoelectronic Measurement Systems Using Coherent Light**, organized by the ANRT and SPIE, Cannes, France, November 1987.

3) Rowland A.C. and Mendoza Santoyo F., "Evaluation of dynamic volume viscoelasticity using electronic speckle pattern interferometry", Optical Engineering, 25, 7, pp. 865, (1986).

4) Bergquist B.D., Montgomery P.C., Mendoza Santoyo F., Henry P. and Tyrer J., "The present status of electronic speckle pattern interferometry (ESPI) with respect to automatic fringe inspection and measurement", SPIE, vol. 654, **Automatic Optical Inspection**, pp. 95, (1986).

5) Bergquist B.D. and Mendoza Santoyo F., "Electronic speckle pattern interferometry (ESPI): some observations concerning conjugacy and fringe resolution", Proceedings of the International Conference **Electro Optics '86**, H.G. Jerrard Ed., Southampton University/Cahner's Exposition Group, Brighton, England, (1986).

ACKNOWLEDGEMENTS

I would like to express my sincere gratitude to my supervisor Brian Bergquist for his expert advice and direction on the present work and for his friendship. Unfortunately, he recently had a heart attack that made him unable to assess part of this thesis. His place was taken by Dr. D Rowley to whom I am very grateful for his valuable comments and suggestions that gave the thesis its final form. I also thank Professor J Dent as my Director of Research, for his encouragement towards the end of my work.

I thank the financial assistance of The British Council and of CONACYT (National Council for Science and Technology) Mexico. The study leave granted by Centro de Investigaciones en Optica (Optical Research Centre) Mexico, through its director Dr. D. Malacara is acknowledged.

The friendship and moral support of my colleagues in the Optics Group has been invaluable. Adrian Rowland, Paul Montgomery, Paul Henry, Vick Roulstone, Liz Raymond, John Tyrer, John Powell, Mick Smeeton, David Hackett, David Kerr, Janet Folkes and Paul king. Special thanks are due to Janet Folkes whose computer I have been using to type my thesis, to Paul Henry and Vick for their help with computer and technical problems, respectively and to Mick and David Hackett for their assistance on electronic related problems.

The photographs appearing in the text are due to Ken Topley and Maggie Martin whose friendship is appreciated. I thank Mr. P LeGood and Janet Redman for the drawings.

Finally, thanks to all my friends outside the University environment for their love and support throughout this work.

BIBLIOGRAPHY

[1] Butters J.N. and Leendertz J.A., "Speckle patterns and holographic techniques in engineering metrology", Optics and Laser Technology, 3, pp.26, (1971).

[2] Montgomery P.C., "Forward looking innovations in electronic speckle pattern interferometry", Ph.D. thesis, Loughborough University of Technology, England, (1987).

[3] Jones R. and Wykes C., **Holographic and speckle interferometry**, Cambridge University Press, (1983).

[4] Jones R. and Wykes C., "General parameters for the design and optimization of electronic speckle pattern interferometers", Optica Acta, 28, 7, pp.949, (1981).

[5] Slettemoen G.A., "Optimal signal processing in electronic speckle pattern interferometry", Optics Communications, 23, 2, pp. 213, (1977).

[6] Slettemoen G.A., "General analysis of fringe contrast in electronic speckle pattern interferometry", Optica Acta, 26, 3, pp. 313, (1979).

[7] Wykes C., "Decorrelation effects in speckle pattern interferometry: 1. Wavelength change dependent de-correlation with application to contouring and surface roughness measurement", Optica Acta, 24, 5, pp. 517, (1977).

[8] Bergquist B.D., Montgomery P.C., Mendoza Santoyo F., Henry P. and Tyrer J., "The present status of electronic speckle pattern interferometry (ESPI) with respect to automatic inspection and measurement", SPIE, 654, **Automatic Optical Inspection**, pp. 95, (1986).

[9] Pedersen H.M., Lökberg O.J. and Förre B.M., "Holographic vibration measurement using a TV speckle interferometer with silicon target vidicon", Optics Communications, 12, 4, pp. 421, (1974).

[10] Slettemoen G.A., "Electronic speckle pattern interferometric system based on a speckled reference beam", Applied Optics, 19, 4, pp. 616, (1980).

[11] Creath K. and Slettemoen G.A., "Vibration-observation techniques for digital speckle-pattern interferometry", Journal of the Optical Society of America A, 2, 10, pp. 1629, (1985).

[12] Wykes C., "A theoretical approach to the optimization of electronic speckle interferometry fringes with limited laser power", Journal of Modern Optics, 34, 4, pp. 539, (1987).

[13] Beckmann P. and Spizzichino A., **The scattering of electromagnetic waves from rough surfaces**, Pergamon Press, (1963).

[14] Born M. and Wolf E., **Principles of optics**, Sixth Edition, Pergamon Press, (1980).

[15] Goodman J.W., **Introduction to Fourier optics**, McGraw-Hill Book Company, (1968).

[16] Gradshteyn I.S. and Ryzhik I.M., **Table of integrals, series, and products**, Fourth Edition, Academic Press, (1965).

[17] Bergquist B.D. and Mendoza Santoyo F., "Electronic speckle pattern interferometry: some observations concerning conjugacy and fringe resolution", Proceedings of the International Conference **Electro Optics '86**, H.G. Jerrard Ed., Southampton University/Cahner's Exposition Group, Brighton, England, (1986).

[18] Stetson K.A., "New design for laser image-speckle interferometer", Optics and Laser Technology, pp. 179, (1970).

[19] Tanner L.H., "A study of fringe clarity in laser interferometry and holography", Journal of Physics E, 1, 2, pp. 517, (1968).

[20] Mendoza Santoyo F. and Bergquist B.D., "Photographic speckle pattern interferometry: an analysis of its Fourier components and their application to electronic speckle pattern interferometry (ESPI)", invited paper presented at the SPIE Conference: **Industrial Optoelectronic Measurement Systems Using Coherent Light**, Cannes, France, November 1987.

[21] Jenkins F.A. and White H.E., **Fundamentals of optics**, Fourth Edition, McGraw-Hill International Book Company, (1981).

[22] Slettemoen G.A., "First-order statistics of displayed speckle patterns in electronic speckle pattern interferometry", Journal of the Optical Society of America, 71, 4, pp. 474, (1981).

[23] Burch J.M. and Tokarski J.M.J., "Production of multiple beam fringes from holographic scatterers", Optica Acta, 15, 2, pp. 101, (1968).

[24] Leendertz J.A., "Interferometric displacement measurement on scattering surfaces utilizing speckle effect", Journal of Physics E, 3, pp. 214, (1970).

[25] Archbold E., Burch J.M. and Ennos A.E., "Recording of in-plane surface displacement by double-exposure speckle photography", Optica Acta, 17, 12, pp. 883, (1970).

[26] Tiziani H.J., "Application of speckling for in-plane vibration analysis", Optica Acta, 18, 12. pp. 891, (1971).

[27] Tiziani H.J., "A study of the use of laser speckle to measure samll tilts of optically rough surfaces accuratelly", Optics Communications, 5, 4, pp. 271, (1972).

[28] Stetson K.A., "Analysis of double-exposure speckle photography with two beam illumination", Journal of the Optical Society of America, 64, 6, pp. 857, (1974).

[29] Verhoeven D.D. and Farrell P.V., "Speckle interferometry in transparent media", Applied Optics, 25, 6, pp. 903, (1986).

[30] Klimenko I.S., Ryabukho V.P., Feduleev B.V. and Lokhova N.V., "Some features of holographic and speckle interferograms produced by recording the object light field in the Fourier plane", Optical Spectroscopy (USSR), 55, 3, pp. 284, (1983).

[31] Kadono H., Takai N. and Asakura T., "Experimental study of the laser speckle phase in the image field", Optica Acta, Special issue **25 Years of the Laser**, (1985).

[32] Steward E.G., **Fourier optics: an introduction**, Ellis Horwood series in Physics, (1983).

[33] Goodman J.W. in, **Laser speckle and related phenomena**, Edited by J.C. Dainty, Springer-Verlag, (1975).

[34] Bergquist B.D., in Proceedings of the International Conference **Electro Optics '82**, H.G. Jerrard Ed., Southampton University/Cahner's Exposition Group, Brighton, England, (1982).

[35] Kreis T., "Quantitative evaluation of interference patterns", Proceedings of the International Symposium on the Techniques for Optoelectronics, SPIE, Cannes (France), (1987).

[36] Stetson K.A. and Brohinsky W.R., "Electro-optic holography system for vibration analysis and non destructive testing", Optical Engineering, 26, 12, pp. 1234, (1987).

[37] Mendoza Santoyo F., Kerr D. and Tyrer J., "Manipulation of the Fourier components of speckle fringe patterns as part of an interferometric analysis process", to be submitted for publication in the Journal of Modern Optics.